

**Evaporative Drying of Cupric-Chloride Droplets
In a Thermo-Chemical Cycle of Hydrogen Production**

By

Mateusz Slowikowski

A Thesis Submitted in Partial Fulfillment
of the Requirements for the Degree of
Master of Applied Science (M.A.Sc)

In

The Faculty of Engineering and Applied Science

Program: Mechanical Engineering

University of Ontario Institute of Technology

August 2012

© Mateusz Slowikowski, 2012

ABSTRACT

In this thesis, new empirical correlations that predict the behaviour of Cupric-Chloride droplets undergoing spraying and drying processes are developed. Cupric-Chloride is a chemical compound with the formula CuCl_2 that is present as slurry or aqueous solution within the Copper-Chlorine (Cu-Cl) thermo-chemical cycle for generation of hydrogen. An experimental study examines the effects of inlet air and liquid temperatures, pressure, concentration, nozzle diameter, and liquid flow rate on the outlet air temperature, particle size, particle size distribution, morphology, moisture content, bulk density, and flowability.

The analysis examines a single droplet of CuCl_2 solution in a continuum drying media. The validation of the model involves comparisons with experimental data from previous studies of different fluids based on non-dimensional analysis. The study provides new information about the effects of different concentrations of water in the CuCl_2 slurry drying at low to moderate air temperatures. Analytical correlations of heat and mass transfer are developed for the aqueous solution, subject to various drying conditions. The analysis is performed for moist air in contact with a sprayed aqueous solution of Copper (II) Chloride Dihydrate [$\text{CuCl}_2 \cdot (2\text{H}_2\text{O})$]. Validation of the model is performed by comparisons with experimental results.

Acknowledgements

This thesis would not have been completed without the constant support of many people. First, I would like to give my most sincere thanks to *Professor G.F. Naterer* for providing me with the opportunity to conduct research in this area, for his unconditional encouragement and leadership, and for his technical expertise and mentorship.

The senior CERL team was unwavering in their inspiration and support. I am most grateful not only for their technical expertise, but to also the fine example that they give to others through their work. Specifically, I give thanks to *Dr. V.N. Daggupati, Dr. Z. Wang, E. Secnik, Dr. G. Marin*, and to *R.R. Roberts*.

My parents are given special thanks for their support and expertise, both of whom have dedicated their careers to advocating safe nuclear technology. Both have completed their masters degrees at the Jagellonian University in Krakow, Poland, and have passed on a wealth of knowledge in engineering. Without their continuous love and support, I would have hesitated many times during this endeavour. Finally, financial support for this project from Atomic Energy of Canada Ltd. and the Ontario Research Excellence Fund is gratefully acknowledged. Without the help, support, expertise, and guidance of all those I have mentioned, my work would not have been possible.

This thesis is dedicated to my parents,
and all those without whom this would not have happened.

Table of Contents

ABSTRACT.....	i
Acknowledgements.....	ii
Nomenclature.....	xiii
Acronyms.....	xviii
1 Introduction.....	1
1.1 Background.....	1
1.2 Thesis outline.....	2
1.3 Motivation of Thesis.....	4
2 Background.....	6
2.1 Hydrogen production.....	6
2.2 Nuclear hydrogen production.....	8
2.3 Options for copper II chloride recovery.....	10
2.3.1 Limitations from the electrochemical cell.....	11
2.3.2 Requirements for the hydrolysis reaction.....	13
3 Literature survey.....	15
3.1 Copper II Chloride and its industrial uses.....	15
3.2 Spray drying.....	16
3.2.1 Particle size.....	17
3.2.2 Particle size distribution.....	18
3.2.3 Moisture content.....	20
3.2.4 Bulk density, flowability.....	20
3.2.5 Outlet air temperature.....	21
3.2.6 Morphology and crystallinity of the spray dried particles.....	22
3.3 Convective drying.....	23
4 Drying Phenomena.....	25
4.1 Spray Drying.....	27
4.1.1 Fluid mechanics.....	29
4.1.2 Heat transfer.....	31
4.2 Convective drying.....	33
5 Physical Properties.....	34
5.1 Property estimation.....	34
5.1.1 Diffusion coefficient.....	35
5.1.1.1 Air – vapor mixture.....	35
5.1.2 Density.....	36
5.1.2.1 Air – vapor mixture.....	36
5.1.2.2 Electrolyte.....	36
5.1.3 Viscosity.....	38
5.1.3.1 Air-vapor mixture.....	38

5.1.3.2	Electrolyte.....	39
5.1.4	Surface tension.....	40
5.1.5	Thermal conductivity	44
5.1.5.1	Air-vapor mixture	45
5.1.5.2	Electrolyte.....	45
5.1.6	Heat capacity.....	46
5.1.6.1	Air-vapor mixture	46
5.1.6.2	Electrolyte.....	47
5.1.7	Partial pressure.....	49
5.1.8	Wet bulb temperature.....	50
5.1.1	Latent heat of vaporization	51
6	Theory	53
6.1	Fluid spraying.....	53
6.1.1	Fluid mechanics	53
6.1.2	Jet breakup length	57
6.2	Heat and mass transfer	60
6.2.1	Initial droplet heating.....	61
6.2.2	Evaporation and shrinkage.....	63
6.2.2.1	Mass transfer analysis.....	64
6.2.2.2	Heat transfer analysis.....	65
1.1.1	Velocity estimation	67
6.3	Particle size distributions	67
6.3.1	Characteristics of particle distribution functions	67
6.3.2	Log-normal distribution	68
6.3.3	Maximum-ended log-normal distribution.....	68
6.3.4	Root normal distribution.....	69
6.3.5	Rosin-Rammler distribution.....	69
6.3.6	Test for best fit.....	70
6.4	Convective drying	70
6.4.1	Characteristic rate drying curve	70
7	Materials and methods	72
7.1.1	Experimental design.....	72
7.1.2	Drying apparatus.....	74
7.1.3	Materials	75
7.1.4	Product characterization.....	75
7.1.4.1	Particle size distribution	76
7.1.4.2	Particle size.....	77
7.1.4.3	Particle morphology	78
7.1.4.4	Volatile content.....	78
7.1.4.5	Particle flowability	79
7.2	Convective Drying	79
7.2.1	Experimental design.....	79
7.2.2	Drying apparatus.....	80
7.2.3	Materials	81

8 Results and discussion	82
8.1 Spray drying	82
8.1.1 Outlet air temperature	83
8.1.2 Atomization flow rate	85
8.1.3 Particle morphology and crystalinity	87
8.1.4 Moisture content	90
8.1.5 Particle size	91
8.1.5.1 Span	91
8.1.5.2 Excluding agglomeration effects	93
8.1.5.3 Equivalent droplet diameter.....	97
8.1.5.4 Particle size correlation: previous models	101
8.1.5.5 Particle size correlation development.....	103
8.1.5.6 First correlation iteration	105
8.1.5.7 Thybo droplet based particle correlation	111
8.1.5.8 Groom droplet based particle correlation	112
8.1.6 Particle size distribution.....	113
8.1.7 Particle flowability	118
8.2 Convective drying	121
8.2.1 Dihydrate.....	121
8.2.2 Slurry drying	121
8.2.3 Drying rate calculations	123
9 Conclusions and recommendations	125
9.1 Conclusions	125
9.2 Recommendations	126
Bibliography	128
Appendix A: Surface tension, viscosity, and density measurements.....	139
Appendix B: program for Bayesian information criterion test	140
Appendix C: Experimental results	141
Appendix D: Results from particle distribution analysis.....	142
Appendix E: Matlab code	144
Appendix E: Corrosion notes.....	146

List of Tables

Table 2.1: Steps in the Copper-Chlorine Cycle [11].....	9
Table 3.1: Particle size definitions.....	18
Table 3.2: Droplet size correlations for spray drying	19
Table 5.1: Electrolyte density model coefficients.....	37
Table 5.2: Air viscosity model coefficients	39
Table 5.3: Viscosity Equation coefficients	39
Table 5.4: β fitting parameter for various chlorine compounds	42
Table 5.5: Surface tension coefficient data	43
Table 5.6: α coefficients for selected aqueous ions.....	46
Table 5.7: Coefficients for heat capacity correlations.....	48
Table 5.8: Coefficients for partial pressure correlations.....	50
Table 6.1: Jet breakup length dimensional analysis variables	57
Table 7.1: Experiments performed with their respective varied parameters.....	72
Table 7.2: Drying rate experiments.....	79
Table 8.1: Parameters from Run #39	93
Table 8.2: Spans calculated from three laser diffractometer runs from experiment #39.....	94
Table 8.3: Determining the Sauter diameter of Run #39	97
Table 8.4: Particle size parameters	103
Table 8.5: Dimensionless groups for the particle size correlation.....	104
Table 8.6: Particle size distribution best fit results	117
Table 8.7: Parameter values for curve fits	117
Table 8.8: CRDC rate calculations	124

Table 12.1: Experimental results: spray drying	141
Table 15.1: Compiled chemical resistance data	146

List of Figures

Figure 2.1: Various methods to produce hydrogen.....	7
Figure 2.2: Projected cost of various hydrogen production methods [6].....	8
Figure 2.4: Schematic of the Copper-Chlorine Cycle [12]	9
Figure 2.5: Summary of dcc processing options for the Cu–Cl cycle	10
Figure 2.6: Schematic of the electrolytic cell	12
Figure 2.7: Percentage distribution of chlorocopper (I) complexes at different temperatures [14]	13
Figure 4.1: Drying rate curve at constant drying conditions.....	26
Figure 4.2: Schematic of spray drying apparatus.....	27
Figure 4.3: Two fluid pneumatic nozzle [30]	28
Figure 4.4: Atomization regions of the spray from a two fluid nozzle [42]	30
Figure 4.5: Droplet drying process	31
Figure 4.6: SEM of spray drying Run #25 - example of blowholes	32
Figure 4.7: Conventional drying oven	33
Figure 5.1: Electrolyte density model.....	37
Figure 5.2: Electrolyte viscosity model	40
Figure 5.3: Osmotic coefficient data fit	43
Figure 5.4: Electrolyte surface tension model	44
Figure 5.5: Electrolyte thermal conductivity model	46
Figure 5.6: Electrolyte heat capacity model	47
Figure 5.7: Partial pressure vs. temperature of water and dcc [40] [48].....	49
Figure 5.8: Phase diagram of drying process [59]	51

Figure 7.1: Nozzle geometry [76]	74
Figure 7.2: Sample bottle with copper II chloride to be dried	81
Figure 8.1: Particle diameter vs. inlet temperature and atomization pressure	82
Figure 8.2: Particle diameter vs. Ohnesorge and Nusselt numbers	83
Figure 8.3: Outlet temperature vs. inlet Temperature.....	84
Figure 8.4: Atomization flow rate vs. temperature	86
Figure 8.5: Atomization air flow rate correlation	86
Figure 8.6: Particles dried at 200°C	88
Figure 8.7: Particles dried at 120C	88
Figure 8.8: Particles dried at 60°C	89
Figure 8.9: Initial concentration vs. wall thickness ratio	90
Figure 8.10: Moisture content vs. hot air inlet temperature.....	91
Figure 8.11: Span vs. Particle diameter	92
Figure 8.12: Results from laser diffractometer run no. #39-2	94
Figure 8.13: SEM images from Run #39	95
Figure 8.14: Diameter peak summation calculation	96
Figure 8.15: Run 21: droplet coalescence during mass transfer and drying.....	97
Figure 8.16: Central void fraction and wall void fraction	98
Figure 8.17: Discounting droplet drying, with non-spherical particles	99
Figure 8.18: Discounting droplet drying, without non-spherical particles	100
Figure 8.19: Droplet diameter vs. inlet temperature and atomization pressure	100
Figure 8.20: Calculated droplet size from Mulhem model vs. measured droplet size	101
Figure 8.21: Calculated droplet size from Groom et al. model vs. measured droplet size	102

Figure 8.22: Calculated droplet size from Thybo model vs. measured droplet size.....	102
Figure 8.23: First step, obtaining power value	106
Figure 8.24: First step after obtaining the power value	107
Figure 8.25: Second step after obtaining the power value.....	107
Figure 8.26: Third step after obtaining the power value.....	108
Figure 8.27: Fourth step after obtaining the power value.....	109
Figure 8.28: Fifth step after obtaining the power value.....	109
Figure 8.29: Fifth step after obtaining the power value.....	110
Figure 8.30: Sixth step after obtaining the power value	110
Figure 8.31: Thybo-based correlation after fifth step	111
Figure 8.32: Groom-based correlation after fifth step	112
Figure 8.33: Run no. 2 (80°C, 0.7mm nozzle) particle results	114
Figure 8.34: Run no. 2 (80°C, 0.7mm nozzle) SEM results	114
Figure 8.35: Run no. 3 (120°C, 0.7mm nozzle) particle results	115
Figure 8.36: Run no. 3 (120°C, 0.7mm nozzle) SEM results	115
Figure 8.37: Run no. 36 (200°C, 0.7mm nozzle, 1/2 nominal pressure) particle results.....	116
Figure 8.38: Run no. 36 (200°C, 0.7mm nozzle, 1/2 nominal pressure) SEM results.....	116
Figure 8.39: Correlation between Hausner ratio and compression ratio	118
Figure 8.40: Hausner ratio vs. particle diameter [all data]	119
Figure 8.41: Hausner ratio vs. particle diameter [higher heat additions]	119
Figure 8.42: power law Equation for Hausner ratio	120
Figure 8.43: Convective drying rate experiments.....	121
Figure 8.44: Initial data from slurry drying at 100C.....	122

Figure 8.45: Drying rate determined from slurry data at 100C	123
Figure 13.1: Run no. 1 (60C, 0.7mm nozzle) particle results.....	142
Figure 13.2: Run no. 1 (60C, 0.7mm nozzle) SEM results.....	142
Figure 13.3: Run no. 4 (160C, 0.7mm nozzle) particle results.....	143
Figure 13.4: Run no. 4 (160C, 0.7mm nozzle) SEM results.....	143
Figure 15.1: Stainless Steel (left) and Titanium (right) nozzle corrosion.....	146

Nomenclature

a	Activity of water [-]
\bar{A}	Partial molar surface area [m^2]
A	Area [m^2]
B	Spalding number [-]
Bi	Biot number [-]
c	Molar concentration of ion [-]
c	Property model constants [-]
C_p	Heat capacity [$\text{kJ}/\text{kg}\cdot\text{K}$]
d	Diameter [m]
\bar{d}	Representative diameter for curve-fitting [m]
\mathcal{D}	Mass diffusion coefficient [m^2/s]
e^-	Electron [-]
F	Force [N]
fs	Enhancement factor (for ideal gas Equation application of water vapor) [-]
Fo	Fourier number [-]
g	Acceleration due to gravity [m^2/s]
G	Mass flux of air at nozzle outlet [$\text{kg}/(\text{m}^2\text{s})$]
h	Heat transfer coefficient [$\text{W}/\text{m}^2\text{K}$]
h	Mass transfer coefficient [m/s]
HR	Hausner ratio [-]
ΔH_v	Latent heat of vaporization [kJ/kg]

k	Coefficient of thermal conductivity [W/m K]
K	Units of temperature [Kelvin]
L	Length [m]
L	Volume to surface area ratio [m]
L_C	Characteristic dimension of the nozzle (taken as nozzle diameter) [m]
\dot{m}	Flow rate [kg/s]
m	Molecular weight [kg/mol]
m	Molality [mol/kg]
m_i	Measured value [-]
M	Mass [kg]
n	Molar mass of substance [kg/mol]
N	Number of parameters [-]
\aleph	Drying rate [kg/m ² s]
Nu	Nusselt number [-]
Oh	Ohnesorge number [-]
p	Pressure [Pa]
p_i	Predicted value [-]
Δp	Differential pressure, change in pressure [Pa]
Pr	Prandtl number [-]
q	Parameter describing distribution width [$q < 3$]
\vec{q}	Heat flux density [W/m ²]
r	Radius, radial displacement [m]
R	Universal gas constant [KJ / kmol K]

\mathcal{R}	Radius of curvature of free surface [m]
RH	Relative humidity [-]
Re	Reynolds number [-]
S	Concentration ratio [-]
Sc	Schmidt number [-]
Sh	Sherwood number [-]
t	Parameter [-]
t	Time [s]
T	Temperature [$^{\circ}\text{C}$] or [K]
∇T	Temperature gradient [K/m]
u	x-direction velocity[m/s]
v	y-direction velocity[m/s]
vf_c	Central void fraction [-]
vf_w	Wall void fraction [-]
V	Volume, molecular volume [m^3]
w	z-direction velocity[m/s]
We	Weber number [-]
x	Mass fraction[-]
X	Dry basis moisture content [kg H ₂ O / kg dry substance]
x	x-direction distance, displacement [m]
y	y-direction distance, displacement [m]
z	z-direction distance, displacement, jet length [m]

Subscripts

0	Initial, first
1	Reference temperature, first
2	Desired temperature, second
10	Number mean
20	Surface mean
30	Volume mean
32	Sauter mean
∞	Bulk value
a	air
<i>at. air</i>	Atomizing air
aq	Aqueous (in solution)
b	Bulk gas, bulk fluid
c	Critical temperature
cr	Critical
d	Droplet
e	Equilibrium
h	Heat
g	Gas
m	Mass
max	Maximum
<i>mmd</i>	Mass median droplet
<i>mr</i>	Root-mean
xvi	

p	Particle
s	Surface
sat	Saturation conditions
sol	Solution
w	Water
sw	Wet solid
wb	Wet bulb
wv	Water vapor
θ	Angle – direction

Superscripts

*	Non-dimensionalized
---	---------------------

Greek letters

α	Contribution to thermal conductivity of ion [-]
α	Thermal diffusivity [m^2/s]
μ	Dynamic viscosity [$\text{Pa}\cdot\text{s}$]
ν	Kinematic viscosity [m^2/s]
ρ	Density [kg/m^3]
τ	Shear stress [N/m^2]
σ	Surface tension [N/m]
σ	Parameter describing shape of distribution [-]

σ^2	Bayesian information criterion test [-]
ν	Stoichiometric coefficient [-]
φ	Osmotic coefficient [-]
θ	Angle, surface- liquid contact angle [°]
θ	Non-dimensional temperature [-]
χ	Chi, for chi-squared test [-]

Acronyms

AECL	Atomic Energy of Canada Limited
CERL	Clean Energy Research Laboratory
Cu-Cl	Copper Chlorine
dcc	Copper Chloride dihydrate
DPF	Discrete probability function
GHG	Greenhouse gas
IGCC	Integrated gasification combined cycle (coal gasification)
LALLS	Low angle light scattering, or laser diffraction
ME	Maximum entropy
MSA	Mean spherical approximation
PCB	Printed circuit board
SEM	Scanning electron microscope
SMR	Steam methane reforming
S-I	Sulphur-Iodine

TC Thermochemical cycle
TGA thermo-gravimetric analysis

Chapter 1

Introduction

1.1 Background

Our way of life, measured by the *standard of living* and *quality of life*, is greatly dependent on energy and resource consumption [1]. Our exponentially growing resource consumption has caused CO₂ emissions to grow 188% between 1973 and 2008 [2]. Our footprint on the planet is so strong that geologists are proposing a new epoch, called the *Anthropocene*, to accurately describe this period. However, as the name suggests, humans are the masters of their fate: the *Anthropocene* is an epoch defined by the human impact on the planet [3].

About 95% of our transportation energy comes from oil and conventional fuels [4]. As more sustainable methods for producing energy for transportation are developed, hydrogen has come to the forefront of alternative fuels. Hydrogen produces no greenhouse gases when reacted with oxygen in air and it is an excellent clean energy carrier for the future of our transportation industry.

Hydrogen is utilized in many industries beyond transportation. Many processes exist to produce hydrogen, and many others are being researched. However, current methods are largely focused on transforming fossil fuels (about 97% is derived from fossil fuels) [5].

Current methods for producing hydrogen require fossil fuels and emit GHGs (for example, steam methane reforming produces carbon dioxide). Sustainable methods for producing

hydrogen are sought to circumvent these undesired outcomes. The ideal method of hydrogen production should have the following characteristics:

- the feedstock should be benign, not releasing GHGs,
- the production process should also not result in GHG emissions,
- the production process should be optimized for minimum input energy requirements, and
- the whole operation, including feedstock and processing, should be economical.

Based on these requirements, thermochemical cycles have shown promise as a feasible means of producing hydrogen sustainably. Among the most promising thermochemical cycles is the Copper-Chlorine cycle (Cu-Cl cycle), due to its relatively low temperature requirements (500°C versus 850°C for higher for other cycles).

As part of the Cu-Cl cycle, copper (II) chloride (both its anhydrous form and dcc – its dihydrate) is used as an electrolyte in the electrolytic cell. It is required later as an input for the hydrolysis reaction. Physical processing of this electrolyte is necessary to allow the dcc to be re-used in the cycle. The physical processing should take the least amount of input energy, and meet the demands of the feedstock and next step in the process. This thesis focuses on developing a model to allow for the product to meet the next step's demands, and to later allow for reduction of the energy input.

1.2 Thesis outline

A key goal of this thesis is to develop a better understanding of the characteristics for the various dcc electrolyte processing options, with specific detail on spray drying and convective drying. Aqueous cupric chloride, a product of the electrolysis reaction, is required as dry solid particles for the subsequent hydrolysis reaction.

Chapter 2 consists of background information on all relevant aspects of nuclear thermochemical hydrogen production, and the Cu-Cl cycle. Various configurations for this step are described. The limitations of the electrolytic cell and the requirements of the hydrolysis reaction are noted. A survey is then conducted in Chapter 3 to review previous experiments in processing dcc and its complexes. A rationale for choosing the Cu-Cl cycle, variations of the cycle itself, and options for the drying step, are discussed. Relevant research conducted with regard to dcc solution drying, spray drying, and convective drying is also discussed. Various parametric optimization results from previous spray drying studies are outlined.

Chapter 4 discusses drying from a phenomenological perspective. Drying is described qualitatively and various stages of drying are introduced, for both spray drying and convective drying. The drying arrangement with regard to equipment is discussed. Property models for each of the required electrolyte properties in the governing Equations are presented in Chapter 5. The mathematical background of the various options for drying is then presented in Chapter 6. The governing Equations are presented and non-dimensionalized. The process of non-dimensionalization determines which properties and parameters have significance in spray drying optimization.

Experimental materials and methods are discussed in Chapter 7. The experimental apparatus is explained with process and instrumentation diagrams. The experimental methods for determining each of the optimization parameters in Chapter 3 are outlined. All equipment used in experimentation and analysis is discussed.

Results of experiments, discussion, and analysis are shown in Chapter 8. Results of all experiments are analyzed comprehensively:

- Particle size as a function of various input parameters (solution input temperature, solution flow rate, air input temperature and flow rate, pressure differential),
- particle size distribution,
- residual volatile content (moisture content),
- drying rates as determined by convective drying,
- particle flowability, and
- particle morphology.

Discussion and analysis are carried out with respect to previously cited literature, with applications of the current Cu-Cl cycle. Tables and analyses are enclosed as appendices.

Finally, conclusions and recommendations based on the research are presented in Chapter 9. Experimental results on the Cu-Cl cycle are highlighted and future work is recommended. The potential of using spray drying as a step in the Cu-Cl cycle for thermochemical hydrogen production is appraised.

1.3 Motivation of Thesis

The Cu-Cl cycle is an excellent choice for clean hydrogen production and this research contributes to determine the most efficient ways of arranging the drying step. As part of this cycle, dcc electrolyte processing requires research to determine:

- Energy requirements during processing,
- Drying rates under various operating conditions,
- Property control for easy adaptation into the cycle (by accommodating a variation in feedstock and a narrow product variation).

Currently, there is insufficient data on dcc drying and processing to determine the most efficient ways of processing. To facilitate future research development of the Cu-Cl cycle, properties are required to be determined as well as dcc drying behavior under various conditions. Spray drying, one option of dcc processing, has yet to be studied. Spray drying experiments will be conducted in this thesis to optimize the spray drying process for re-processing dcc, and determining various parameter requirements at different input parameters.

Chapter 2

Background

2.1 Hydrogen production

With ever increasing hydrogen demand, sustainable methods for hydrogen production are needed. Sustainability in this context means no CO₂ emissions, and without the use of non-renewable resources. Several methods exist to produce hydrogen; however, current methods, such as steam methane reforming (SMR), are largely focused on extracting hydrogen from fossil fuels (about 97% is derived from fossil fuels) [5]. Electrolytic hydrogen production is available commercially, yet it is relatively more expensive compared to SMR.

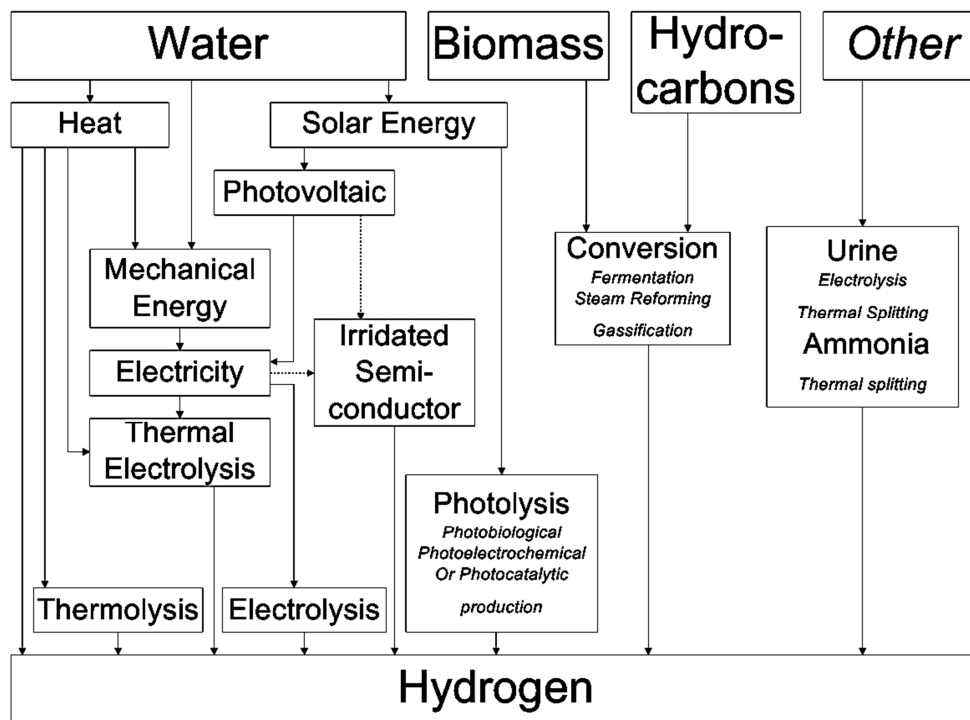


Figure 2.1: Various methods to produce hydrogen

A partial flow diagram of hydrogen production methods available commercially and currently being researched is shown in Figure 2.1. Research is also underway in biomass hydrogen production, using biomass gasification or steam reforming. Hydrogen can be produced directly through the thermal disassociation of water into hydrogen and oxygen, using high temperatures (2500°C). Solar hydrogen production research via photo-biological (e.g. algae bioreactors), photo-electro-chemical, or photo-catalytic methods have potential to produce hydrogen. Hydrogen can also be generated through thermochemical cycles (TCs), such as the Sulfur-Iodine, or Copper-Chlorine cycles which require input from a high temperature heat source.

Ultimately, economics determines the most viable hydrogen production method. Currently SMR is the most economical method. Recent advancements in drilling technology are keeping natural gas prices at historical lows in the near term. As consumption for power production increases however, natural gas prices will to increase. As shown in Figure 2.2, the next alternatives for hydrogen production in terms of cost are coal gasification (IGCC) or nuclear hydrogen production through the Sulphur-Iodine cycle (S-I cycle). Nuclear hydrogen production through the copper-chlorine cycle is still in the design stages of development.

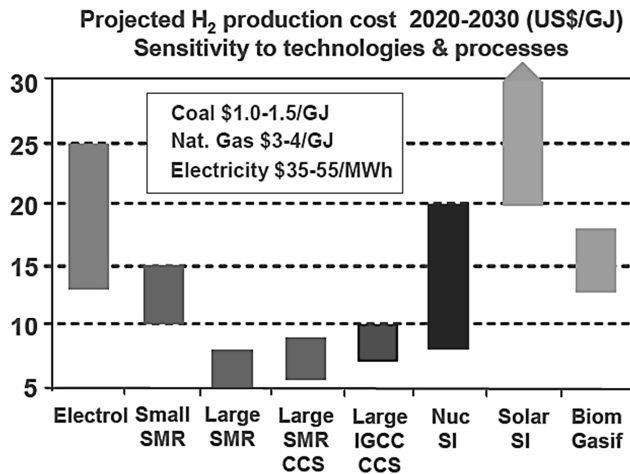


Figure 2.2: Projected cost of various hydrogen production methods [6]

2.2 Nuclear hydrogen production

Hydrogen can be produced by using heat for thermolysis. This water splitting chemical reaction is the basis of thermochemical hydrogen production methods. The key advantage is eliminating the need for fossil fuels, and thus, decreasing GHG emissions. To date, numerous TCs have been designed. By using various chemical configurations as catalysts, these cycles reduce the temperature required to produce hydrogen from water. The chemicals are recycled in TCs, effectively only using heat, water, and possibly electricity in electrolytic cells as inputs, and hydrogen and oxygen as the outputs.

The S-I and hybrid sulphur cycles have been developed by countries such as the USA, Japan, Italy, France, and others [7] [8]. The S-I cycle requires temperatures up to 900°C, while the copper-chlorine cycle requires temperatures up to 550°C. The Cu-Cl cycle has many potential savings over the S-I TC for hydrogen production [9]. The temperature requirements of the copper-chlorine cycle are much lower thereby making it feasible to integrate this cycle to generation IV supercritical or ultra-supercritical nuclear reactors. It potentially reduces difficult materials requirements. By using TCs, the raw materials for generating hydrogen are renewable,

and no GHGs are released to the atmosphere during production [10]. Table 2.1 shows a five-step configuration of the Cu-Cl cycle. A visual diagram of these steps is shown in Figure 2.3.

	Name	Reaction	T [°C]		Feed / Output
1	Hydrolysis	$2\text{CuCl}_2(\text{s}) + \text{H}_2\text{O}(\text{g}) \rightarrow \text{CuO} \cdot \text{CuCl}_2(\text{s}) + 2\text{HCl}(\text{g}) + \text{H}_2\text{O}(\text{g})$	375-400	Feed Output	Powder/granular $\text{CuCl}_2 + \text{H}_2\text{O}(\text{g}) + \text{Q}$ Powder/granular $\text{CuO} \cdot \text{CuCl}_2 + \text{HCl}(\text{g})$
2	Thermolysis O ₂ production	$\text{CuO} \cdot \text{CuCl}_2(\text{s}) \rightarrow 2\text{CuCl}(\text{l}) + 1/2\text{O}_2(\text{g})$	500-530	Feed Output	Powder/granular $\text{CuO} \cdot \text{CuCl}_2(\text{s}) + \text{Q}$ $\text{CuCl}(\text{l})$ salt + oxygen
3	Electrolytic cell	$2\text{CuCl}(\text{aq}) + 2\text{HCl}(\text{aq}) \rightarrow \text{H}_2(\text{g}) + 2\text{CuCl}_2(\text{aq})$	20-80	Feed Output	Powder/granular $\text{CuCl} + \text{HCl}(\text{l}) + \text{V}$ $\text{HCl} + \text{CuCl}_2$ slurry + $\text{Cu}(\text{aq})$
4	drying	$\text{CuCl}_2(\text{aq}) \rightarrow \text{CuCl}_2(\text{s})$	> 100	Feed Output	$\text{HCl} + \text{CuCl}_2$ slurry + Q Powder/granular $\text{CuCl}_2 + \text{HCl} + \text{H}_2\text{O}(\text{g})$
5	Hydrogen production	$2\text{Cu}(\text{s}) + 2\text{HCl}(\text{g}) \rightarrow 2\text{CuCl}(\text{l}) + \text{H}_2(\text{g})$	430-475	Feed Output	Electrolytic $\text{Cu} + \text{dry HCl} + \text{Q}$ H_2 gas + $\text{CuCl}(\text{l})$ salt

a: Q = thermal energy, V = electrical energy.

Table 2.1: Steps in the Copper-Chlorine Cycle [11]

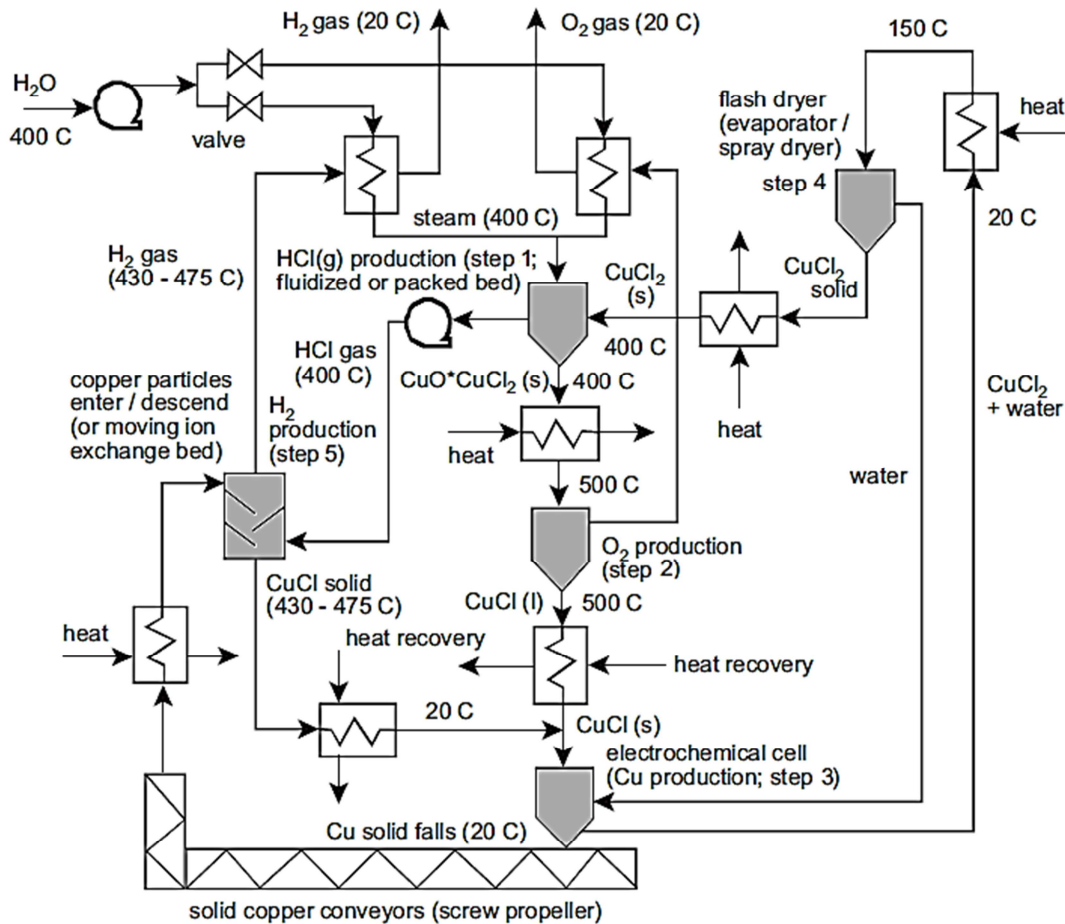


Figure 2.3: Schematic of the Copper-Chlorine Cycle [12]

2.3 Options for copper II chloride recovery

There are various configurations of the Cu-Cl cycle for hydrogen production. All are based on the original five step cycle, as shown in Table 2.1. There is also four, three, and two step cycles. The various configurations have their corresponding advantages and drawbacks as outlined by Orhan [11]. The processing of aqueous dcc solution is an essential step in both the five and four step cycles, both of which have the advantage of lower temperature requirements compared to the two and three step cycles. This thesis is based on the five-step cycle: aqueous dcc is a product of the electrolysis reaction (Step 3), and it is required as dry solid particles for the subsequent hydrolysis reaction in a fluidized bed (Step 1). For this cycle, fast and efficient recovery of aqueous dcc is essential (step 4). Some possible methods for recovering dcc from the electrolyte are shown in Figure 2.5.

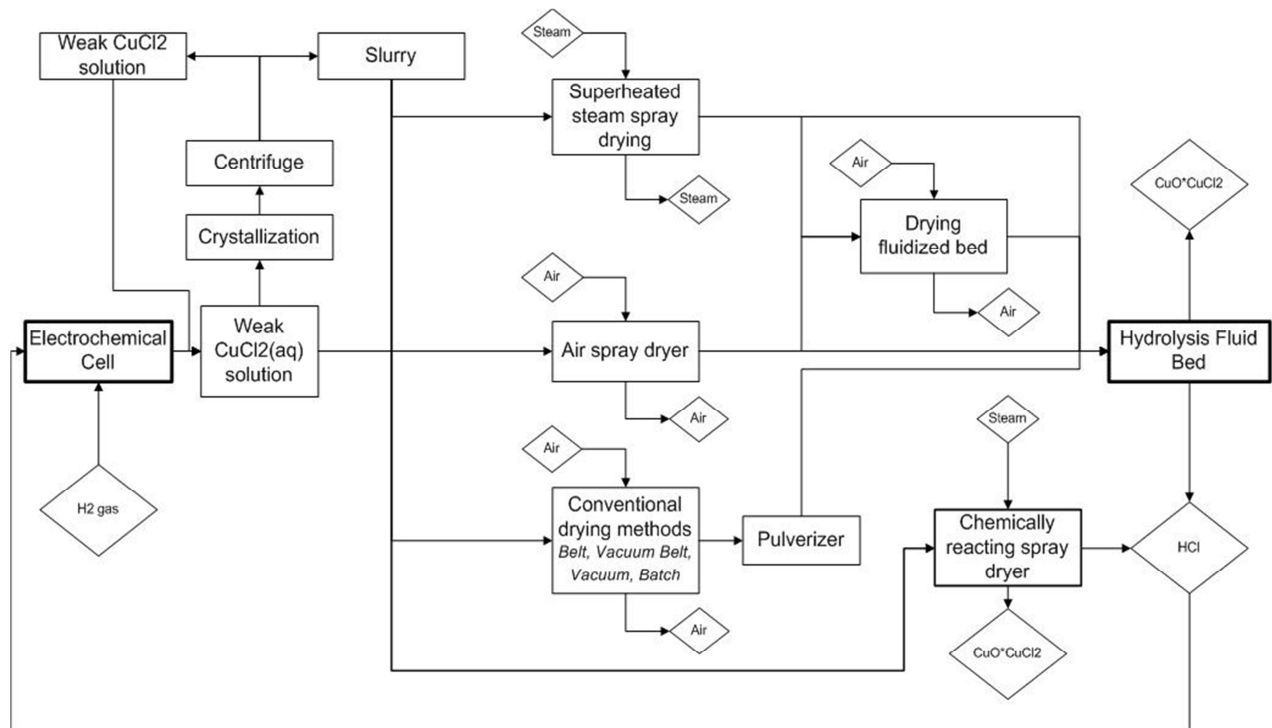


Figure 2.4: Summary of dcc processing options for the Cu-Cl cycle

The behaviour of dcc during processing, characteristics of the aqueous dcc feed, and the hydrolysis reaction feed requirements will affect the favorable path in Figure 2.5. To determine the most efficient conversion mechanism, measurements must to be taken of various parameters during processing using different processing methods, as well as collecting physical data related to the drying of dcc. The feed and product characteristics should also be determined. These parameters, and the characteristics of different processing methods, will affect which recovery process is ultimately chosen. One specific drying option, spary drying, will be studied in depth to determine its physical viability for dcc processing. Convective drying is also studied and modelled to determine drying rates at various temperatures. This information will be usefull in computer modelling of the drying step. Convective drying can be used to supplement other processes noted in Figure 2.5.

2.3.1 Limitations from the electrochemical cell

Studies have been conducted at AECL, Pennsylvania State University, Argonne National Laboratory, and UOIT on the electrolytic cell for hydrogen production in the Cu-Cl cycle [5]. The configuration of the cell is shown in Figure 2.6.

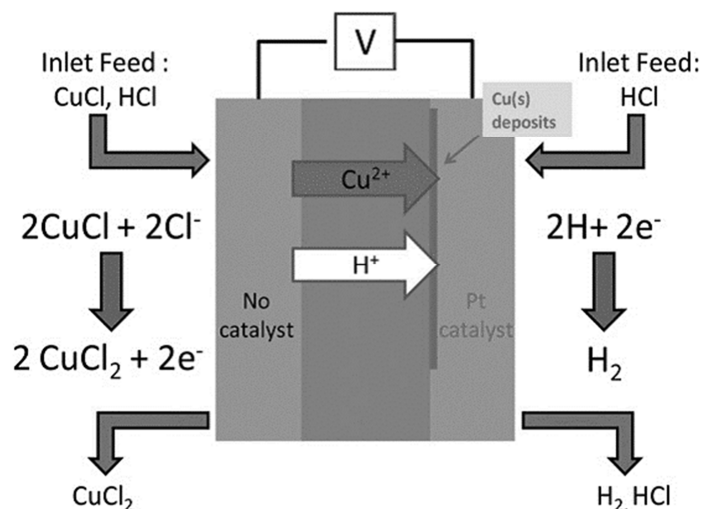
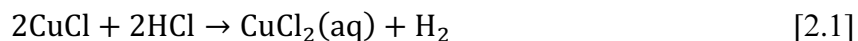


Figure 2.5: Schematic of the electrolytic cell

The overall cell reaction is shown as follows:



The anodic half reaction oxidizes copper I chloride. Depending on the concentration of the chlorine species, different copper species can form [13]:



There are complications with regard to copper species transferring across the membrane, and deposited at the platinum cathode at lower (6M) concentrations [13]. Therefore, it should be expected that used electrolyte will be in the 11M HCl solution, with about 85% of the dissolved copper forming as CuCl_2^{1-} , 10% as CuCl_3^{2-} , and 5% as CuCl^0 species [14]. This can be derived from the expected solution concentration, and Figure 2.7 below.

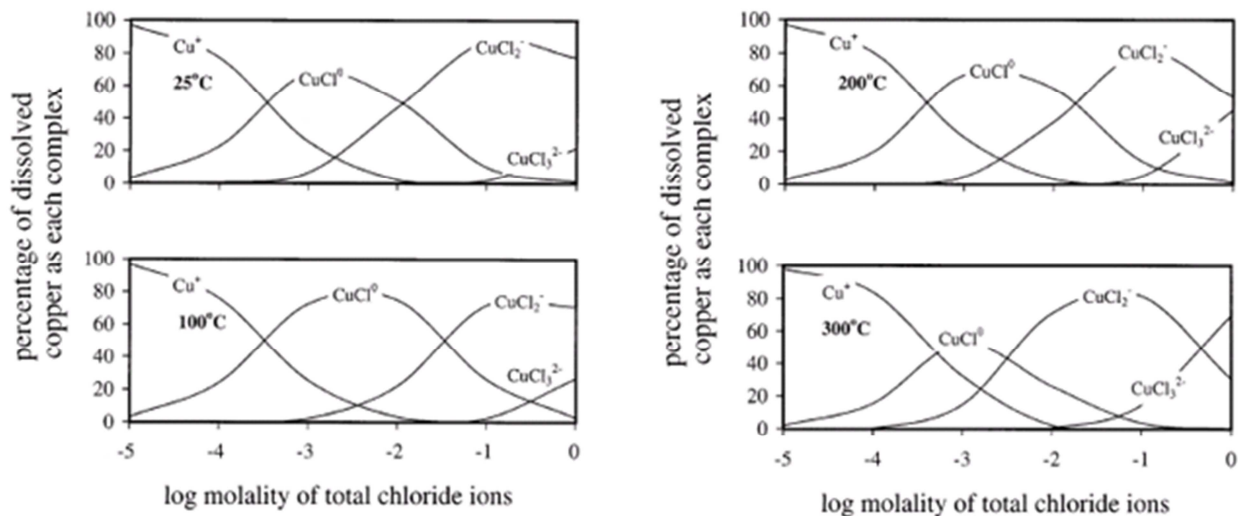
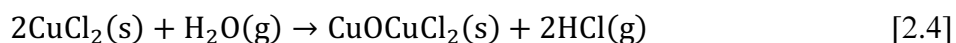


Figure 2.6: Percentage distribution of chlorocopper (I) complexes at different temperatures [14]

2.3.2 Requirements for the hydrolysis reaction

For a fluidized bed to be effective in the copper-chlorine cycle, dcc particles should have controlled properties to allow the fluidized bed to operate quickly, reliably, and predictably. The fluidized bed undergoes the following reaction:



From Equation 2.4, it can be seen that out of the two volatile compounds, excess hydrochloric acid in the feed will inhibit the reaction, and excess water will help the reaction. However, by the time the reactants (products from spray drying) are raised up to 300-400C, all volatile compounds will evaporate. Therefore, moisture inside the hydrolysis feed is not a problem. A previous study required particles larger than 40 μm to be generated in the spray dryer [15]. Recently, particles of 200 μm diameter have been assumed in a fluidized bed study [16]. Particles should flow as easily as possible: a narrow particle size distribution will help with this objective.

The particle morphology and density are strongly related to each other, since hollow particles have a much smaller particle size distribution. Friability, often important in powder treatment, is very important during the fluidized bed process. To enable fluidization in a fluidized bed, a narrow range of particle sizes exist based on the fluidized bed configuration. Therefore, good control of the final particle size in spray drying should allow the fluidized bed to operate in its designed fluidization regime. The particles should have a narrow particle size distribution, be durable, and a large surface area.

2.3.3 Fluidized bed operation

A fluidized bed operates under the principle that a fluid passing through a bed of particles can exert enough drag force on the particles to overcome their weight. The air flowing past the particles should overcome the terminal velocity of the particles, as shown in equation 2.5:

$$v_t = \sqrt{\frac{4gd_{3,0}(\rho_s - \rho_a)}{3\rho_a C_d}} \quad [2.4]$$

Where v_t is the terminal velocity, g is the acceleration due to gravity, d is the volume mean diameter of the particles (or equivalent diameter), ρ_s is the density of the particles, ρ_a is the density of the gas stream flowing past the particles, and C_d is the drag coefficient of the particles. The terminal velocity of the particles is highly dependent on the drag coefficient of the particles. Since the drag coefficient of the particles depends on the particle morphology, the spray-dried particle morphology is important in the later operation of the fluidized bed.

Chapter 3

Literature survey

3.1 Copper II Chloride and its industrial uses

Chemical systems containing copper II chloride have importance in many industrial applications. Its unique properties have allowed it to be used in many industries. This substance is ubiquitous, used in biological any enzymatic systems, agriculture, electronics, mining, photography, and energy applications among other applications [17] [18]. Copper chloride complexes catalyze several industrial and biological reactions, where the copper atom serves in electron transfer and redox processes. Common industrial uses occur in dyeing and printing of fabrics, as an ingredient of isomerization cracking catalysts, desulfurizing, and a deodorizing agent in the petroleum industry.

Various studies on industrial applications have been made on dcc. Polyachenok et al. [19] noted the advantages of using dcc over silica as a medium for desiccation, and studied the partial pressure of the substance as a function of temperature. Busscher et al. [17] studied the substance as it applies to biocrystallization as a means of authenticating agricultural products. The dcc concentration was noted as a function of evaporation time and solution temperature. Keskitalo et al. [18] noted copper chloride and its use in the printed-circuit board (PCB) industry as an etchant. Various patents for recovering the used dcc solutions were compared by Keskitalo et al. [18]. Under the same context of dcc recovery from etchant, Basir [20] studied the effects of using HCl as an additive to displace the copper and chlorine ions in solution, and recover the dcc from

used etchant. With specific interest to the copper chloride cycle, Zamfirescu et al. [21] conducted a survey of the current thermophysical properties of various compounds containing copper and chlorine of interest to the copper-chlorine cycle for nuclear hydrogen production. Due to the versatility of the substance, research continues to better understand these compounds.

3.2 Spray drying

Spray drying is often used in industry because of its excellent control of properties. Often, morphological studies are used to validate assumptions used in the governing fundamental Equations. The effects of process variables on desired outputs are studied to determine optimal parameters. The particle residence time, method and conditions of atomization, type of spray, air contact, drying temperature, and feed parameters (concentration, temperature, and degree of aeration) all govern the properties of the final product [22].

Previous investigations have been completed on spray drying of dcc and various other substances at low temperatures [23]. Various other substances have been studied for spray drying optimization and low temperature [24] [25]. Meenan et al. [26] used a counter current spray dryer with a 52% moisture burkeite slurry to determine property effects. It was found that six variables were the most important in determining the dependent variables in spray drying included the size of the spray nozzles, the atomizing pressure, the slurry flow rate, the air inlet temperature, the air inlet flow rate, and the air outlet temperature. Ambike et al. [24] used a lab-scale spray dryer to study amorphous particle dispersion at 35°C. Birchal et al. [27] used a lab scale spray dryer operating at temperatures between 160-200°C and studied the effects of operating variables on the powder quality of spray dried milk. For these experiments a rotating atomizer was used to dry the powders; however the influence or rotation on the atomization

variables was found to be negligible. Stahl et al. [25] used a lab scale spray dryer and determined the changes that physical properties underwent as the process variables were altered. Sachin and Bhaskar [28] dried ginger in a lab-scale spray dryer at temperatures from 120-160°C to determine product characterizations for commercial use.

Other studies specifically aimed at spray drying dcc for application in the Cu-Cl cycle were presented. Daggupati et al. [15] studied the effects of atomization conditions and flow rates on particle formation during cupric chloride, sodium bicarbonate, and sodium carbonate in a lab-scale spray dryer. Naterer et al. [23] [29] studied the effect of flashing on the drying efficiency, and developed a predictive model for the drying and flashing process. However, to our knowledge, there has been no comprehensive study to determine particle size morphology and optimization for dcc product use in a fluidized bed. The following Sections present a review of how various parameters change the spray drying product in the previously mentioned studies.

3.2.1 Particle size

Control of particle size is the most desired goal in spray drying. However, it is difficult to represent a whole array of particle sizes accurately in a powder. Often one particle size and droplet size are taken to represent the whole set. Various definitions of diameters are used in industry, as shown in Table 2. These various distributions are used to help with various types of industrial processes for which particles are used in different industrial processes, whereby volume, surface area, or the number of particles can be of greater importance. For spray drying, the Sauter mean diameter is most often used.

Name	Denotation	Value
Number mean diameter	d_{10}	$\sum d / N_p$
Surface mean diameter	d_{20}	$\sqrt{\sum d^2 / N_p}$
Volume mean diameter	d_{30}	$\sqrt[3]{\sum d^3 / N_p}$
Sauter mean diameter	d_{32}	$\sum d^3 / \sum d^2 = d_{30}^3 / d_{20}^2$

Table 3.1: Particle size definitions

Studies have been completed to determine how particle size is affected by various parameters. Correlations are often used to best describe these parametric influences on droplet or particle size. Stahl et al. [25] found that the particle size increases with decreasing nozzle flow. Birchall et al. [27] found a slight counter-current trend; however this was due to the rotary nozzle. Hede et al. [30] completed a comprehensive review of droplet size correlations for two fluid nozzles. Thybo et al. [31] also derived a correlation for spray dried particle size using results from a lab-scale study. These correlations are shown in Table 3. The conditions under which the correlation was completed and materials dried should be noted, since different materials can exhibit different drying characteristics under the same conditions. Ultimately, experimental verification of these correlations is required for use by different materials. Note that all correlations have a similar form except Gretzinger and Marshall [32]. The form of droplet correlations will be further discussed in Chapter 6.

3.2.2 Particle size distribution

Particle size distributions are affected by various parameters. Babinsky and Sojka [33] conducted a comprehensive particle size distribution survey and determined two ways were most often used to determine particle size distributions. The classical method, where modeling is empirically determined, is based on experimental results. Recently, analytical approaches have

Correlation	Conditions / materials	Parameters	Author/ Reference
$\frac{d_{32}}{d_0} = \left(1 + \frac{\dot{m}_{sol}}{\dot{m}_g}\right) \cdot X_2 \cdot \left(\frac{Oh}{We}\right)^{X_1}$	Water, ethanol, acetaminophen and PVP K-30 in ethanol Surface tension: 23-72 x10 ³ kg/s ² Liquid viscosity:0.9-20.2x10 ³ kg/m s Air pressure: atmospheric Air Temperature: 288-293 K M _{air} / M _{liq} = 1-35 Flow velocity: <sonic	Water: X ₁ =0.606; X ₂ = 1.19x10 ⁷ Ethanol: X ₁ =0.649 X ₂ = 1.31x10 ⁷	Thybo [34]
$d_{mmd} = 2600 \cdot \left[\left(\frac{\dot{m}_{sol}}{\dot{m}_g}\right) \cdot \left(\frac{\mu_g}{G_g \cdot L_c}\right)\right]^{0.4}$ $\log d_{mmd} = \log d_{32} + 1.1513 \cdot \log^2(s_g)$ $s_g = 1.77 \cdot d_{mmd}^{0.14}; d_{32} = 0.83 \cdot d_{mmd}$	50 aqueous solutions of black dye Surface tension: 50x10 ³ kg/s ² Air pressure: 1.6-4 kPa, Air Temperature: 295 K Liquid viscosity: 1.0x10 ³ kg/m s, M _{air} / M _{liq} = 1-16 Flow velocity: <sonic	N/A	Gretzinger and Marshall [30]
$\frac{d_{32}}{d_0} = 0.21 \cdot (Oh)^{0.0622} \cdot \left(We_g \cdot \frac{\dot{m}_g}{\dot{m}_{sol}}\right)^{-0.4}$	Water, glycerol, kaolin suspensions and CMC water mixtures Surface tension: 56-72x10 ³ kg/s ² Liquid density: 1000 – 1130 kg/m ³ Liquid viscosity: 1-8x10 ³ kg/m s Air pressure: 1.1-1.6 kPa Air Temperature: 293 K M _{air} / M _{liq} = 2-100 Flow velocity: <250 m/s	N/A	Mulhem et al. [32]

Table 3.2: Droplet size correlations for spray drying

been developed to predict the particle size distribution. Two methods, namely the maximum entropy method (ME), and the discrete probability function (DPF) method, both are non-deterministic methods to predict the final particle distribution based on different underlying assumptions. For the purposes of this thesis, the physical characteristics and changes between experiments were determined rather than a non-deterministic method for extrapolation of data. Thybo and Hovagaard [34] dried Table salt and milk powder, and determined that such data could be beneficial to determine which operating conditions would result in the same droplet size of a nozzle of similar design.

3.2.3 Moisture content

Generally, decreasing the water flow and increasing the heat flow decreases the moisture content of the dried particles. Birchal et al. [27] found that an increased inlet air temperature and increased solids concentration decreased the final moisture content; Stahl et al. [25] agreed with these findings. Sachin and Bhaskar [28] noted that at higher pressures smaller droplets are formed increasing the heat transfer surface area. This decreased the moisture content. Daggupati et al. [23] found that for dcc, higher temperatures decreased the moisture content but not linearly. Since dcc forms a dihydrate at 100°C, 120°C corresponds to the powder directly forming its anhydrous form. At lower temperatures, the powder is dried to a higher mixture of dihydrate due to a lower input energy.

3.2.4 Bulk density, flowability

Flowability has importance in the fluidized bed step following the spray drying step in the Cu-Cl cycle. Bulk density has been used as a measure of flowability of dried powders. It has

been determined that a lower Hausner ratio correlates to a more flowable powder [35] [36]. Both Xu et al. [35] and Abdullah [36] noted that a lower Hausner ratio meant a more flowable powder. Xu et al. [35] studied the flowability of spray dried B-carotene using three different methods of flowability measurement and tabulated different Hausner ratios vs. flowability. Abdullah [36] used two different types of particles (fluid cracking catalyst and non-porous fire retardant filler) to determine the best measure of flowability. Both determined that the Hausner ratio using a tap test produced an adequate measure. Daggupati et al. [23] found that the flowability of the drying powder for use in a fluidized bed, measured using the Hausner ratio is larger at higher temperatures. This could be due to a simultaneous decrease in moisture content at higher temperatures, which would decrease the Van der Waals cohesive forces at the surface due to the polar water molecules. Walton and Mumford [37] conducted a comprehensive study of particle morphology and found that particle size, size distribution, particle morphology (irregular vs. spherical shape), moisture content, and the hygroscopy of the powder all contributed to the flowability of the powder.

3.2.5 Outlet air temperature

The outlet air temperature was found to be almost directly related to the inlet air temperature. Stahl et al. [25] determined that both an increased inlet air temperature and decreased feed flow rate increased the outlet air temperature. Daggupati et al. [23] found the air outlet temperature to vary depending on the inlet air temperature, drying air flow rate, and atomization liquid flow rate. The outlet air temperature increases linearly with respect to the air inlet temperature and air flow rate, while decreasing with increasing atomization liquid flow rates.

3.2.6 Morphology and crystallinity of the spray dried particles

The morphology of spray dried particles was found to depend greatly on the dried material. Daggupati et al. [23] dried dcc and found that at temperatures greater than 120°C, the spray dried particles formed hollow spheres. However, at lower temperatures, some sharp-edged amorphous particles were formed. Interestingly, below 80°C, all particles were sharp-edged and amorphous. For the porosity and agglomeration of dcc particles, other dried substances can be compared. Walton [37] found that agglomeration occurred due to static electricity. Thybo et al. [31] dried acetaminophen and polvinylpyrrolidone K-30 and noted that at higher temperatures, the particle surface was much smoother. This happens because at higher temperatures, many smaller crystals are formed. Langrish [38] completed a study determining the crystallization behavior of sodium chloride and lactose.

Meenan et al. [26] found that spray dried burkite droplets had a high overall porosity due to crystals aggregating edge to face and edge to edge. The effective wall thickness of large and small particles didn't change. However, the bulk crystal in smaller particles is denser. Larger particles were also found to have a greater tendency to be hollow.

Ambike et al. [24] determined that additives can be used as a means of decreasing the crystallization of particles. Additives in spray drying dcc could be detrimental to the Cu-Cl cycle. These additives would build up due to a continuous need in spray drying and thus decrease the cycle efficiency.

3.3 Convective drying

Many previous experiments have been conducted to determine properties from convective drying of dcc. Mohamed and Halawy [39] completed non-isothermal TGA measurements on copper (II) chloride dihydrate efflorescence. Polyachenok et al. [19] [40] used tensimetric methods to measure the equilibrium water vapor pressure for the dehydration of solid cupric chloride dehydrate. Polyachenok [19] noted that technical issues with current experimental methods for thermodynamic quantities existed. Lower tensimetric methods were devised to measure the vapor pressure, enthalpy and entropy. Both papers noted that drying is a much faster process than re-hydrating CuCl_2 .

Busscher et al. [17] studied the influences of additives on the evaporation and subsequent dewetting and crystallization of various concentrations of cupric chloride solution. Keskitalo et al. [18] studied the removal of copper from spent dcc solutions in the PCB industry. However, most of the applications involve other chemical reactions, without reusing the final products in the cycle. To our knowledge, there are no studies on the drying rate of cupric chloride in slurry form, and no comparisons made with current literature. Further, the current literature focuses on lab scale experiments, using small samples in a TGA analyzer or similar equipment. Although these are useful precise measurements, these results must be verified with larger scale experiments to determine their scalability. Further, drying rate calculations were reported based on the experiments.

Although much research has been conducted on copper II chloride, most of the research was not focused on the Cu-Cl cycle. Further work is required with the goal of understanding the substance's behavior within the cycle, for reasons outlined in Chapter 2. Various fundamental

aspects of drying, such as determining particle size and distribution control, need to be determined to advance this research in the most expedited way.

Chapter 4

Drying Phenomena

For the purpose of this thesis, drying is defined as the vaporization of volatile substances by supplying heat to wet feedstock, yielding a dry solid product. Here, water is the volatile substance (at a later stage of research, hydrochloric acid will be added to properly model the full cycle). A liquid solution or slurry with dissolved solids is heated. Moisture vaporizes from the liquid, leaving a solid product. Moisture is divided into two groups:

1. Bound moisture: moisture exerting a vapour pressure higher than that of the pure liquid, often due to loose chemical combinations or vapour trapped in the microstructure.
2. Unbound moisture: moisture in excess of the bound moisture (exerts a vapour pressure equal to that of the pure volatile).

Bound moisture is entrained within the solid, after most of the bound moisture evaporates. At the air – solid boundary (surface evaporation), vaporization increases with increasing surface area, flow rate, supplied heat, decreasing the air moisture content, and decreasing the drying process pressure. Internal moisture is brought to the drying surface through [22]:

1. Liquid diffusion: The wet solid is below the liquid boiling temperature.
2. Vapour diffusion: above the boiling temperature, the liquid vaporizes within the material.
3. Differences in hydrostatic pressure: internal vaporization occurs faster than vapour transport through the solid to the surroundings.

As shown earlier in Figure 4, there are various options available for drying dcc. Spray drying is a good option because it is a good fit for later use in the fluidized bed (no need for a

pulveriser), and good control of properties. Energy requirements for spray drying of the initial electrolyte can be decreased by adding a conventional drying step before spray drying to increase the spray drying of feedstock solids concentration. The two courses of action studied here are:

1. Spray drying a lower concentration fluid, and
2. Conventional drying followed by spray drying.

The process of drying is complex with the simultaneous transfer of heat, mass and momentum. However for a single substance, the drying behaviour can be characterized by the rate at which moisture is lost as a function of time. In Figure 7, the first stage of drying involves vaporization of unbound liquid moisture, with surface diffusion controlling this rate. At the second stage, the critical moisture content, X_{cr} , has been reached. Dry spots appear on the surface and the surface becomes unsaturated, which is the start of the second stage of drying. The third stage of drying occurs when most or all the surface is dry, and the drying rate depends on concentration gradients between the surface and inner parts of the substance.

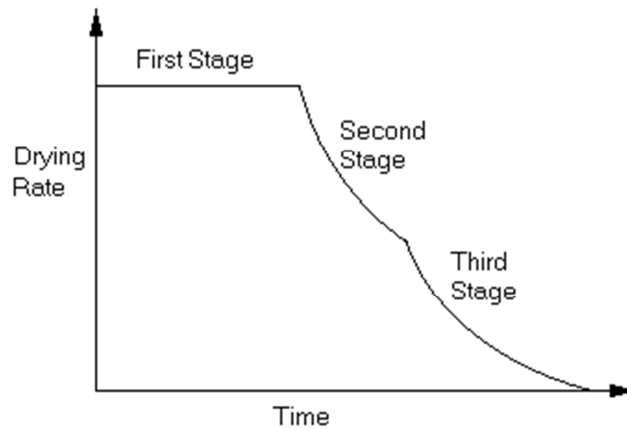


Figure 4.1: Drying rate curve at constant drying conditions

It is well known that CuCl_2 forms a di-hydrate at ambient conditions. When initially starting from a dilute aqueous solution of dcc, the initial drying can form anhydrous crystals or di-hydrate, depending on the temperatures and heat transfer.

4.1 Spray Drying

Spray drying uses liquid atomization to form suspended particles, increase surface area, and increase the drying rate. Droplets are dried in a continuous process using a hot gas, usually air. Spray drying is often used in industry because of its excellent control of product properties. It has found applications in various industries, with many different required particle morphologies [37]. Final product characteristics (powder bulk density, particle size and distribution, moisture content, particle morphology, surface structure, and particle flowability) can be controlled by controlling the process parameters (atomization liquid flow rate, atomization pressure, drying air inlet temperature, nozzle diameter and solid concentration in the liquid) during spray drying.

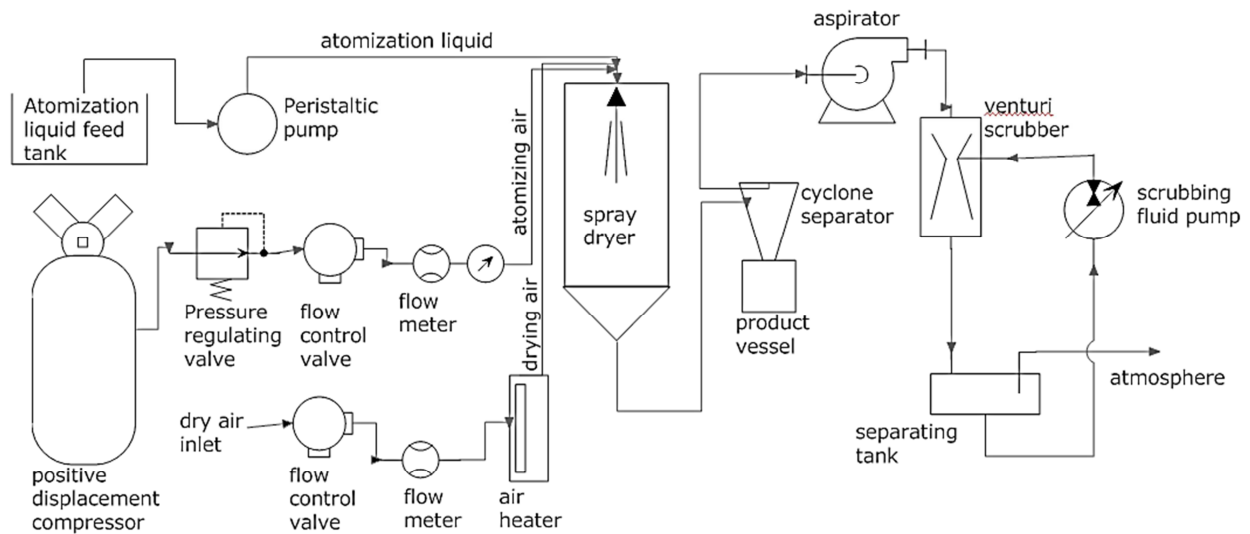


Figure 4.2: Schematic of spray drying apparatus

In a spray drying apparatus, shown in Figure 8, liquid solution is pumped with a peristaltic pump to the pneumatic atomization nozzle. Dry compressed air is mixed with the liquid solution in a two fluid nozzle as per Figure 9. Drying air is drawn from the atmosphere through a filter compressor through a flow valve to the electric heater. The dried powder product is separated

from the air using a cyclone separator. Before releasing the air, a venturi scrubber is used to clean the air free of any suspended particulate.

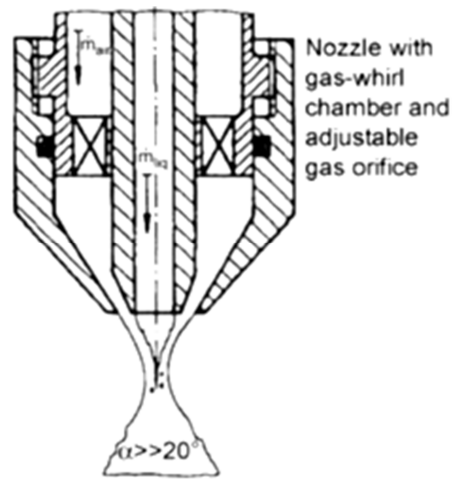


Figure 4.3: Two fluid pneumatic nozzle [30]

4.1.1 Dependence of nozzle type

The shape of the spray, and the gas-air contact characteristics are highly dependent on the type of nozzle used. Normally single-fluid nozzles do not find application in drying due to the absence of atomization – small particle sizes are needed for spray drying to be efficient. The main types of two-fluid nozzles can be subdivided into:

Externally mixing,

Internally mixing, and

Pneumatic cup atomizers (air and liquid contact at the rim of a rotating nozzle)

There is a compromise between two fluid nozzles in either high specific gas consumption, limited gas flow rates, wide droplet distribution, modest liquid flow capacities, or a combination of any of these limitations. Generally, to maintain the same droplet size while scaling nozzles, the gas to liquid ratio increases (more gas is required); this is much more pronounced with

externally mixing nozzles compared to internally mixing nozzles. To produce the same small droplet size, internally mixing nozzles require less gas than externally mixing nozzles. This is due to higher energy transfer rates with internally mixing nozzles.

This study uses externally mixing nozzles due to a simpler design. The correlations are generally not transferable from one nozzle type to another (external vs. internal). Further studies should include internally mixing nozzles, where air flow rate will decrease, and the subsequent filtration equipment will decrease as well. Great advances have also been made in superheated steam nozzles. These would have a great advantage in the copper chlorine cycle processing equipment for spray dried air would be decreased. Alternatively, air recirculation could be incorporated for the drying air in the spray dryer.

4.1.2 Fluid mechanics

For dcc, the droplet initially behaves as an electrolyte. Due to a high pressure upon leaving the nozzle, the liquid is atomized and a fine spray is formed. This process is known as pneumatic atomization. Since most nozzle designs involve two fluids, this is often called two-fluid atomization. The liquid in the middle of the nozzle is subject to a high velocity gas leaving the outside ring of the nozzle. The difference in velocities of the liquid and gas causes the gas to shear the liquid. Shearing causes disturbances in the liquid jet. It is governed by properties such as viscosity, surface tension, and density. Atomization is often divided into two separate regions: primary and secondary atomization. Primary atomization deals with the jet breaking up into particles due to instabilities, while secondary atomization deals with the droplet-droplet interaction and droplet interaction with the surrounding media, often described by the Weber number.

In primary atomization, high velocity air penetrates the lower velocity liquid, transferring energy, causing disturbances, and forming a spray. However, a larger liquid feed rate will not generate a large enough shear force to break apart the liquid jet. The most classical analysis of jet breakup was done by Raleigh [41], which assumed perturbations of a prescribed form, and determined breakup modes of liquid jets. The process of forming droplets involves shear forces vibrating the jet to form ligaments. These ligaments are then further broken into droplets, as shown in Figure 10.

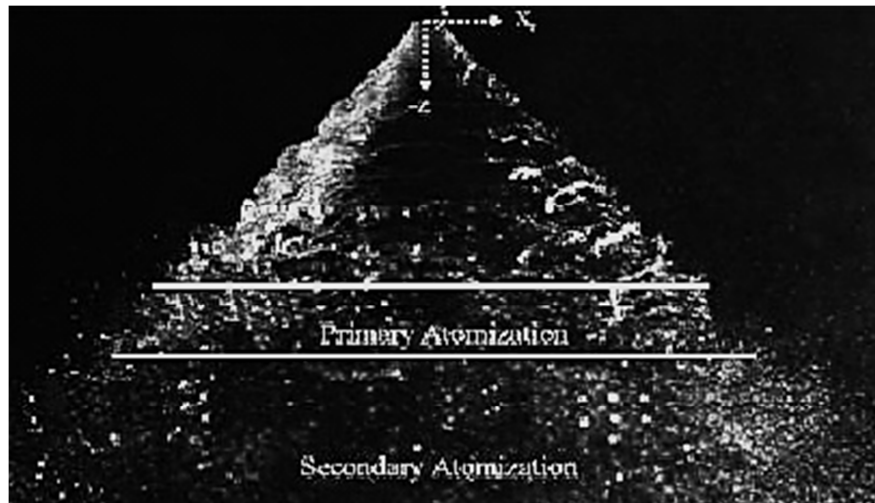


Figure 4.4: Atomization regions of the spray from a two fluid nozzle [42]

At this point, when the ligaments break into droplets, secondary atomization begins. Here, the main concerns are the droplets' interactions with the surrounding gas, and droplet-droplet collisions causing coalescence or further breakup. In spray drying, the time frames of droplet breakup determine the degree of secondary atomization. Since drying droplets become viscous and can form hard shells, these droplets require much greater forces for further breakup.

4.1.3 Heat transfer

The initial liquid jet leaving the spray drying process is normally at ambient conditions. Therefore, upon initial breakup, the jet is also being heated to saturation conditions. As the temperature of the liquid increases and droplets are formed, the droplet becomes more saturated with solute, as the first stage of drying begins (Figure 7). Once saturation conditions exist, crystal nucleation starts and a crust is formed out the outer surface of the droplet. Due to capillary action, the surface of the droplet remains wet at this stage. Depending on the drying energy of the droplet compared to the water to be evaporated, the droplet may form a crust all around or may only form a crust at the side of the droplet. Shear forces on the outside of the droplet will move nucleation points to one side of the droplet as the fluid inside is transported due to surface shear stresses. This process is shown in Figure 11.

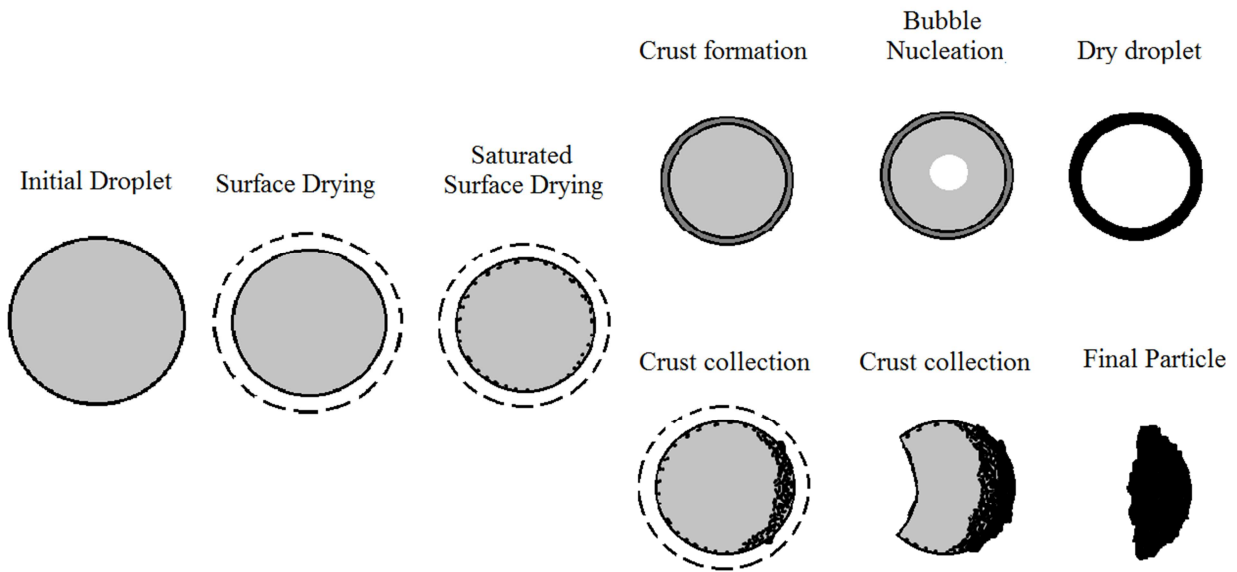


Figure 4.5: Droplet drying process

As more solution is brought to the surface of the particle, a smooth surface is formed. This fine surface fills in any pores found on the surface. As drying continues, the second stage of

drying begins as the surface of the particle becomes dry and the wet core shrinks within the particle. Evaporation occurs within the droplet and it is controlled by the mass transfer of moisture within the crust. Mechanisms of moisture movement during the non-saturated surface drying period may cause particles to inflate, distort or shrink. Some may form an internal or external skin, the particles may crack, case harden, or fracture completely, giving dust. If, after the crust is formed, its porosity is too low to allow vapour to escape, moisture will escape from the centre of the crust through a blowhole. Blowholes, as show in Figure 12, are evidence of internal water evaporation and a shrinking drying core.

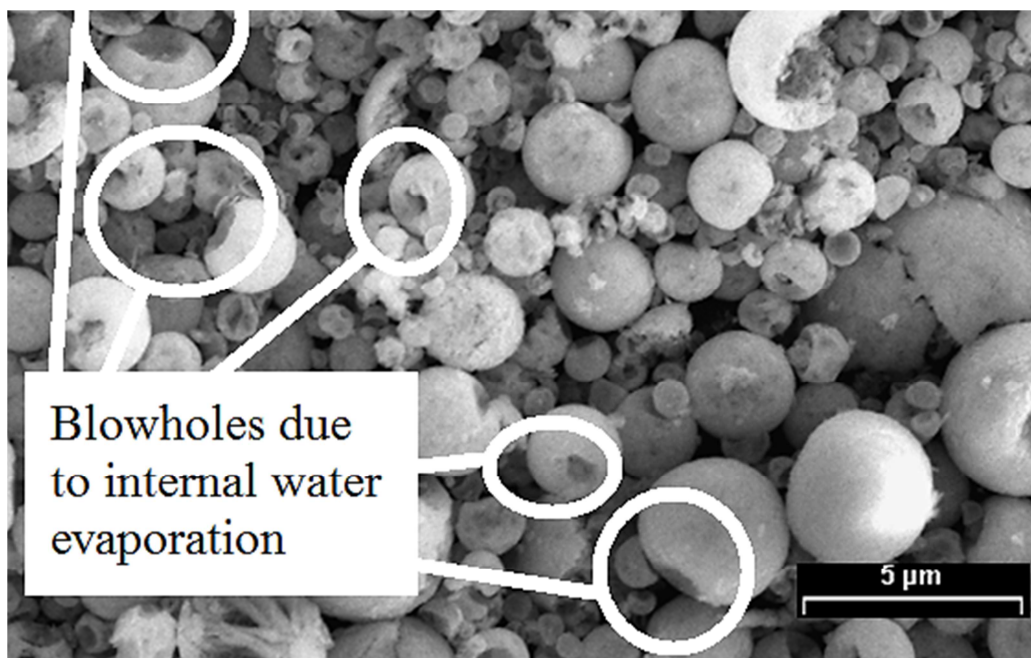


Figure 4.6: SEM of spray drying Run #25 - example of blowholes

Cupric Chloride can form a dihydrate or an anhydrous crystal. Depending on the ambient conditions, the crystal that is initially formed during drying can either be the dihydrate, if ambient conditions are below 100°C, or the anhydrous form. If the di-hydrate is formed, complete drying will require further removal of chemically bound moisture. This temperature-preferential crystal formation will affect nucleation rates during spray drying.

4.2 Convective drying

Convective drying employs a conventional oven to remove moisture from solids and liquids. To help determine liquid drying rates and energy requirements for liquid or particle processing, a drying oven is used. The fluid mechanics problem is simplified to boundary layer flow above a drying liquid or slurry. Temperature dependence in crystal formation can be studied in isolation. Figure 13 below shows the drying oven that was used for this work.

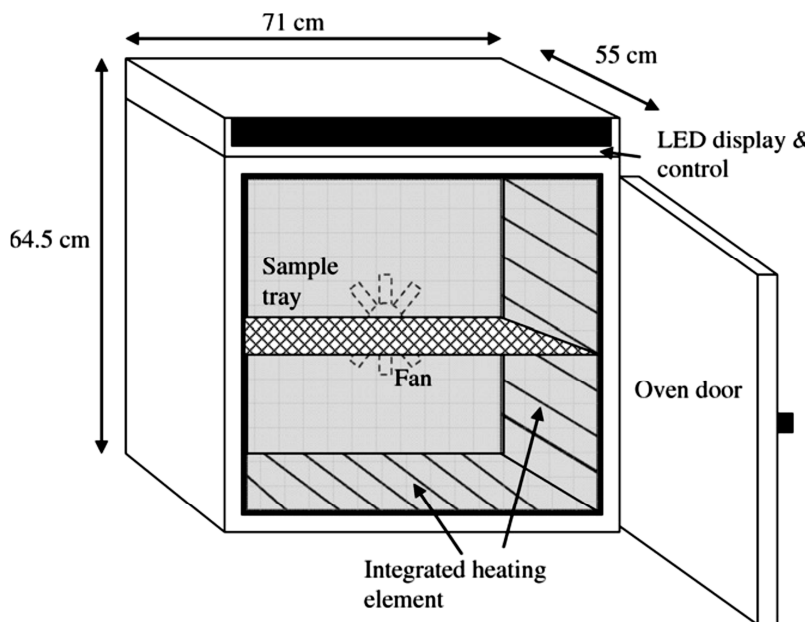


Figure 4.7: Conventional drying oven

Chapter 5

Physical Properties

5.1 Property estimation

In the preceding Chapter, mathematical models of the physical phenomena in spray drying require the knowledge of certain thermodynamic and transport properties. To use these mathematical models in a predictive capacity, the thermodynamic and transport properties need to be presented in a parametric form, allowing the properties to be determined at various conditions during spray drying. This Chapter describes the models used to determine properties under various conditions.

To calculate air properties, the partial pressure of dry air was assumed constant throughout the process. To determine properties inside the spray dryer, the initial relative humidity at ambient conditions was transformed into an equivalent relative humidity at the drying temperature using the following Equations:

$$fs = 1.00062 + 3.14 \cdot 10^{-8} p_a + 35.6 \cdot 10^{-7} T^2 \quad [5.1]$$

$$x_g = (RH/100)(p_{sat}(T)/101325)fs \quad [5.2]$$

where fs is an enhancement factor used for ideal gas applications of water vapor, as defined by Rasmussen [43].

After these calculations, the relative humidity at the hot air conditions was determined with Equation 5.3:

$$RH(hot) = (x_g \cdot 100 \cdot 101325)/(p_{sat}(T) \cdot fs) \quad [5.3]$$

The absolute humidity of the incoming air did not change during the heating process.

5.1.1 Diffusion coefficient

The diffusion coefficient needed to analyze mass transfer. Diffusion is often four to five orders of magnitude higher in air than water. Diffusion in fluids occurs due to random particle motion. The average distance travelled between collisions in liquids is less than the molecular diameter, while in gases, the mean free path is many times larger than the volume of the molecule. This allows molecules to penetrate gases farther and faster in gases without being re-directed.

5.1.1.1 Air – vapor mixture

A diffusion Equation by Gilliland et al. [44] based on kinetic theory is shown below:

$$\mathfrak{D} = (435.7 \text{cm}^2 \text{s}^{-1}) \frac{T^{3/2}}{p_b (V_w^{1/3} + V_a^{1/3})^2} \sqrt{\frac{1}{m_w} + \frac{1}{m_a}} \quad [5.4]$$

where p_0 in Pa is the surrounding gas pressure, V_w and V_a are the molecular volumes of water vapour and air, and m_w and m_a are their respective molecular weights.

However, Reid et al. [45] noted this Equation has errors of $\pm 10\%$. Therefore the following empirical Equation, valid for $[293 \text{ K} < T < 373 \text{ K}]$, was used [46]:

$$\mathfrak{D} = 1.87 \cdot 10^{-10} T - 3.33307 \cdot 10^5 \quad [5.5]$$

where \mathfrak{D} is in m^2/s and T is in K.

5.1.2 Density

5.1.2.1 Air – vapor mixture

The density of the air-vapor mixture is obtained by Equations 5.6 – 5.10, based on a simple mass balance and the ideal gas law:

$$p_w = \frac{RH}{100} p_{w,sat}(T) \quad [5.6]$$

$$x_a = \frac{101325}{101325 + p_i} \quad [5.7]$$

$$x_w = 1 - x_a \quad [5.8]$$

$$m_{tot} = x_a m_a + x_w m_w \quad [5.9]$$

$$\rho_{av} = 101325 * m_{tot} / (RT) \quad [5.10]$$

An assumption was made that the dry air pressure was 101325 Pa at all times, as no pressure measurements inside the spray dryer were taken.

5.1.2.2 Electrolyte

Cupric chloride has a density of 3.4 g/cm^3 in its anhydrous form, while its dihydrate density is 2.51 g/cm^3 . For the aqueous solution of water and copper II chloride, the density model developed by Laliberte and Cooper [47] is used. Equation 5.8 is used to calculate the density of water:

$$\rho_w = \frac{\left[\left(\left(\left(\left(c_1 T + c_2 \right) T - c_3 \right) T - c_4 \right) T + c_5 \right) T + c_6 \right]}{[1 + c_7 T]} \quad [5.11]$$

where T is in °C. Then Equation 5.9 is used for the density of the aqueous solution:

$$\rho_m = \frac{1}{\frac{x_w}{\rho_w} + w_{CuCl_2} \left((x_{CuCl_2} + c_3 + c_4 T) / (c_1 w_w + c_2) e^{(c_6(T+c_5)^2)} \right)} \quad [5.12]$$

where T is in °C. The coefficients for the correlations are shown in Table 4 below.

Coefficient	Water Density	Electrolyte density
c_1	$-2.8054253 \times 10^{-10}$	1868.5
c_2	1.0556302×10^{-7}	1137.20
c_3	4.6170461×10^{-5}	0.07185
c_4	0.0079870401	0.002565
c_5	16.945176	575.7
c_6	999.83952	0.000001
c_7	0.01687985	

Table 5.1: Electrolyte density model coefficients

The values for this model are shown below in Figure 14:

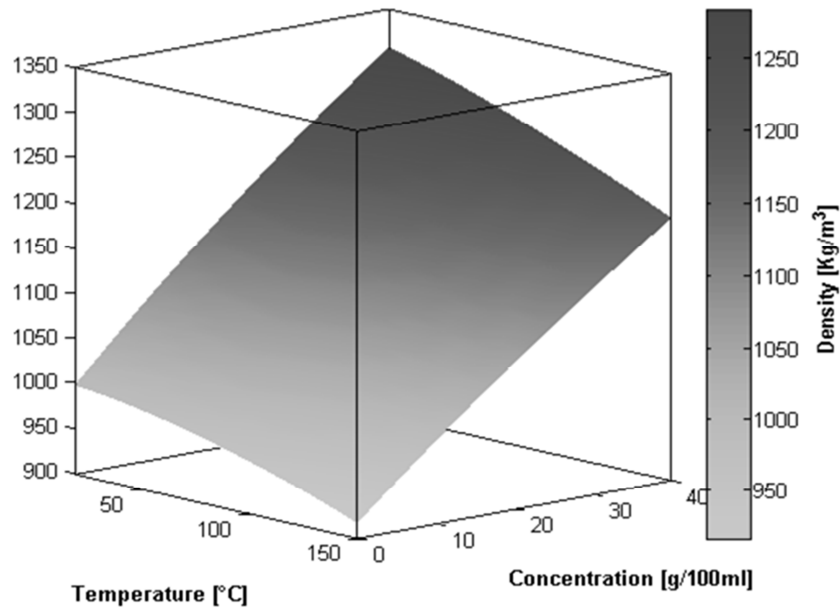


Figure 5.1: Electrolyte density model

5.1.3 Viscosity

Viscosity characterizes the resistance a fluid to shear or tensile stresses. All fluids in this thesis were considered to be Newtonian, where the shear stress between uniform, identical, parallel layers of fluid is directly proportional to the perpendicular velocity gradient:

$$\tau = \mu \frac{\partial u}{\partial y} \quad [5.13]$$

where μ is the viscosity, τ is the x-direction shear stress, and $\frac{\partial u}{\partial y}$ is the velocity gradient of the x-direction flow with respect to its perpendicular y-direction.

5.1.3.1 Air-vapor mixture

The following Equation was used for the viscosity of air [48]:

$$\mu_a = (c_1 + c_2T - c_3T^2 + c_4T^3 + c_5T^4) \times 10^{-6} \quad [5.14]$$

where μ_a is in MPa·s and T_b is in K. For the viscosity of water vapor, the following Equations were used [48]:

$$a = b = c_1 + c_2(c_3/T) + c_4(c_3/T)^2 - c_5(c_3/T)^3 \quad [5.15]$$

$$b = c_4(T/c_3)^{0.5} \quad [5.16]$$

$$\mu_{wv} = (a/b) \times 10^{-6} \quad [5.17]$$

where T is in K. The coefficients for the air-vapor correlations are shown in Table 5.

Coefficient	Water Density	Electrolyte density
c_1	0.40401	0.0181583
c_2	0.074582	0.0177624
c_3	5.7171×10^{-5}	647.27
c_4	2.9928×10^{-8}	0.0105287
c_5	6.2524×10^{-12}	0.0036744

Table 5.2: Air viscosity model coefficients

5.1.3.2 Electrolyte

The viscosity model developed by Laliberte [49] is used. Equation 5.8 is first used to calculate the viscosity of water:

$$\mu_w = [T + c_1] / [(c_2 \cdot T) + c_3]T + c_4 \quad [5.18]$$

where μ_w is the viscosity of water in MPa·s, and T is in °C. The viscosity of the aqueous electrolyte solution is calculated by Equation 5.9 [50]:

$$\ln(\mu_{sol}) = x_w \ln(\mu_w) + x_{CuCl_2} \frac{[c_1(1-w_w)^{c_2} + c_3]}{[(c_4 \cdot T + 1)(c_5(1-w_w)^{c_6} + 1)]} \quad [5.19]$$

The coefficients for the correlations are shown in Table 6 below.

Coefficient	Water Viscosity	Electrolyte viscosity
c_1	246	6.9303
c_2	0.05594	1.8668
c_3	5.2842	7.4786
c_4	137.37	0.0060045
c_5		65.035
c_6		0.15662

Table 5.3: Viscosity Equation coefficients

The values for this model are shown below in Figure 15.

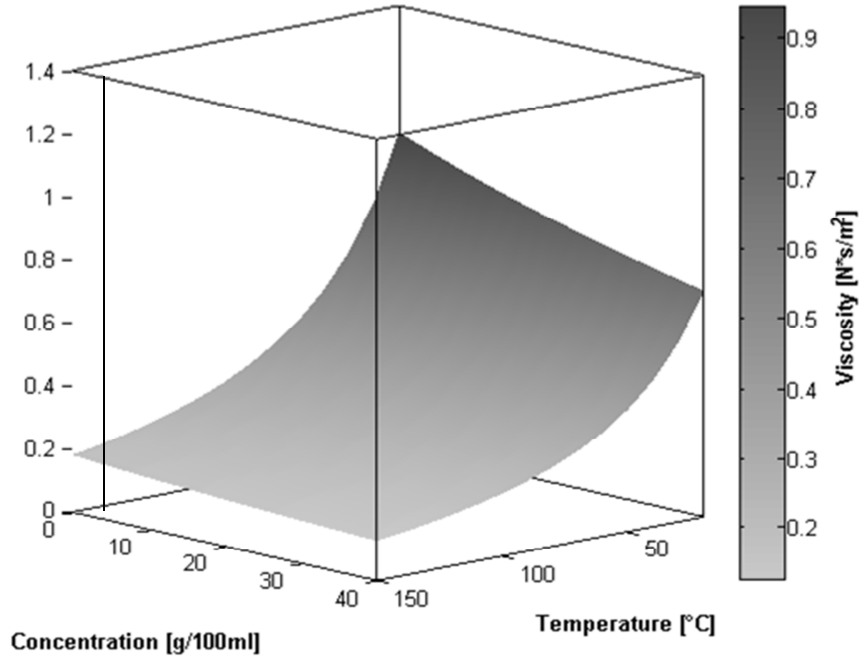


Figure 5.2: Electrolyte viscosity model

5.1.4 Surface tension

Surface tension is a property of the surface of a liquid, allowing it to resist an external applied force. The property involves the tension at the boundary between two phases, so only one property is required. When the two phases have the same pressure, the surface remains flat. However, if one phase has a higher pressure than the other, the surface must curve to relieve the pressure. The Equation describing this force balance (and the differential pressure) is the Young-Laplace Equation:

$$\Delta p = \sigma \left(\frac{1}{R_x} + \frac{1}{R_y} \right) \quad [5.20]$$

where σ is the surface tension in Pa·m, R_x and R_y are the radii of curvature of the surface in m, and Δp is the pressure differential across the surface in Pa. To determine the surface tension of the aqueous electrolyte solution, start with the surface tension of water [51]:

$$\sigma_w = c_1 \left(\frac{c_2 - T}{c_2} \right)^{c_3} \cdot \left[1 - c_4 \left(\frac{c_2 - T}{c_2} \right) \right] \quad [5.21]$$

Where σ_w is the surface tension of water in mN/m, and T is the temperature in K. To calculate the surface tension of electrolyte, the modified mean spherical approximation (MSA) of Yu et al. [52] is used. In MSA, the surface layer is assumed to be separate from the bulk liquid and gas phases. The chemical potentials of the bulk liquid and surface phases are:

$$\mu_w^B = \mu_w^{0B} + RT \ln a_w^B \quad [5.22]$$

$$\mu_w^S = \mu_w^{0S} + RT \ln a_w^S - \sigma \bar{A}_w \quad [5.23]$$

where R is the universal gas constant, T is the temperature in K, \bar{A}_w is the partial molar surface area, a_w is the activity of water, B and S refer to the bulk and surface phases, and w refers to the water. Using the phase equilibrium condition, the following Equation is obtained:

$$\sigma \bar{A}_w = \sigma_w A_w + RT \ln \left(\frac{a_w^S}{a_w^B} \right) \quad [5.24]$$

Yu [52] noted that \bar{A}_w is often assumed as:

$$\bar{A}_w = A_w \quad [5.25]$$

The osmotic coefficient can be used to calculate water activity of a single electrolyte solution:

$$\ln a_w = - \frac{vm\phi}{55.51} \quad [5.26]$$

where v is the stoichiometric coefficient of the electrolyte, equal to $v = v_+ + v_-$, m is the molality of the solution, and φ is the osmotic coefficient. Substituting Equations 5.26 and 5.25 into 5.24:

$$\sigma = \sigma_w + \frac{vRT}{A_w} \ln(m_b \varphi_b - m_s \varphi_s) \quad [5.27]$$

where m_b and m_s are the molalities of the bulk and surface phases, respectively. Also, m_s , the molality of the surface phase is calculated by:

$$m_s = m_b \left[1 - \frac{\beta}{1 + \left(\frac{vm^B}{55.51}\right)} \right] \quad [5.28]$$

where β is a fitting parameter. Though β was not found for CuCl_2 , it was found for other compounds shown in Table 7:

Compound	β Value
CaCl_2	0.0791
MgCl_2	0.0591
SrCl_2	0.1294
LaCl_2	0.2418

Table 5.4: β fitting parameter for various chlorine compounds

The value for m_b was measured at the initial point in each experiment. For the osmotic coefficient it, was assumed that $\varphi_b = \varphi(m_b)$, and $\varphi_s = \varphi(m_s)$. Goldberg [53] published osmotic coefficient tabular data for various compounds including dcc. A curve was fitted to published data, with an R-squared fit value of 0.9993, as shown in Figure 16.

$$\varphi = 0.52 \cdot \ln(m + c_1) + \frac{1}{c_2(m+c_3)} + c_4 + c_5 m + c_6 m^2 + c_7 m^3 + c_8 m^4 \quad [5.29]$$

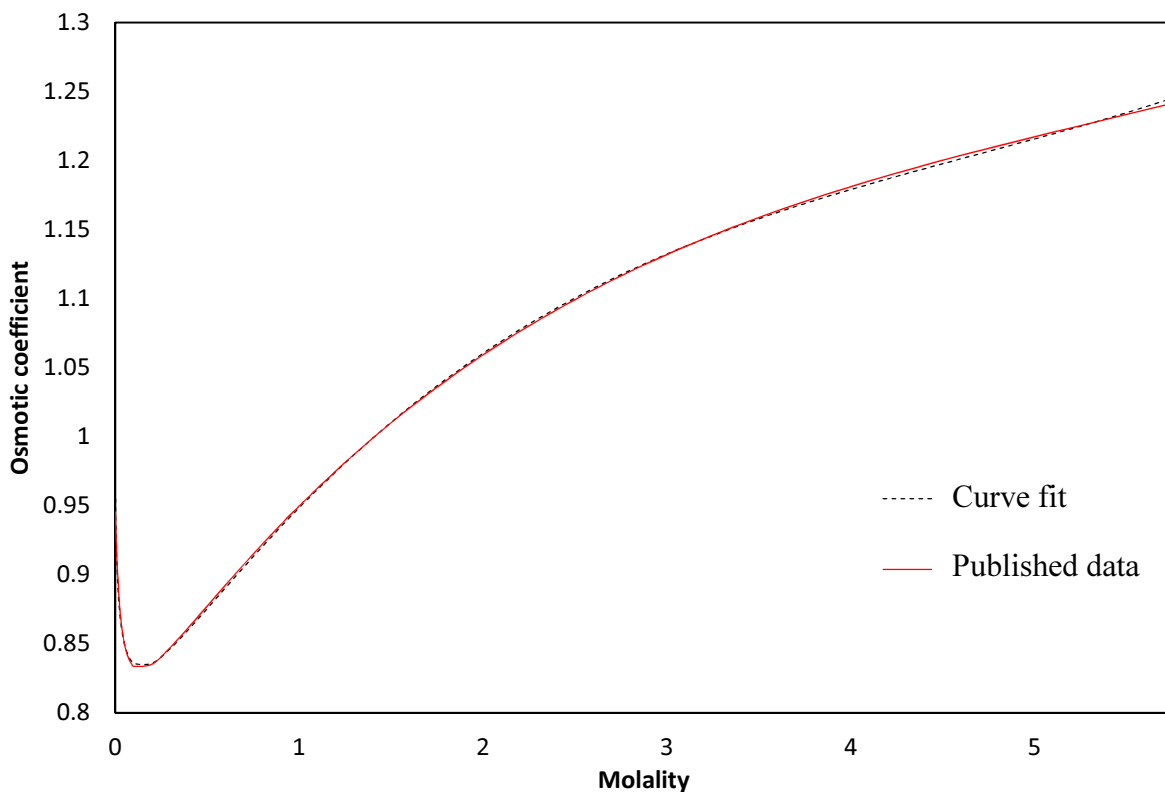


Figure 5.3: Osmotic coefficient data fit

Equations 5.21, and 5.26-5.29 form the complete model used to determine the aqueous electrolyte surface tension with air. The various coefficients for these Equations are shown in Table 8 below.

Coefficient	Osmotic coefficient	Water Surface tension
c_1	2.18	235.8
c_2	170	647.15
c_3	0.032	1.256
c_4	0.362	0.625
c_5	-0.0139	
c_6	-0.0058	
c_7	0.00009	
c_8	0.0000516	

Table 5.5: Surface tension coefficient data

To accurately determine the value for β , using the Equation, $h = \frac{\sigma \cos\theta}{\rho g d}$ the surface tension can be found using a tube of a specified diameter. Nine measurements of density, viscosity, and surface tension were made at different CuCl_2 concentrations. The results of which are shown in Appendix A. It was found that $\beta = 0.06$ fit to the data adequately. This fits with the other published data, as copper is heavier than the compounds with a smaller β , but lighter than those with a larger β . The values for this model are shown below in Figure 17.

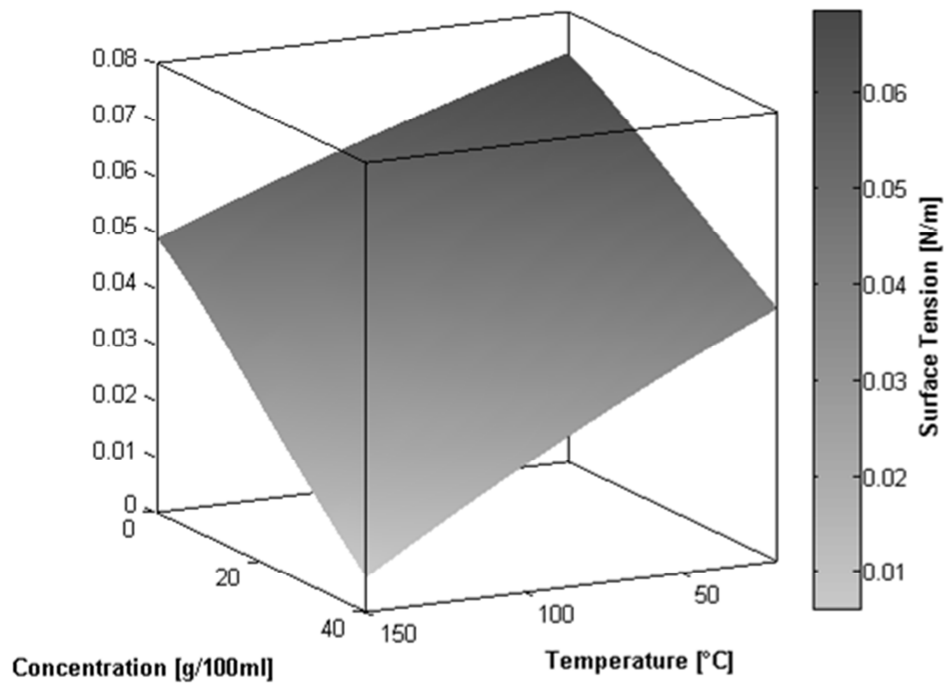


Figure 5.4: Electrolyte surface tension model

5.1.5 Thermal conductivity

Thermal conductivity or the ability of a body to conduct heat from molecule to molecule is described by Fourier's law of heat conduction:

$$\vec{q} = -k\nabla T \quad [5.30]$$

where \vec{q} is the heat flux density, ∇T the local negative temperature gradient, and k is the thermal conductivity. The thermal conductivity of liquids is an order of magnitude higher than the gas, due to closer molecules.

5.1.5.1 *Air-vapor mixture*

The following Equation is used for the thermal conductivity of air [54]:

$$k_{bg} = 1.5207 \cdot 10^{-11}T^3 - 4.8574 \cdot 10^{-8}T^2 + 1.0184 \cdot 10^{-4}T - 0.00039333 \quad [5.31]$$

where T is in K. The effects of water vapor were found to be insignificant.

5.1.5.2 *Electrolyte*

The most common thermal conductivity Equation for electrolyte solutions is (Riedel [55]):

$$k = k_w + \sum_i \alpha_i c_i \quad [5.32]$$

where λ_w is the thermal conductivity of water, α_i is the contribution of ion i , and c_i is the molar concentration of ion i . The thermal conductivity of pure water is [54]:

$$k_w = 0.57109 + 0.0017625 \cdot T - 6.7036 \cdot 10^{-6}T^2 \quad [5.33]$$

where T is in K. The contributions for each ion in CuCl_2 is taken from Wang and Anderko [56] shown in Table 9:

ion	C_{1,H_2O}	C_{2,H_2O}
Cu^{2+}	-0.975 205	-0.098 87
Cl^-	-0.360 439	0.006 076

Table 5.6: α coefficients for selected aqueous ions

Wang and Anderko [56] note that Equation 5.32 is only valid for dilute solutions. For the purposes of this study, Equation 5.32 will be used. A visualization of the electrolyte thermal conductivity model is shown in Figure 18.

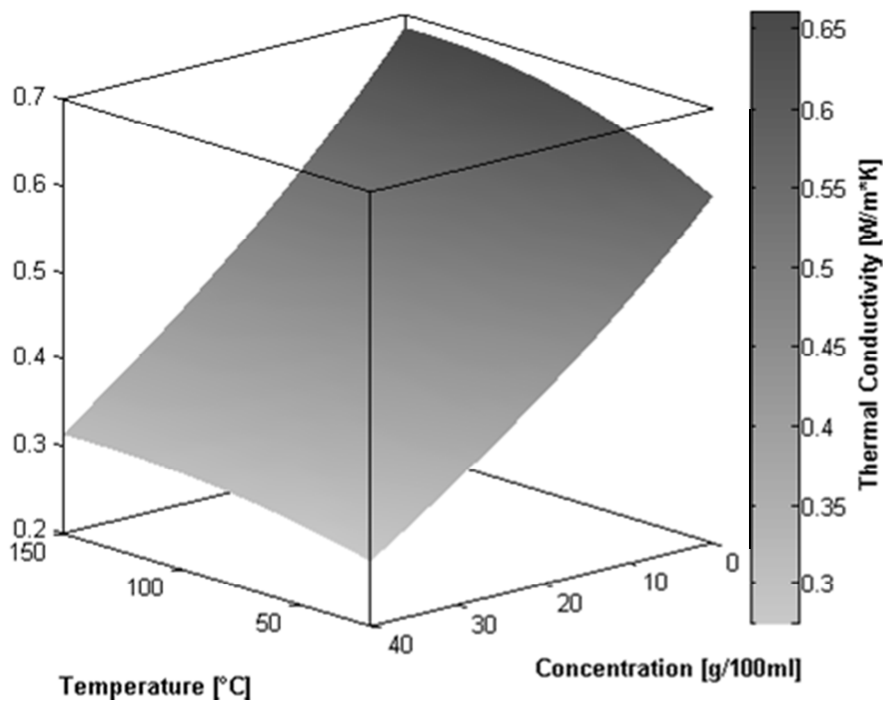


Figure 5.5: Electrolyte thermal conductivity model

5.1.6 Heat capacity

Heat capacity represents the energy required to raise the temperature of a substance by a given amount, often given the SI units $\text{J/kg}\cdot\text{K}$ or $\text{J/mol}\cdot\text{K}$.

5.1.6.1 Air-vapor mixture

The specific heat of the air is calculated by [54]:

$$a = 1.9327 \cdot 10^{-10}T^4 - 7.9999 \cdot 10^{-7}T^3 + 1.1407 \cdot 10^{-3}T^2 - 0.4489T + 1057.3$$

$$Cp_a = a/1000 \quad [5.34]$$

The specific heat of water vapor is calculated by:

$$Cp_{wv} = -1.09354 \cdot 10^{-12}T^4 - 6.63918 \cdot 10^{-10}T^3 + 1.10234 \cdot 10^{-6}T^2 - 4.64233 \cdot 10^{-4}T + 1.89559 \quad [5.35]$$

To determine the heat capacity of the air-water vapor mixture, the heat capacity of each component is averaged:

$$Cp_g = Cp_{wv}x_{wv} + Cp_ax_a \quad [5.36]$$

5.1.6.2 Electrolyte

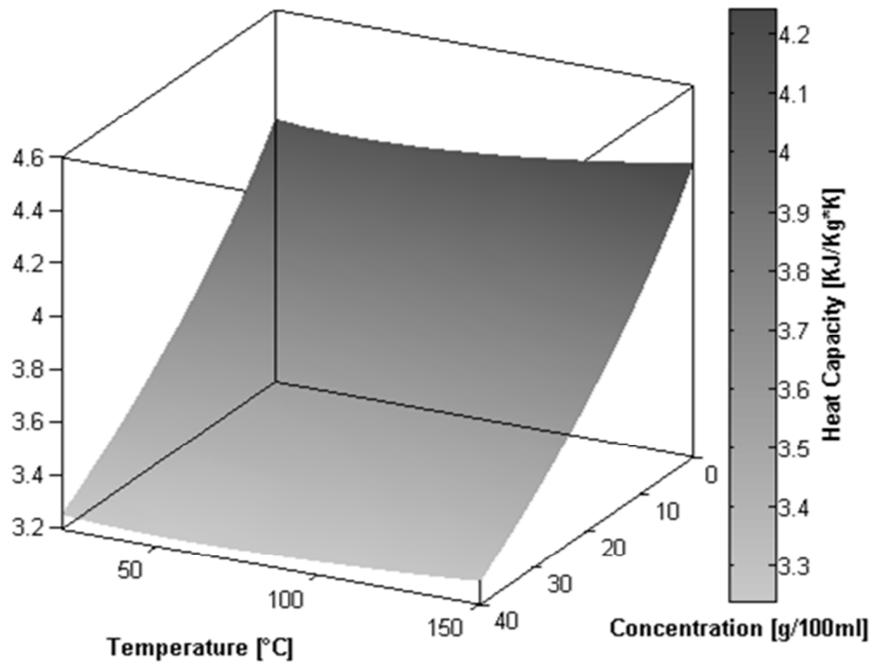


Figure 5.6: Electrolyte heat capacity model

The values for the electrolyte heat capacity model are shown in Figure 19. The electrolyte solution heat capacity is calculated using Equation 5.37 [50]:

$$Cp_{sol} = Cp_w x_w + \sum_i Cp_i x_i \quad [5.37]$$

where Cp_w is the heat capacity of water in kJ/kg·K, Cp_{sol} is the heat capacity of the solution, x_w and x_i are the mass fractions of water and solute, respectively, and Cp_i is the heat capacity of the solute. The heat capacity of water, in J/kmol·K, is given by Equation 5.38, valid for [273.15 K < T < 533.15 K], from Perry's chemical engineer's handbook [48]:

$$Cp_w = c_1 + c_2 T + c_3 T^2 + c_4 T^3 + c_5 T^4 \quad [5.38]$$

To determine the heat capacity of the solute, Equations 5.39 and 5.40 are given by Laliberte [50]:

$$Cp_i = c_1 e^\alpha + c_5 (1 - x_w)^{c_6} \quad [5.39]$$

$$\alpha = c_2 + c_3 e^{0.01T} + c_4 (1 - x_w) \quad [5.40]$$

where Cp_i is the heat capacity in kJ/kg·K. Coefficients for heat capacity are shown in Table 10.

Coefficient	Water	Electrolyte
c_1	276370	-7.629893672
c_2	-2090.1	0.004002253
c_3	8.125	-1.486444632
c_4	-0.014116	-1.809311448
c_5	9.3701E - 06	1.305076189
c_6		0.274748304

Table 5.7: Coefficients for heat capacity correlations

5.1.7 Partial pressure

The partial pressure of a gas is the pressure it would exert in a specified volume, if it would occupy the volume. For water vapor, this value is commonly called to as the vapor pressure. The vapor pressure of Copper II Chloride dihydrate is the pressure that water exhibits when sTable, but not saturated, crystals of Copper II Chloride (with their 27% water content) are found in the control volume. Since dcc is a very good desiccant, it should be expected that the vapor pressure of dcc is much lower of pure water, as shown in Figure 20.

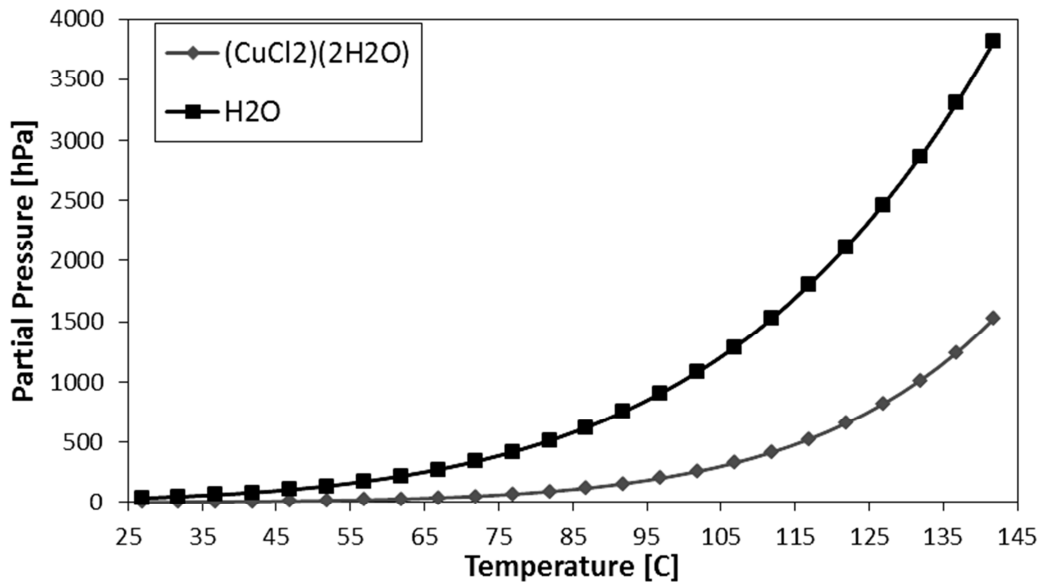


Figure 5.7: Partial pressure vs. temperature of water and dcc [40] [48]

Noel [57] used the following Equation for the vapor pressure at saturated conditions:

$$\ln p_{sat} = c_1 - \frac{c_2}{T+c_3} \quad [5.41]$$

where p_{sat} is in Torr and T is in °C. Polyachenok [40] proposed the following Equation for the partial pressure of water over Copper II Chlorine dihydrate:

$$\ln \frac{p}{p_0} = c_1 - c_2/T - c_3 \ln T \quad [5.42]$$

where p_0 is the standard pressure (1013.25 hPa), and T is in K. The various coefficients used for these Equations are shown in Table 11 below.

Coefficient	Water	Electrolyte
c_1	7.94917	25.515
c_2	1657.462	7409.4
c_3	227.02	1.203

Table 5.8: Coefficients for partial pressure correlations

5.1.8 Wet bulb temperature

The wet-bulb temperature is defined as the temperature air reaches when it becomes saturated with a pool of cool water. This can be defined either using thermodynamics as a stream of air cooled using water. At the point when the air stream is saturated with water vapor, it reaches the wet bulb temperature:

$$(x_{sat} - x_0)\lambda = (T_0 - T_{sat})Cp_g \quad [5.43]$$

where H_{sat} is the saturated water content of the air, H_0 is the initial content of water in air on a dry mass basis, T_0 and T_{sat} are the initial and saturated temperatures of the air, respectively, Cp_g is the heat capacity of air, and λ is a constant. The Equation is often approximated with a hydrometer where, at the bottom of a thermometer, a droplet of water is evaporated by air passing over it. At equilibrium, the heat gained through convection is equal to the heat removed by evaporation:

$$(x_{sat} - x_0)\lambda \cdot h_m = (T_0 - T_{wb})h_c \quad [5.44]$$

where h_c is the heat transfer coefficient, and h_m is the mass transfer coefficient. Equations 5.43 and 5.44 are equal if $\frac{h_c}{c_{p_g} \cdot h_m} = 1$. To determine T_{wb} thermodynamic Equations can be used. To the following Equation is used to correlate the wet bulb temperature with the dry bulb temperature and the relative humidity [58]:

$$T_{wb} = 237 \log(p_{sat} \cdot RH/611) / (7.5 - \log(p_{sat} \cdot RH/611)) \quad [5.45]$$

where RH is the relative humidity. Equation 5.45 is used to solve for the wet bulb temperature directly without the use of a psychometric chart.

5.1.1 Latent heat of vaporization

The heat of vaporization is the heat required to bring a defined amount of a substance from its boiling point in liquid form to a saturated vapor, otherwise known as boiling. This process is shown under the vapor dome in Figure 21.

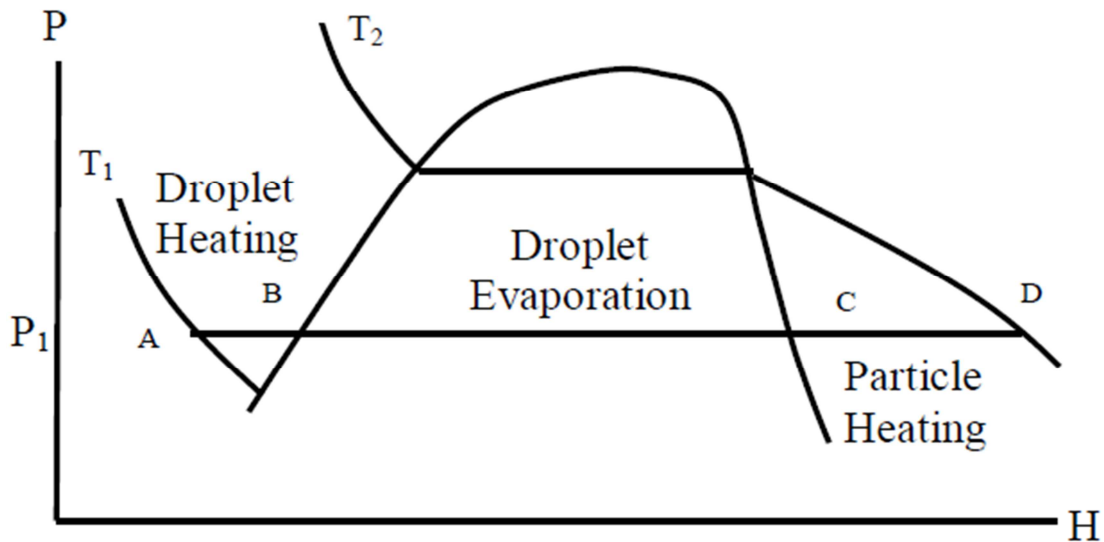


Figure 5.8: Phase diagram of drying process [59]

The energy required to vaporize the same amount of liquid is greater at lower temperatures and pressures. Since the pressure differences in spray drying during the drying itself are minor, the Watson correlation was used to model the temperature dependence of the latent heat of vaporization at atmospheric pressure [60]:

$$\frac{\Delta H_{v1}}{\Delta H_{v2}} = \left(\frac{1-T_1/T_c}{1-T_2/T_c} \right)^{0.38} \quad [5.36]$$

Where the ΔH_v is the latent heat of vaporization, the subscripts 1 and 2 refer to reference temperature and desired temperature, and the subscript c is for critical temperature, 647.1K. The reference state was taken at 373.15K, where the latent heat of water is $\Delta H_v = 2257$ kJ/kg [61].

Chapter 6

Theory

6.1 Fluid spraying

In the first stage of spray drying, the fluid exiting the nozzle is atomized. A two fluid nozzle will be studied.

6.1.1 Fluid mechanics

The following momentum Equation in vector notation governs the fluid jet exiting the nozzle:

$$\frac{D\vec{u}_i}{Dt} = -\frac{\nabla p}{\rho} + \frac{\nabla \cdot \tau}{\rho} + g + \frac{F}{\rho} \quad [6.1]$$

where the individual variables are defined in the nomenclature. The shear stress relation below is used.

$$\tau_i = -\mu \left(\nabla \vec{u}_i + \nabla \vec{u}_i^T - \frac{2}{3} \nabla \cdot \vec{u}_i \right) \quad [6.2]$$

For an incompressible Newtonian fluid with uniform viscosity, $\nabla \vec{u}_i^T - \frac{2}{3} \nabla \cdot \vec{u}_i = 0$, and the shear stress constitutive Equations are denoted as follows:

$$\tau_{rz} = \tau_{zr} = -\mu \left(\frac{\partial u_z}{\partial r} + \frac{\partial u_r}{\partial z} \right) \quad [6.3]$$

$$\tau_{zz} = -\mu \frac{\partial u_z}{\partial z} \quad [6.4]$$

$$\tau_{\theta z} = \tau_{z\theta} = -\mu \left(\frac{\partial u_\theta}{\partial z} + \frac{1}{r} \frac{\partial u_z}{\partial \theta} \right) \quad [6.5]$$

For the initial liquid jet, the most important term is the axial momentum (z-direction).

Expanding Equation 6.2 for the z-direction:

$$\frac{\partial u_z}{\partial t} + u_r \frac{\partial u_z}{\partial r} + \frac{u_\theta}{r} \frac{\partial u_z}{\partial \theta} + u_z \frac{\partial u_z}{\partial z} = -\frac{1}{\rho_i} \frac{\partial p_i}{\partial z} - \frac{1}{\rho_i} \left(\frac{1}{r} \frac{\partial}{\partial r} (r \tau_{rz}) + \frac{1}{r} \frac{\partial \tau_{\theta z}}{\partial \theta} + \frac{\partial \tau_{zz}}{\partial z} \right) + g_z + \frac{F_z}{\rho_i} \quad [6.6]$$

Assuming a negligible rotational velocity ($u_\theta = 0, \frac{\partial u_z}{\partial \theta} = 0, \frac{\partial u_\theta}{\partial \theta} = 0$), negligible effects of gravity in the micro scale, steady state and substituting in the Newtonian shear stress relations:

$$u_r \frac{\partial u_z}{\partial r} + u_z \frac{\partial u_z}{\partial z} = -\frac{1}{\rho_i} \frac{\partial p_z}{\partial z} - \frac{\mu}{\rho_i} \left(\frac{1}{r} \frac{\partial u_z}{\partial r} + \frac{\partial^2 u_z}{\partial r^2} + \frac{\partial^2 u_z}{\partial z^2} \right) + \frac{F_z}{\rho_i} \quad [6.7]$$

For a free jet, the internal pressure is caused by surface tension:

$$p_z = \sigma \left(\frac{1}{\mathcal{R}_N} + \frac{1}{\mathcal{R}_T} \right) \quad [6.8]$$

where \mathcal{R}_N and \mathcal{R}_T are the radii of curvature in the normal and tangential directions, respectively. They can be defined as:

$$\mathcal{R}_N = \left(1 + \left(\frac{\partial r}{\partial z} \right)^2 \right)^{1/2} \quad [6.9]$$

$$\mathcal{R}_T = \frac{\left(1 + \left(\frac{\partial r}{\partial z} \right)^2 \right)^{3/2}}{-\frac{\partial^2 r}{\partial z^2}} \quad [6.10]$$

For small oscillations of the radius with respect to the z axis, ($\left(\frac{\partial r}{\partial z}\right)^2 = 0$), $\mathcal{R}_N = r$, and

$\mathcal{R}_T = -\frac{\partial^2 r}{\partial z^2}$, and the pressure gradient can be denoted as:

$$\frac{\partial P_z}{\partial z} = \sigma \left(\frac{1}{r^2} \frac{\partial r}{\partial z} - \frac{\partial^3 r}{\partial z^3} \right) \quad [6.11]$$

Re-writing the momentum Equation with the pressure term, and assuming no large external forces while the liquid jet is breaking up, the following governing momentum Equation is obtained:

$$u_r \frac{\partial u_z}{\partial r} + u_z \frac{\partial u_z}{\partial z} = -\frac{\sigma}{\rho_i} \left(\frac{1}{r^2} \frac{\partial r}{\partial z} - \frac{\partial^3 r}{\partial z^3} \right) - \frac{\mu}{\rho_i} \left(\frac{1}{r} \frac{\partial u_z}{\partial r} + \frac{\partial^2 u_z}{\partial r^2} + \frac{\partial^2 u_z}{\partial z^2} \right) \quad [6.12]$$

To determine the final particle size, a scaling analysis is used. This will determine which non-dimensional groups are most evident during initial droplet breakup. The following scaling variables are used:

$$z^* = \frac{z}{r_0} \quad [6.13]$$

$$r^* = \frac{r}{r_0} \quad [6.14]$$

$$u_r^* = \frac{u_r}{u_{r,0}} \quad [6.15]$$

$$u_z^* = \frac{u_z}{u_{z,0}} \quad [6.16]$$

where r_0 is used for the axial length scale because the length of the jet is not known. Using the following relation: $u_{z,0} = u_{r,0} \cdot A$ where A is a constant, the relations are substituted into the momentum Equation and simplified:

$$A \cdot u_r^* \frac{\partial u_z^*}{\partial r^*} + u_z^* \frac{\partial u_z^*}{\partial z^*} = - \left(\frac{\sigma}{u_{z,0}^2 \rho r_0} \right) \left(\frac{1}{r^{*2}} \frac{\partial r^*}{\partial z^*} - \frac{\partial^3 r^*}{\partial z^{*3}} \right) - \left(\frac{\mu}{\rho u_{z,0} r_0} \right) \left(\frac{1}{r^*} \frac{\partial u_z^*}{\partial r^*} + \frac{\partial^2 u_z^*}{\partial r^{*2}} + \frac{\partial^2 u_z^*}{\partial z^{*2}} \right) \quad [6.17]$$

From Equation 6.17, two non-dimensional groups are formed – the Weber and Reynolds numbers. They are defined as follows:

$$We = \frac{\sigma}{u_{z,0}^2 \rho r_0} \quad [6.18]$$

$$Re = \frac{\mu}{\rho u_{z,0} r_0} \quad [6.19]$$

Substituting these relations into Equation 6.20:

$$A \cdot u_r^* \frac{\partial u_z^*}{\partial r^*} + u_z^* \frac{\partial u_z^*}{\partial z^*} = - \frac{1}{We} \left(\frac{1}{r^{*2}} \frac{\partial r^*}{\partial z^*} - \frac{\partial^3 r^*}{\partial z^{*3}} \right) - \frac{1}{Re} \left(\frac{1}{r^*} \frac{\partial u_z^*}{\partial r^*} + \frac{\partial^2 u_z^*}{\partial r^{*2}} + \frac{\partial^2 u_z^*}{\partial z^{*2}} \right) \quad [6.20]$$

From Equation 6.20, two non-dimensional groups are formed. These groups determine the relative scale of each of the terms. The Reynolds number determines the ratio of shear forces to momentum forces, while the Weber number relates surface tension forces to momentum forces. A correlation describing the initial jet atomization phenomenon and droplet size from initial parameters has the form:

$$\frac{d_{32}}{d_0} = C \cdot We^\alpha \cdot Re^\beta \quad [6.21]$$

Often in sprays, the Ohnesorge number is introduced, which is a ratio of the Weber and Reynolds numbers:

$$Oh = \frac{\mu}{\sqrt{\rho\sigma L}} = \frac{\sqrt{We}}{Re} \quad [6.22]$$

Since all three numbers (We, Oh, and Re) are not independent of each other, a droplet size correlation should include only two out of three numbers. To be consistent with previous droplet size correlations as shown in Chapter 3, Equation 6.22 is adapted to use the Ohnesorge number. It has the following form:

$$\frac{d_{32}}{d_0} = C \cdot We^\alpha \cdot Oh^\beta \quad [6.23]$$

Equation 6.23 is a useful estimate of initial droplet size. However, since only one fluid Equation is used, the relative differences between the gas for atomization and the liquid are not considered.

6.1.2 Jet breakup length

To determine the length required for the liquid jet to be atomized, a semi-empirical dimensional analysis is used. This analysis is commonly called to as the Buckingham-Pi theorem. The following physical quantities in Table 12 are considered to have significant effects on the jet breakup length:

Property	Symbol	Units	Fundamental Units
Absolute fluid viscosity	μ	kg/(m · sec)	M/(L · T)
Jet breakup length	z_0	m	L
Jet diameter	d_0	m	L
Initial jet velocity	v_0	m/sec	L/T
Fluid density	ρ	kg/m ³	M/L ³
Surface tension	σ	kg/sec ²	M/T ²

Table 6.1: Jet breakup length dimensional analysis variables

To use the Buckingham-pi theorem, two rules must be followed. The dimensional formula of each measured quantity is expressed in the fundamental quantities upon which it depends (i.e. mass, length, time, temperature, etc.). This is shown in Table 5. Any Equation expressing the relationship of n measurable physical quantities of the form $f(\alpha, \beta, \gamma, \dots) = 0$ has a solution of the form $\pi(\pi_1, \pi_2, \pi_3, \dots) = 0$. The number of π variables is equal to $n - r$ where r is the number of fundamental dimensions used to measure the quantities. Here, $n = 6$ and $r = 3$ so there are three π groups required to accurately describe the jet breakup length.

$$f(\mu, z_0, d_0, v_0, \rho, \sigma) = 0 \quad [6.24]$$

$$\pi(\pi_1, \pi_2, \pi_3) = 0 \quad [6.25]$$

Each π group is a dimensionless number and a combination of the measured quantities:

$$\pi = \mu^a z_0^b d_0^c v_0^d \rho^e \sigma^f \quad [6.26]$$

To ensure that each π group is a dimensionless number, the fundamental dimensions are introduced into Equation 5.26:

$$\pi = \left(\frac{M}{LT}\right)^a (L)^b (L)^c \left(\frac{L}{T}\right)^d \left(\frac{M}{L^3}\right)^e \left(\frac{M}{T^2}\right)^f \quad [6.27]$$

From 5.27, there are three separate Equations for the exponents of the fundamental dimensions. Each of the exponents on the fundamental Equations must be equal to zero:

$$a + e + f = 0$$

$$-a + b + c + d - 3e = 0 \quad [6.28]$$

$$a + d + 2f = 0$$

For the first π group we choose $b = 1$ as z_0 as the variable we are looking to find. Since c has the same dimensions, choose $b = 1$ and $c = -1$. By choosing these two variables, a simple non-dimensional solution will give no other measured physical quantities. This gives the somewhat trivial result:

$$\pi_1 = \mu^0 z_0^1 d_0^{-1} v_0^0 \rho^0 \sigma^0 = \frac{z_0}{d_0} \quad [6.29]$$

For the second group, look at the surface tension: take $f = 1$ to allow for the surface tension term. Since jet length is not a commonly used term in non-dimensional variables, allow for $b = 0$. From the previous non-dimensionalization of the momentum Equation, it was evident that the viscosity term and surface tension term appeared in different non-dimensional groups. Therefore, for the viscosity term, $a = 0$. This yields the Weber number:

$$\pi_2 = \mu^0 z_0^1 d_0^{-1} v_0^{-2} \rho^{-1} \sigma^1 = \frac{\sigma}{d_0 v_0^2 \rho} \quad [6.30]$$

For the third group, choose $a = 1$, corresponding to the viscosity term, which has not appeared yet. As a corollary to the second group, take $f = 0$ and $b = 0$, yielding the Reynolds number:

$$\pi_2 = \mu^0 z_0^1 d_0^{-1} v_0^{-2} \rho^{-1} \sigma^1 = \frac{\mu}{\rho v_0 d_0} \quad [6.31]$$

This yields the result:

$$\frac{z_0}{d_0} = A \cdot Re^a We^b \quad [6.32]$$

This is similar to the result from the previous Section. Note that Weber [62] determined that for low velocity jets, the following Equation can be used to determine breakup length, which includes all the same non-dimensional groups:

$$\frac{z_0}{d_0} = \sqrt{We} \cdot \ln\left(\frac{d_0}{2\alpha_0}\right) \cdot \left(1 + \frac{3\sqrt{We}}{Re}\right) \quad [6.33]$$

The value α_0 is obtained from perturbation theory of jets. Knowing the initial velocity, it is straight forward to estimate the jet breakup time. For higher jet velocities governed by aerodynamic breakup, Yarin [63] determined the breakup length:

$$\frac{z_0}{d_0} = \sqrt{We} \cdot \ln\left(\frac{m \cdot d_0}{2\alpha_0}\right) \cdot \left(\frac{3\mu\rho d_0^2 v_0^3}{(\rho v_0^2 - \sigma/d_0)^2}\right)^{1/3} \quad [6.34]$$

where m is a constant between 2-4 that is fitted to experimental data.

6.2 Heat and mass transfer

When a droplet is formed, drying and evaporation continue in stages. First, the droplet is heated up to the wet bulb temperature of the surrounding gas. The evaporation and boiling commence. As more volatiles are evaporated from the droplet, saturation conditions begin to exist on the droplet surface. Local nucleation of salt crystals begins, and a crust is formed as these crystals grow toward each other. As the crust is formed, water is brought to the surface through pores which are formed in the crust. This is the onset of the falling rate drying period. After all water leaves the droplet-now-turned-particle, the particle is heated to the equilibrium temperature with its surroundings.

6.2.1 Initial droplet heating

The initial heating starts when the fluid exits the nozzle flow. The initial heating occurs on the order of tenths of a second [64]. For a spherical droplet with isotropic properties, the following energy conservation Equation is used to describe the initial stages of droplet heating in spherical coordinates [59]:

$$\rho_i C_p \frac{DT_d}{Dt} = k_d \nabla^2 T_d + \mu_d \left(\frac{\partial u}{\partial r} \right)^2 \quad [6.36]$$

The Laplacian of T_d in spherical coordinates, or the conduction term, is defined as:

$$\nabla^2 T_d = \frac{1}{r^2} \frac{\partial}{\partial r} \left(r^2 \frac{\partial T_d}{\partial r} \right) + \frac{1}{r^2 \sin(\theta)} \frac{\partial}{\partial \theta} \left(\sin(\theta) \frac{\partial T_d}{\partial \theta} \right) + \frac{1}{r^2 \sin^2(\theta)} \frac{\partial^2 T_d}{\partial \varphi^2} \quad [6.37]$$

The material derivative of T_d in spherical coordinates, is defined as:

$$\frac{DT_d}{Dt} = \frac{\partial T_d}{\partial t} + u_r \frac{\partial T_d}{\partial r} + \frac{u_\theta}{r} \frac{\partial T_d}{\partial \theta} + \frac{u_\varphi}{r \sin(\theta)} \frac{\partial T_d}{\partial \varphi} \quad [6.38]$$

As previously noted in past studies [64] [59] [65] [66], a lumped capacitance heat and mass transfer model is assumed if the temperature distribution within the droplet is sufficiently small. The lumped capacitance model implies that heat conduction within the droplet is much faster than heat convection away from the droplet surface. It models the whole heat transfer process from the droplet to its surroundings in one lumped process. To use the lumped capacitance model, the Biot number must be below 0.1:

$$Bi = \frac{hLc}{k_{sol}} < 0.1 \quad [6.39]$$

where L_C is the ratio of the volume to the surface area:

$$L_C = \frac{4/3\pi(D_d/2)^3}{4\pi(D_d/2)^2} = \frac{D_d}{3} \quad [6.40]$$

Also h , the heat transfer coefficient is obtained from the Nusselt number:

$$Nu = \frac{2hD_d}{k_{sol}} \quad [6.41]$$

The initial heating of the droplet happens on the order of tenths of a second, so the Fourier number, $Fo = \alpha_d t / r_d^2 > 0.1$ and temperature dependence with time must be considered. Due to the small droplet diameters, it is assumed that internal convection within the droplet is negligible. Equation 5.32 can be written as:

$$\frac{\partial T_d}{\partial t} = + \frac{\alpha}{r^2} \frac{\partial}{\partial r} \left(r^2 \frac{\partial T_d}{\partial r} \right) \quad [6.42]$$

with the following boundary conditions:

$$\begin{cases} \frac{\partial T_b}{\partial r} = 0, & r = 0; \\ h(T_s - T_b) = k_{sol} \frac{\partial T_b}{\partial r}, & r = R_d. \end{cases} \quad [6.43]$$

In the centre of the droplet, there is only a time dependence on temperature. At the outside of the droplet, the temperature is influenced by the outside gas temperature and the thermal conductivity of the droplet, k_{sol} . In Figure 11, this step happens after the initial droplet and before the surface drying. For surface drying to start, the droplet temperature is brought above the wet bulb temperature for the current air moisture content.

6.2.2 Evaporation and shrinkage

After the initial heating process, the droplet continues to dry in a constant drying period. Evaporation and shrinkage occur from the droplet surface. The analysis in the following Section uses simplified forms of the transport Equations, with the following assumptions, similar to the assumptions of the d^2 law combustion model [67]:

1. The drying droplet is spherically symmetrical.
2. Buoyancy effects are neglected ($Gr \ll 0$).
3. The droplet is a single isolated droplet in an infinite drying medium.
4. The gas phase transport properties are constant in time.
5. The gas phase is quasi-steady.
6. The Lewis number for the gas is close to unity.
7. The droplet has a constant uniform temperature.
8. Negligible radiation, Dufour and Soret effects.

Often in evaporation analysis, the equivalence of heat and mass transfer is used [59] [68].

This is justified by stating the Lewis number is on the order of unity:

$$Le = \frac{Sc}{Pr} = \frac{\alpha}{D} \approx 1 \quad [6.44]$$

where α is the thermal diffusivity and D is the mass diffusivity. For droplets, the Nusselt number for heat transfer and the Sherwood number for mass transfer are compared. The Ranz-Marshall correlations are cited [69]:

$$Nu = 2 + Re^{1/2} Pr^{1/3} \quad [6.45]$$

$$Sh = 2 + Re^{1/2} Sc^{1/3} \quad [6.46]$$

Equation 6.45 has a form found by Hoffman and Ross [70] in their computational solutions for the energy Equation *in the absence of evaporation* (only diffusion mass transfer was considered), during initial droplet heating. A different solution was proposed (also for initial droplet heating) for $1 < Re \leq 400$ [71]:

$$Nu = 1 + (1 + RePr)^{1/3} Re^{0.077} \quad [6.47]$$

This Equation fit experimental data for non-evaporating drops by $\pm 3\%$. To determine the effects of evaporation, two hydrodynamic approaches are considered.

6.2.2.1 Mass transfer analysis

At the surface of an evaporating droplet moving in a surrounding fluid, the following Equation describes the mass diffusion and convective mass flow (Stefan flow) [72]:

$$\frac{\dot{m}_d}{4\pi R^2} = \mathfrak{D}_v \frac{d\rho_v}{dR} - \mathfrak{D}_g \frac{\rho_v}{\rho_g} \frac{d\rho_g}{dR} \quad [6.48]$$

The left hand term is the mass flux from the droplet, the middle term shows the diffusion effects and the third term represents the effects of Stefan flow. Assuming that the vapor diffusion coefficient is the same as the total gas diffusion: $\mathfrak{D}_g = \mathfrak{D}_v$, and that the total density of the gas is constant: $\rho_v + \rho_g = \rho_{total} = const$, and integrating from $R = R_{d \rightarrow \infty}$:

$$\dot{m}_d = 4\pi R^2 \mathfrak{D}_v \rho_{total} \ln(1 + B_M) \quad [6.49]$$

where B_M is the mass transfer Spalding number:

$$B_M = \frac{\rho_{vs} - \rho_{vb}}{\rho_{vs}} \quad [6.50]$$

The Spalding number is named after Prof. Brian Spalding who pioneered computational fluid dynamics and the science of combustion from the 1950s to the 1970s.

Following the definition of the Sherwood number:

$$Sh = \frac{2R_d h_m}{\mathcal{D}_g} \quad [6.51]$$

The heat transfer coefficient, h_m is defined whereby:

$$\dot{m}_d = 4\pi R_d^2 h_m (\rho_{vs} - \rho_{vb}) \quad [6.52]$$

Equation 6.47 can be re-written:

$$\dot{m}_d = 2\pi R_d \mathcal{D}_g \rho_{total} Sh^* B_M \quad [6.53]$$

The Sherwood number here is:

$$Sh^* = \frac{\ln(1+B_M)}{B_M} Sh_0 \quad [6.54]$$

where Sh_0 is the Sherwood number in the absence of evaporation, defined by Equation 6.45, replacing Pr with Sc.

6.2.2.2 Heat transfer analysis

Performing an energy balance at the surface of the droplet, the following Equation is obtained:

$$4\pi R_d^2 k_g \frac{dT}{dR} = -\dot{m}_d c_{pv} (T - T_s) - \dot{m}_d \Delta H_v(T_s) + |\dot{q}_d| \quad [6.55]$$

where the left side is the heat supplied from the surroundings, the first right term is the heat required to initially heat the droplet, the second term describes the vaporization, and the

final term is the heating of the droplet's vapor to ambient conditions. Integrating Equation 6.55 from $R = R_{d \rightarrow \infty}$ and $T = T_{s \rightarrow g}$:

$$\dot{m}_d = -\frac{4\pi R_d k_g}{c_{pv}} \ln(1 + B_T) \quad [6.56]$$

Following the definition of the Nusselt number from Equation 6.41, and Equation 6.52 for the heat transfer coefficient, Equation 6.56 can be rewritten as:

$$\dot{m}_d = 2\pi R_d \frac{k_g}{c_{pv}} Nu^* B_T \quad [6.57]$$

The Nusselt number here is:

$$Nu^* = \frac{\ln(1+B_T)}{B_T} Nu_0 \quad [6.58]$$

where B_T is the heat transfer Spalding number:

$$B_T = \frac{c_{pv}(T-T_s)}{\Delta H_v(T_s) - |\dot{q}_d|/\dot{m}_d} \quad [6.59]$$

Also Nu_0 is the Nusselt number in the absence of evaporation, defined by Equation 6.45. Equations 6.53 and 6.57 have very similar forms. They differ by their definitions of the Spalding number:

$$B_T = (1 + B_M)^\alpha - 1 \quad [6.61]$$

$$\alpha = \frac{c_{pv}}{c_{pg}} \frac{1}{Le} \quad [6.61]$$

1.1.1 Velocity estimation

The following Equation was used as an initial velocity of the liquid droplets [30]:

$$v_g \cdot \dot{m}_g = v_{mr} \cdot \dot{m}_g + v_{mr} \cdot \dot{m}_{sol} \quad [6.62]$$

$$V_{mr} = \frac{V_{air}}{1 + \frac{\dot{m}_{liq}}{\dot{m}_{air}}} = \frac{\dot{V}_{air}/A_{orifice}}{1 + \frac{\dot{V}_{liq}\rho_{liq}}{\dot{V}_{at.air}\frac{P_{at.air}}{RT_b}}} \quad [6.63]$$

This velocity is based on momentum conservation.

6.2.3 Correlation development

In the following chapter, materials and methods, the experimental setup is discussed.

Experiments are

6.3 Particle size distributions

As noted in Chapter 3, a distribution analysis is used as a tool to describe physical changes between experiments. The particle size Equations are deterministic to describe the range of data, and the type of data observed. All particle distribution functions were fitted to all data, to determine the type of distribution that the experiments follow, and the spread of the distributions.

6.3.1 Characteristics of particle distribution functions

All particle distribution functions used follow certain characteristics. The total number of drops below a minimum diameter and above a maximum diameter should be very small:

$$\lim_{d \rightarrow 0} \int_0^d f(d) dd = 0 \quad [6.64]$$

$$\lim_{d \rightarrow \infty} \int_d^{\infty} f(d) dd = 0 \quad [6.65]$$

The distributions are positive and normalized:

$$f(d) \geq 0 \quad [6.66]$$

$$\int_0^{\infty} f(d) dd = 1 \quad [6.67]$$

With these characteristics, a few distribution models are chosen to be fitted to the measured size distributions. All distributions were chosen as they were previously applied to spray drying, as noted by Babinsky and Sojka [33].

6.3.2 Log-normal distribution

The first and simplest distribution to be fitted is the Log normal distribution:

$$f_1(d) = \frac{1}{d(\ln\sigma)\sqrt{2\pi}} \exp\left\{-\frac{1}{2} \left[\frac{\ln(d/\bar{d})}{\ln\sigma}\right]^2\right\} \quad [6.68]$$

where d is the predicted particle size, σ is a parameter describing the shape of the distribution ($\sigma > 0$), and \bar{d} is a representative diameter for curve fitting.

6.3.3 Maximum-ended log-normal distribution

As the Log-normal distribution has a trailing end with a probability of obtaining infinitely large particles becoming infinitely small, an upper limit can be introduced on the

probability. Above this upper limit, the probability of obtaining particles is zero. The probability distribution function is defined as follows:

$$f_2(d) = \frac{\delta d_{\max}}{\sqrt{\pi}d(d_{\max}-d)} \exp\left\{-\delta^2 \left[\ln\left(\frac{ad}{d_{\max}-d}\right)\right]^2\right\} \quad [6.69]$$

The the following properties are defined:

$$a = \frac{d_{\max}}{\bar{d}} \quad [6.70]$$

$$\delta = \frac{1}{\sqrt{2}(\ln\sigma)} \quad [6.71]$$

where σ is the width of the distribution ($\sigma > 0$), \bar{d} is the logarithmic mean size of the distribution, and d_{\max} is the maximum permissible droplet diameter.

6.3.4 Root normal distribution

The root normal distribution, originally defined by Marshall and Tate [73], was applied to volume distributions in sprays. The probability distribution function is given as follows:

$$f_3(d) = \frac{1}{2\sigma\sqrt{2\pi}\bar{d}} \exp\left\{-\frac{1}{2}\left[\frac{\sqrt{\bar{d}}-\sqrt{d}}{\sigma}\right]^2\right\} \quad [6.72]$$

6.3.5 Rosin-Rammler distribution

The Rosin-Rammler distribution, introduced by Rosin and Rammler [74], originally found its application in coal particle distributions. The probability distribution function is defined in the following way:

$$f_4(d) = q\bar{d}^{-q}d^{q-1}\exp\{-(d/\bar{d})^q\} \quad [6.73]$$

where q is a value representing the width of the distribution, with large values of q giving narrow sprays. However, for physically meaningful spray distributions, $q < 3$, as larger values of q will yield negative values for distributions.

6.3.6 Test for best fit

To determine the best fit for the collected data, two different tests were performed. Initially, the Chi-squared test was used:

$$\chi^2 = \sum_{i=1}^N \frac{(m_i - p_i)^2}{p_i} \quad [6.74]$$

where χ^2 , Chi, is the value to be minimized, N is the number of values, m_i is the true measured value, and p_i is the predicted value based on the curve to be fitted. However, it was observed that the Chi-squared test gave skewed results due to small sample sizes in the analysis. Therefore, the Bayesian criterion was chosen as a tool for curve-fitting. The Bayesian information criterion is denoted as follows:

$$\sigma^2 = \frac{1}{N-1} \sum_{i=1}^N (m_i - p_i)^2 \quad [6.75]$$

The program used to determine these tests is shown in Appendix B.

6.4 Convective drying

6.4.1 Characteristic rate drying curve

Convective drying in a conventional oven was used to determine the drying rate, \mathfrak{N}_W . The drying rate is dependent on all parameters previously mentioned in this Chapter. A

model often used in expressing the drying rate uses the characteristic rate drying curve (CRDC), where the drying rate is considered to be a first order linear Equation proportional to the free moisture content [75]:

$$\mathfrak{N}_W = -\frac{1}{A_S} \frac{dm_{SW}}{d\tau} = \frac{dm_{SW}}{A_S} \frac{d\bar{X}}{d\tau} \quad [6.76]$$

where the free moisture content is defined as:

$$\bar{X} = X - X_e \quad [6.77]$$

Also X_e is the moisture content of the dry solids when they are at equilibrium with their surroundings. For dcc, above 100°C there is no chemically bound moisture and $X_e = 0$.

The moisture content, X , is $X = \frac{m_{SW} - m_S}{m_S}$ and $m_{SW} = m_W + m_S$. The wet mass, mass of moisture, and dry mass are m_{SW} , m_W , and m_S , respectively. Also A_S is the surface area in contact with the drying surface. The CDRC model is attractive for use as a convective drying model since a version modified for particles is used in spray drying. By expanding the differential terms in Equation 6.65, the following Equation is obtained:

$$\mathfrak{N}_W = (X - X_e)[C(T_b - T_{wb})] \frac{m_S X}{A_S} \quad [6.78]$$

where \mathfrak{N}_W is the drying rate (determined experimentally), T_b is the bulk temperature, which is controlled, T_{wb} is the wet bulb temperature, m_S is the mass of the solid, and A_S is the surface drying area. Also, C is a constant which is determined when equating both sides after experimentation.

Chapter 7

Materials and methods

7.1.1 Experimental design

Experiments were conducted for various drying conditions, as shown in Table 13. The hot air inlet temperature, solids concentration, hot air and liquid flow rates, atomization pressure, nozzle diameter, and liquid initial temperature were all varied. Each parameter was varied separately to determine its effect on the output parameters in isolation. The ambient air humidity and temperature were noted for each experiment using a digital barometer. For some experiments, the ambient air temperature varied significantly, and two experiments on different days were conducted to determine the effect that ambient air humidity would have on the dependent variables.

Table 7.1: Experiments performed with their respective varied parameters

Trial no.	Ambient air		Hot air			Atomization air		Atomization liquid	
	Room Temp. C	Relative Humidity %	Inlet Temp. C	Outlet Temp. C	Flow rate m ³ /min	Flow rate m ³ /hr	Pressure bar	Flow rate lit/hr	Temp. C
Effect of drying air temperature									
1	22	23	60	35	1	3	4	0.5	22
2	23	26	80	40	1	2.9	4	0.5	23
3	24	23	120	58	1	3.1	4	0.5	24
4	23.5	24	160	70	1	3.1	4	0.5	23.5
9	21.5	23	200	90	1	4.1	4	0.5	21.5
Effect of nozzle diameter									
20	22.5	23	60	25	1	5.7	2.5	0.5	22.5
19	22.5	23	121	30	1	5.75	2.5	0.5	22.5
18	22.5	23	200	30	1	5.8	2.5	0.5	22.5
30	22.5	23	200	72	1	5.2	2.5	0.5	22.5
31	22.5	23	120	60	1	5.1	2.5	0.5	22.5

Trial no.	Ambient air		Hot air			Atomization air		Atomization liquid	
	Room Temp. C	Relative Humidity %	Inlet Temp. C	Outlet Temp. C	Flow rate m ³ /min	Flow rate m ³ /hr	Pressure bar	Flow rate lit/hr	Temp. C
32	21.5	24	60	39	1	5.2	2.5	0.5	21.5
Effect of drying air flow rate									
33	21.5	23	80	40	0.8	4	4	0.5	21.5
11	22	38	120	70	0.8	4.1	4	0.5	22
5	23	25	200	82	0.8	3.25	4	0.5	23
16	21.5	23	60	35	1.2	4.55	4	0.5	21.5
12	21.5	23	120	50	1.2	4.4	4	0.5	21.5
6	21.5	23	200	100	1.2	3.79	4	0.5	21.5
34	21.5	23	61	37	1.2	3.95	4	0.5	21.5
35	21	24	120	55	1.2	3.85	4	0.5	21
Effect of atomization air pressure									
13	21.5	23	125	60	1	3.1	2	0.5	21.5
7	21.5	23	200	92	1	2.68	2	0.5	21.5
38	21.5	23	60	38	1	3	2	0.5	21.5
37	21.5	23	120	60	1	2.9	2	0.5	21.5
36	21.5	23	200	80	1	2.95	2	0.5	21.5
17	23	23	61	28	1	4.1	3	0.5	23
14	23	23	120	60	1	3.7	3	0.5	23
8	22	27	200	70	1	3.67	3	0.5	22
41	21	24	60	46	1	3.7	3	0.5	21
40	22.5	23	120	65	1	3.5	3	0.5	22.5
39	23	23	200	89	1	3.6	3	0.5	23
Effect of atomization liquid flow rate									
15	23	23	120	60	1	4	4	0.75	23
10	22	32	200	70	1	4.1	4	0.75	22
42	22	23	200	68	1	3.95	4	0.75	22
Effect of atomization liquid temperature									
28	22.5	23	120	58	1	3.35	4	0.5	40
29	22	23	200	89	1	3.95	4	0.5	40
Effect of concentration in the atomization liquid									
21	24	22	200	90	1	4.3	4	0.5	24
22	24	22	122	50	0.6	4.3	4	0.5	24
23	24	22	120	60	1	4	4	0.5	24
24	24	22	65	40	1	4.1	4	0.5	24
25	24	22	200	85	1	4.1	4	0.5	24
26	24	22	120	62	1	4.1	4	0.5	24
27	24	22	64	39	1	4.1	4	0.5	24

7.1.2 Drying apparatus

Experiments were conducted using a Yamato model D-41 spray dryer. A schematic diagram of the experimental setup for low-grade heat utilization was shown in Chapter 4, Figure 8. The dryer was modified slightly from its manufactured state to avoid irreversible corrosion caused by spray drying of corrosive cupric chloride solution. Two separate gas orifice sizes were used in the titanium nozzles: 0.7mm and 1.5 mm diameters, as shown in Figure 22.

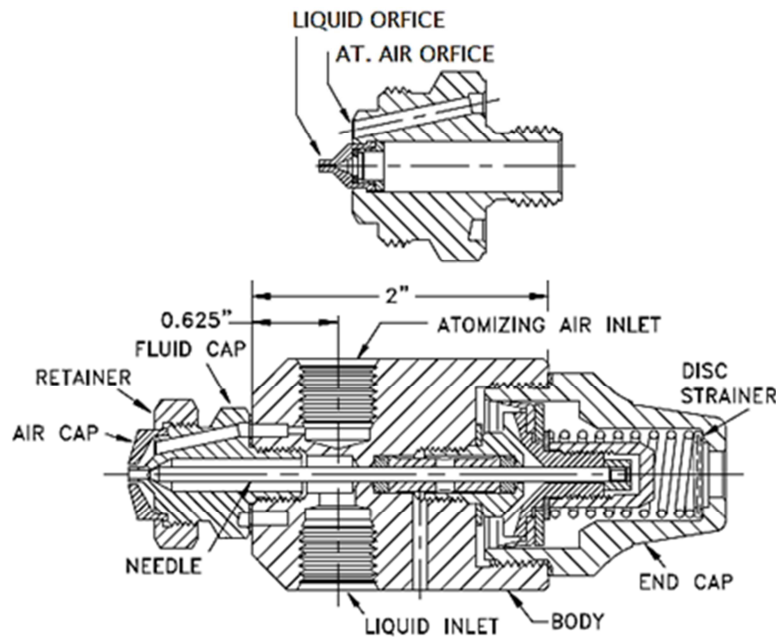


Figure 7.1: Nozzle geometry [76]

Stainless steel parts downstream of the nozzle were coated with a thin layer of Viton. All glass parts the drying chamber, the cyclone separator, and the product vessel were kept in the manufactured state. The spray drying chamber has a diameter of 0.45m, and a 1.0m cylindrical height. Also, a venturi scrubber was used to clean the flue gases of cupric chloride particles which were not captured inside the cyclone. The drying air entered the

dryer at the top and was heated. It entered the drying chamber, and left through the cyclone separator and finally the scrubber. A peristaltic pump was used to transport the atomization liquid to the two-fluid nozzle. A flow meter was installed to measure the atomized air flow rate. To measure the atomization liquid flow rate, the initial and final time of experimentation, and volume of liquid were determined. K-type thermocouples were installed to measure the exiting air humidity and temperature.

7.1.3 Materials

Analytical grade (<98% copper chloride) copper chloride and commercial grade de-ionized water were used in all experiments. All copper chloride was first dried in a conventional oven at 110°C and used in the anhydrous form during experiments, to eliminate error in hydration levels. Air was taken from the surrounding room at ambient temperature and humidity. It was filtered inside the spray dryer, and heated.

7.1.4 Product characterization

The atomization air flow rate and pressure were measure with a separate air flow meter, and a pre-installed pressure gauge, respectively. The drying air flow rate was measured with an air flow meter. The drying air inlet and outlet temperatures were measured with K-type thermocouples. The atomization liquid flow rate was varied and measured based on the time required for the experiment to complete and the volume of liquid used.

7.1.4.1 Particle size distribution

Through SEM microscopy the surface area of particles can be determined based on the observed area in the micrograph. There is a large uncertainty in underrepresenting the particle population using SEM microscopy. It is recommended that 10 000 images are processed to have an accurate representation of the population. Due to time constraints, this is often not feasible in determining the particle size. Therefore, LALLS (low angle light scattering, or laser diffraction) is used to determine the particle size, and verified with SEM microscopy. SEM microscopy is also used to determine the particle morphology.

Laser diffraction is used to determine the particle size and particle size distribution, using a Microtrac S3500 unit. The unit's particle range is 0.024-2800um. Each sample is taken a minimum of three times for repeatability. The machine is allowed to run once without any new product introduced in between samples to minimize error. The analyzer gives the particle number mean diameter, area mean diameter, volume mean diameter, and the particle size distribution. The Sauter mean diameter is taken from Table 2, and used to calculate the span. The span of the powder, which is calculated in the following way:

$$Span = \frac{(d_{90\%} - d_{10\%})}{d_{50\%}} \quad [7.1]$$

where 10%, 50%, 90% are the diameter values at the 10th, 50th, and 90th percentiles, respectively. The distribution of the data is also obtained from the Microtrac readouts. This data is used to determine the distribution model that best fits the data. The distributions were compared based on the Chi-squared test and the Bayesian information criteria, as noted in Section 6.4.5.

7.1.4.2 Particle size

Using measured properties, a procedure was used to determine the particle size. The subsequent calculated particle size was compared to the particle size and distribution obtained by laser diffraction. The following procedure was used.

1. Determine all relevant physical properties required for the particle size models. The properties were obtained from the parameters and property models:
 - a. Surface tension,
 - b. Viscosity of electrolytic fluid and gas,
 - c. Density of electrolytic fluid and gas,
 - d. Temperature, relative humidity, and saturation temperature,
 - e. Thermal conductivity and heat capacity of fluid and gas,
 - f. Nozzle geometry,
 - g. Pressure differential across nozzle to drying chamber, and
 - h. Velocity of fluid.
2. Determine non-dimensional parameters from property values
3. Use the Buckingham-Pi theorem as outlined in chapter 8 to determine the most applicable non-dimensional parameters, and use this as a guideline to compare parameters. The details of this procedure are outlined in Section 8.1.5.

The aforementioned parameters were determined experimentally in the same experiments as the particle size and distribution to validate the particle sizing models.

7.1.4.3 Particle morphology

The particle morphology was investigated using a JEOL JSM-6400 scanning electron microscope (SEM). Black carbon tape was applied to the SEM aluminum stub, and the powder sample was stuck to the carbon tape. Because the scanning electron microscope requires a vacuum, the procedure of using the SEM necessitates the complete drying of the sample before entering the SEM. The crystal structure observed under the SEM will be that of anhydrous copper (II) chloride. As noted by Engberg [77], during vacuum-drying at room temperature, the crystals behave as cubes, whereas during normal drying, they behave as long prisms. Although the crystal structure will change, the relative shape of the crystals will remain intact during vacuum drying, as compared with the changes during spray drying. However, the relative size of the crystals will change, since the density of the anhydrous form is about twice the dihydrate.

7.1.4.4 Volatile content

The moisture content of the samples was analyzed with a conventional oven. As noted by Polyachenok [40], the partial pressure of HCl in equilibrium with CuCl_2 is negligible (0.5hPa measured from a water vapor pressure of 484hPa at 400K). Therefore, it was the only volatile. A sample is prepared of 4-5g of dried copper (II) chloride powder, and the mass was recorded. The sample was kept at 105°C and was removed from the oven every hour, placed into a desiccator for 5 min, the new mass of the sample was taken, and the sample was returned to the oven. The dry mass was taken when the difference between successive measurements stabilized.

7.1.4.5 Particle flowability

The bulk density of the powder and its flowability characteristics via the Hausner ratio were measured using an Electrolab ETD-1020 tap tester, often called a Copley Tap Density Volumeter. A specified mass of powder is poured into a graduated cylinder, and the volume is measured. The cylinder is dropped using a mechanized cam rotating at 250rpm. The cylinder is first dropped 500 times, then 750 times, and the volume is measured at each interval. When the difference between consecutive measurements is less than 2%, the final volume is taken as the tapped volume.

7.2 Convective Drying

7.2.1 Experimental design

Experiments were conducted at various drying conditions, as shown in Table 14.

Temp [°C]	Sample removal frequency [min]	
150	10	5
130	10	5
105	10	
70	5	

Table 7.2: Drying rate experiments

The ambient air humidity and temperature were noted for each experiment using a digital barometer. Two experiments were conducted for selected temperatures to determine the effect of heat loss to the environment while the door was left open for approx. 1 second to remove the sample bottle.

Sample bottles were weighed for initial empty mass, mass with 4.5g \pm 0.5g of sample, and after the prescribed time of drying (allowing to cool in a desecrator for 1 minute). The

sample bottles were all returned to the dryer after experiments, to determine the bone dry mass of the dcc sample, and the initial moisture content.

One experiment at 130°C and not shown in Table 14, was also conducted. This experiment studied the drying rate of drying a dcc slurry, with initial moisture content above 27%, dry basis. Slurry is the expected outcome of a crystallization process; this experiment was more realistic as to the expected mixture composition prior to drying. The slurry was prepared using a mechanical stirrer at 600rpm for 30 min, to allow for homogeneous slurry to dry.

7.2.2 Drying apparatus

A convective dryer as shown in Section 4.2, Figure 13, was used. The temperature was controlled at different set points, while the air flow rate was kept constant. A mechanical scale with four digit accuracy was used for all mass measurements. Sample bottles were cleaned with de-ionized water and acetone between experiments. Their masses were measured before each experiment, with their lid placed beside the bottle on the scale. Samples of 4.5g were then taken, and the bottles had their lids placed on while other samples were prepared. All samples were placed inside the oven at the same time, with their lids removed. Upon removing samples from the oven, their lids were replaced, and the bottles were placed into a desiccator to allow sample bottles to cool for one minute before placing them on the scale. Figure 23 below shows a sample bottle with copper II chloride to be dried.

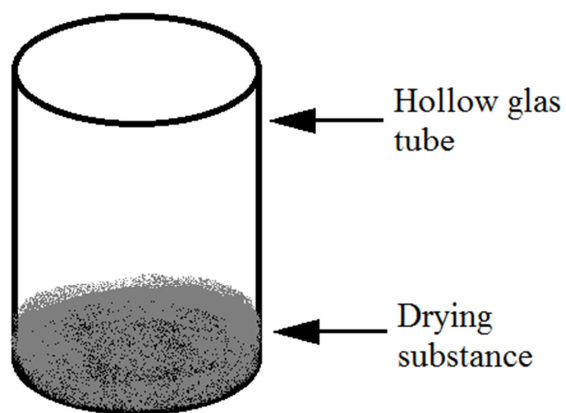


Figure 7.2: Sample bottle with copper II chloride to be dried

7.2.3 Materials

All materials were the same as in Section 7.1.3 above.

Chapter 8

Results and discussion

8.1 Spray drying

The complete data set for the experimental results is found in Appendix C. A visualization of the results is shown in Figure 24, with an interpolating surface plot to help visualize the data. In Figure 23, the effects of agglomeration have been removed, as described in Section 8.1.5.2. The temperature dependence is evident, while the pressure dependence is more nuanced.

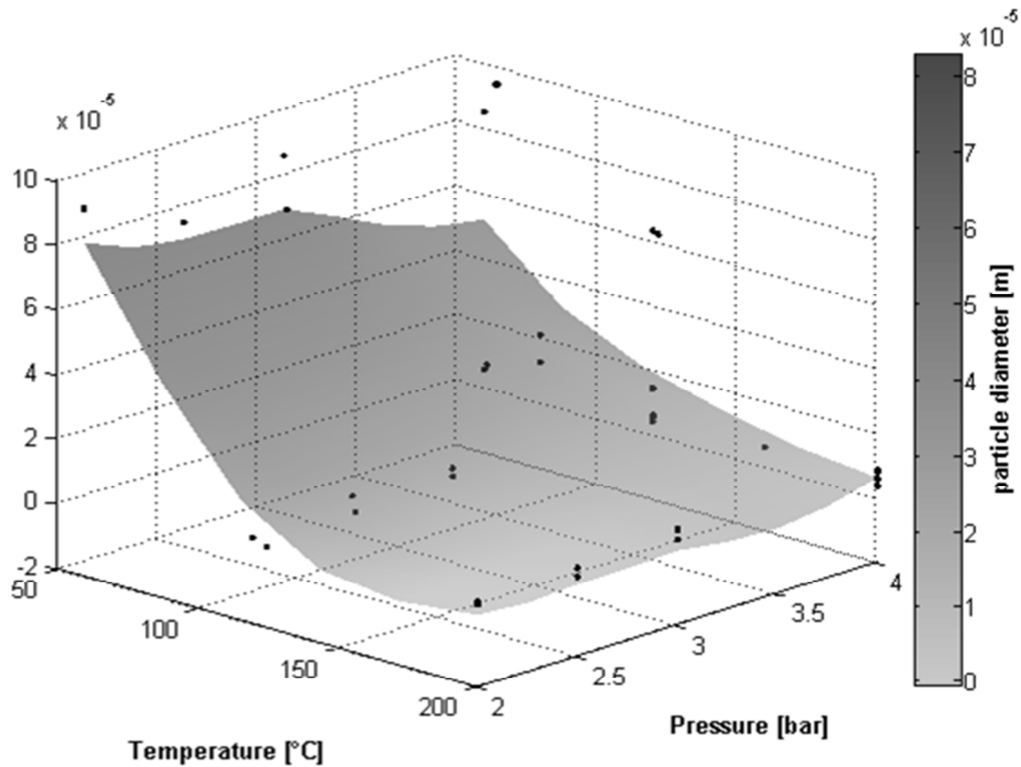


Figure 8.1: Particle diameter vs. inlet temperature and atomization pressure

Figure 25 below shows the droplet diameter dependence on the Ohnesorge and Nusselt numbers. It is clear from Figure 24 that there is a strong dependence on the Ohnesorge number, while the dependence on the Nusselt number is less pronounced. Further analysis of particle size is shown in Section 8.1.5.

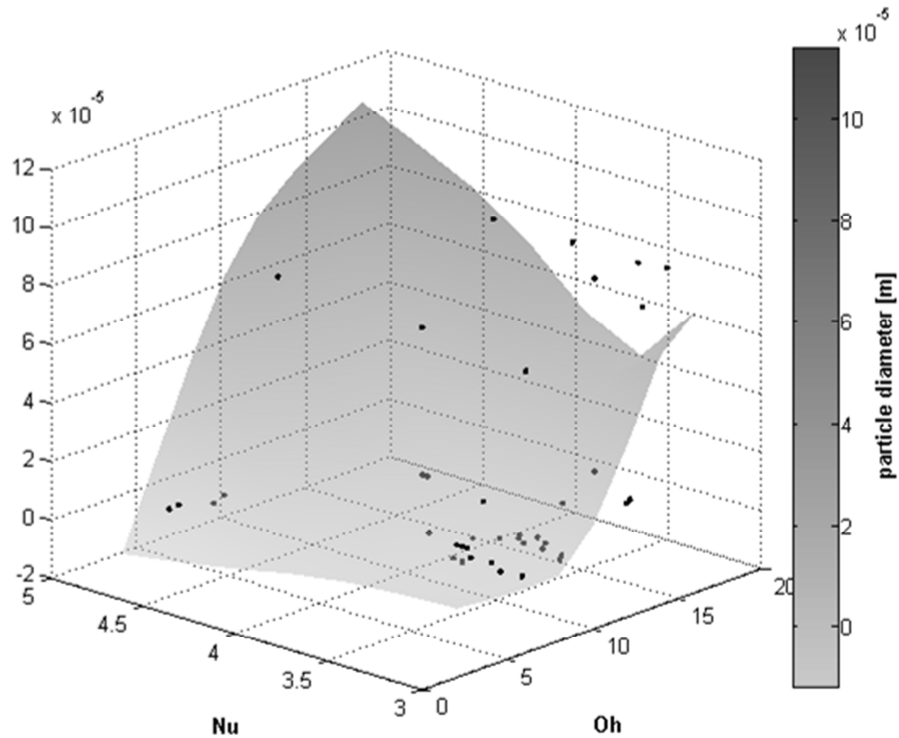


Figure 8.2: Particle diameter vs. Ohnesorge and Nusselt numbers

8.1.1 Outlet air properties

8.1.1.1 Temperature

There is a strong correlation between the inlet air temperature and the outlet air temperature, as shown in Figure 26. The correlation is almost linear, dropping only slightly at the outlet at higher temperatures. The two outlying temperatures that lie significantly below the trend-line occur for the larger nozzle at lower concentrations.

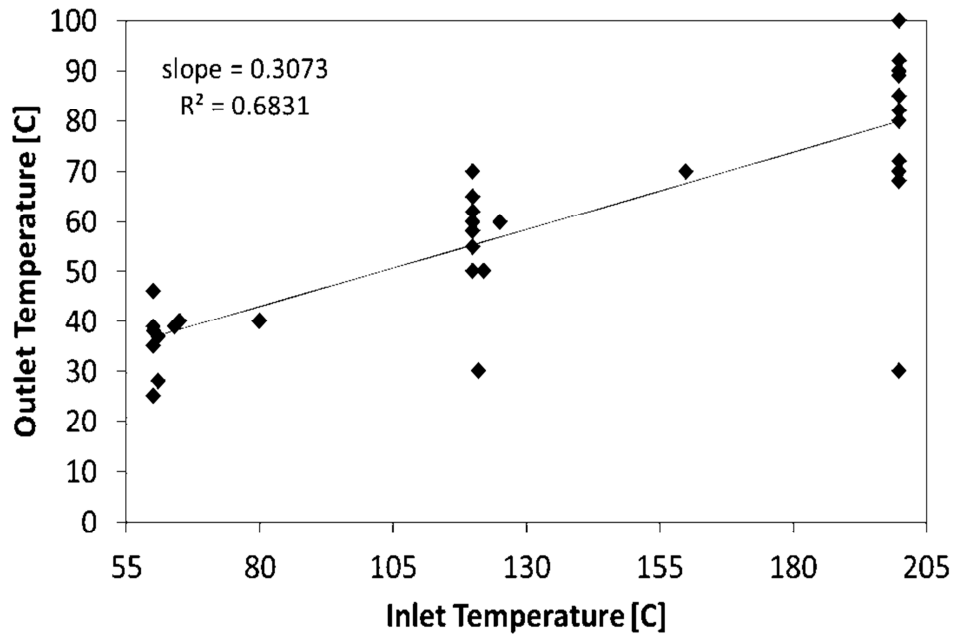


Figure 8.3: Outlet temperature vs. inlet Temperature

To limit dynamic effects during experimental preparation, water was allowed to run freely in the system at the set hot air inlet temperature, until temperatures reached equilibrium. Then the deionized water was replaced with the electrolyte solution and the experiment was started. Equilibrium heat-transfer conditions with respect to pure water existed before the experiment started, which is much closer than equilibrium conditions with respect to air. However a small drop in the outlet temperature was evident over the duration of the experiment in most cases.

8.1.1.2 Moisture content

The water vapor concentration in the exiting drying gas is higher than the entering gas.

8.1.2 The moisture taken with the exiting gas can be recovered in a crystallization process. Crystallization is where water is evaporated from a solution at elevated temperatures, then cooled again to ambient temperatures where crystals are formed. Since crystallization is a batch process, at least two crystallizers are required for to ensure continuous operation. Care must be taken to ensure that the condensing moisture from the exiting spray dryer gas stream does not mix with the evaporating water from the crystallizer.

8.1.2 Atomization flow rate

The strongest correlations with the atomization flow rate were found to occur with the nozzle diameter and atomization pressure. This was be expected, since the Equation for flow rate is:

$$\dot{m} = \rho v A \quad [8.1]$$

where ρ is the density, v is the velocity, and A is the area. The velocity is proportional to the back pressure driving the flow. The most interesting case happened at 2.5bar with the larger nozzle, as shown in Figure 27. In this case, the flow rate was also proportional to the temperature. This was due to viscosity and density differences between the different temperatures. **With the smaller nozzle, the boundary layer formed much of the flow profile.** However, with the larger diameter nozzle, there was a large bulk flow peak in the middle of the nozzle.

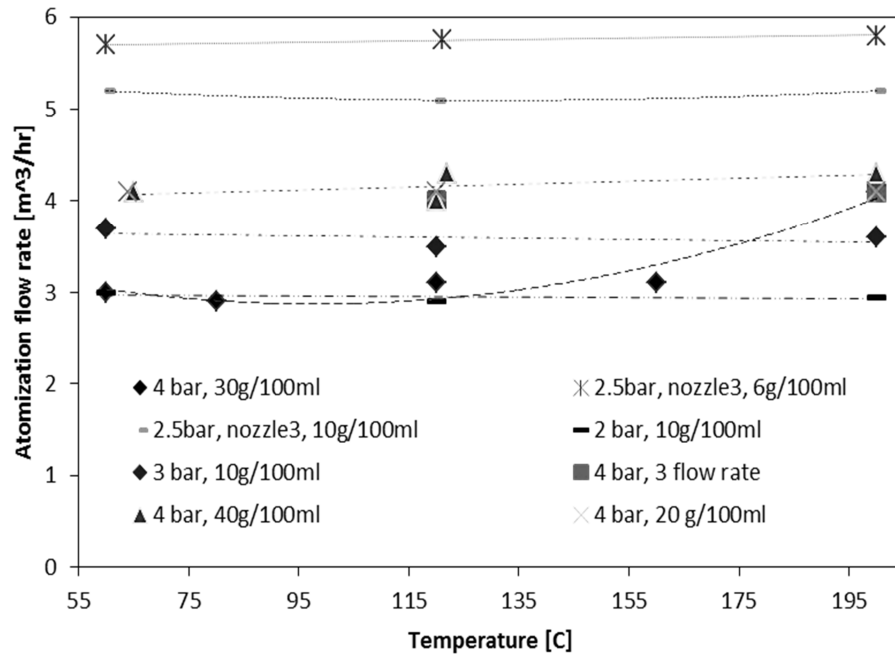


Figure 8.4: Atomization flow rate vs. temperature

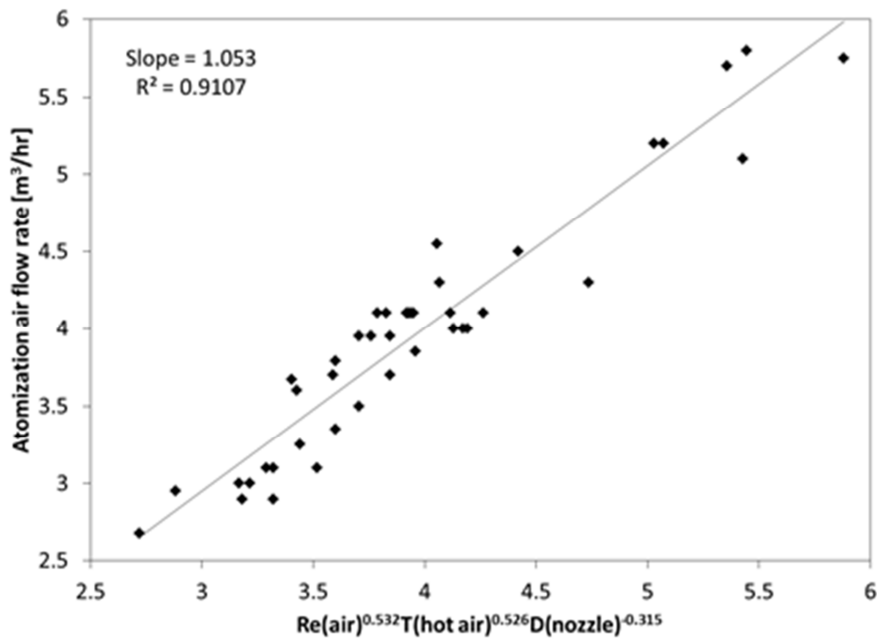


Figure 8.5: Atomization air flow rate correlation

Figure 28 shows a correlation for the atomization air flow rate and various parameters, including the atomization air Reynolds number, hot air temperature, and nozzle

diameter. The process of obtaining a correlation will be described in Section 8.1.5.5. With increased inlet air Reynolds number, the atomization air flow rate increases. The hot air temperature effects on the atomization air flow rate suggests that in the spray drying, the atomization air is heated as the unit supplies more energy to heat the hot inlet air. This in turn, changes the properties of the atomization air, such as its density. It is expected that the nozzle diameter will have an effect on the atomization air flow rate. The inverse effects are due to changes in the atomization air annulus when the inside liquid nozzle diameter changes. The atomization air flow rate correlation can be written as:

$$\dot{V}_{at.air} = 0.0042 \cdot Re_{at.air}^{0.532} T_{hot air}^{0.526} D_{nozzle}^{-0.315} \quad [8.2]$$

8.1.3 Particle morphology and crystallinity

In the process of spray drying of aqueous cupric chloride, the volatile compounds (water and some hydrochloric acid) evaporate from the droplets generated by the atomization nozzle. Because the volatile compounds are evaporated at the surface of the droplet, nucleation points at which precipitation occurs form first on the surface. This causes crystals to form, and grow internally into the droplet. The internal crystal structure of the particles in Figure 29 is fine: there are many small crystals that are formed.

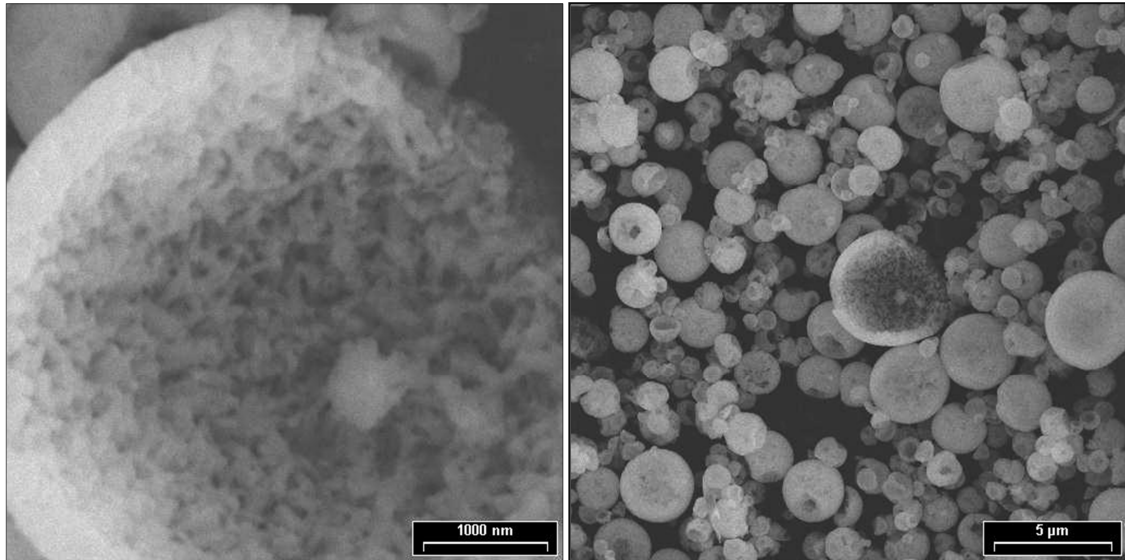


Figure 8.6: Particles dried at 200°C

In Figure 30, there is a more organized pattern formed in the internal crystal of the particle, and the pattern is much coarser.

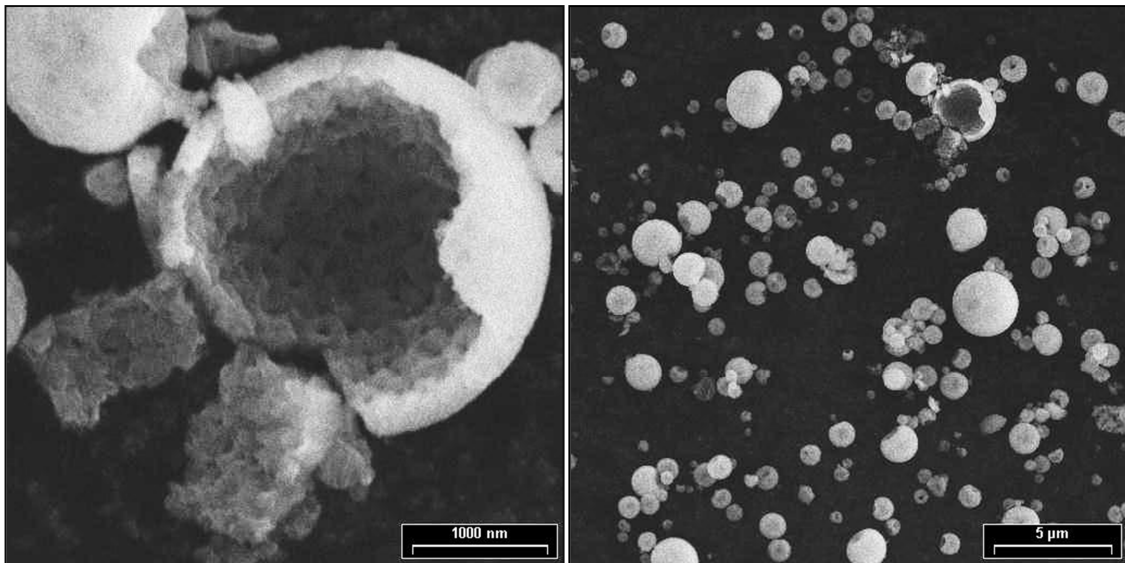


Figure 8.7: Particles dried at 120°C

Based on the SEM images, higher temperatures increase the number of nucleation points. Because of the increased number of crystals, there is less precipitate per crystal, and

the crystals are much smaller in size. This difference in crystal formation is further evident with the difference in color between the 200°C and 120°C particles.

It was postulated that at different temperatures and operating conditions, different drying mechanisms were dominant. This was clearly visible due to a color change of the collected samples from higher to lower temperatures. When completely dry, the anhydrous CuCl_2 forms crystals of a maroon-brown color, while the completely hydrated powder has a turquoise-blue form. When there is a mixture of crystals, the color ranges include light green, to an almost orange color, then to brown. The 60°C experiments yielded blue-green particles, the 120°C experiments yielded yellow-green particles, while the 200°C experiments yielded brown / yellow-brown particles.

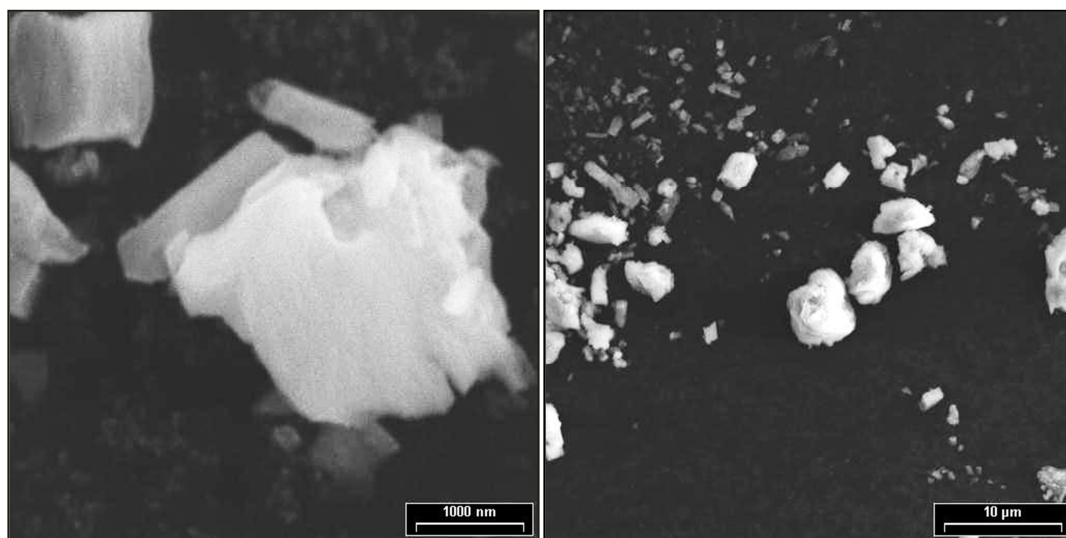


Figure 8.8: Particles dried at 60°C

Figure 31 shows that cooler temperatures yielded amorphous particles. As the drying rate slows, the number of nucleation points drops, and particles form more orderly shapes. For the purpose of analysis, the wall thickness was assumed uniform at all points in the

particle wall. However, measurements were taken for the wall thickness, as shown in Figure 32:

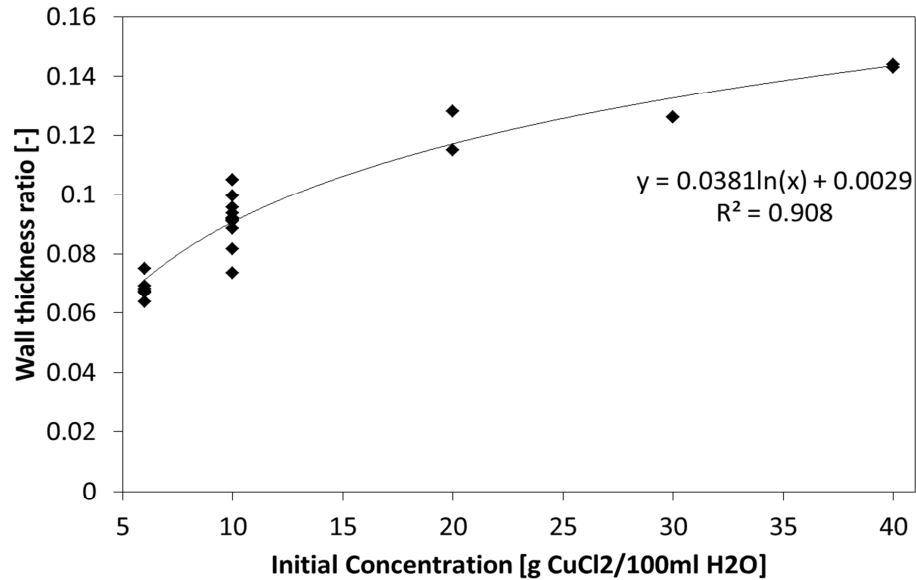


Figure 8.9: Initial concentration vs. wall thickness ratio

The process of obtaining the wall thickness ratio is described in Sections 8.1.5.2 and 8.1.5.3. Further, the wall was considered solid. Both these approximations were made because measurements were not possible with the data collected.

8.1.4 Particle moisture content

The moisture content showed preferential formation of either the dihydrate or anhydrous forms. Figure 32 below shows a curve following either the formation of the dihydrate, anhydrous, or, if drying was incomplete, a mixture of the dihydrate and unbound moisture. These observations are verified with the colour of the copper II chloride powder after collecting it from the spray dryer.

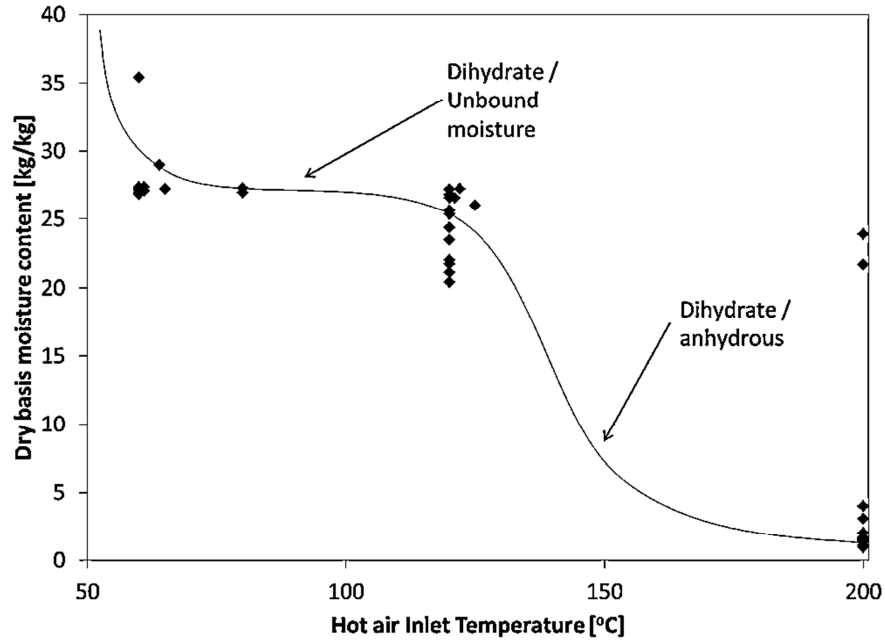


Figure 8.10: Moisture content vs. hot air inlet temperature

There are two outliers in Figure 33 in the top right. Both points arise from experiments with an increased liquid flow rate, suggesting a relationship between liquid flow rate and final moisture content. A comprehensive quantitative study of the effects on moisture content is beyond the scope of this work.

8.1.5 Particle size

Analysis was conducted with the agglomeration both included and excluded. The role of the agglomeration inside the fluidized bed was not determined. Experiments would need to be conducted to determine the magnitude of agglomeration and its role in the experiments.

8.1.5.1 Span

The largest span was observed with the highest temperatures, as shown in Figure 34. It is expected that the higher temperatures generate smaller particles, due to the differences

in densities between the hydrous and anhydrous forms, and due to faster drying times, meaning less time to agglomerate during the drying period. At higher temperatures, tighter lattices with smaller crystals were formed, corresponding to faster drying times. The reason for this overly large span was related to the storage of the dried particles. Although the particles were stored in sealed containers, they were slowly subject to atmospheric conditions. Most SEM images were taken after two months of storage in containers (due to scheduling with equipment). During this time, it was observed that particles slowly hydrated, and formed larger crystals.

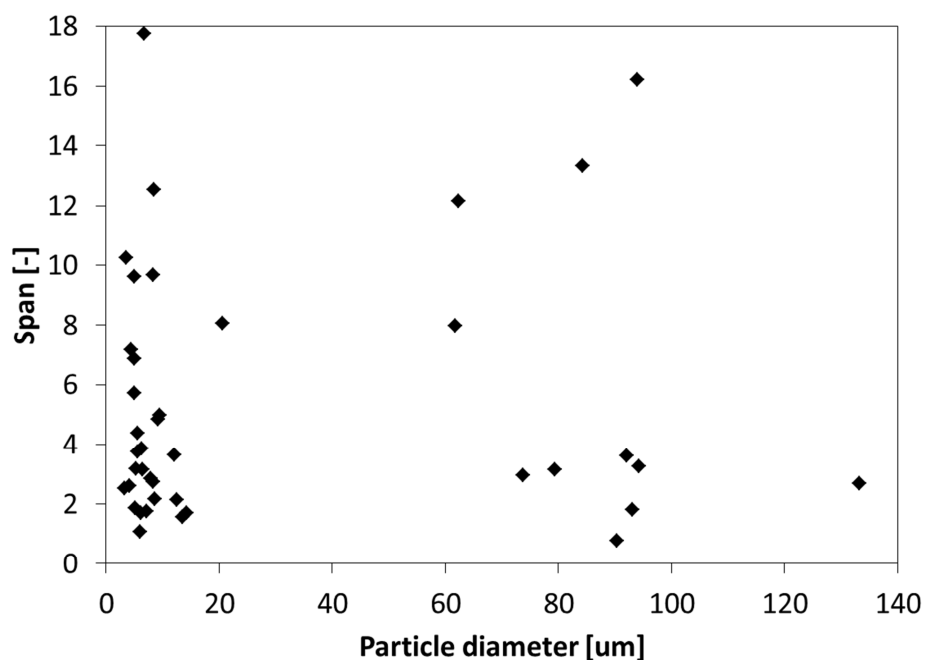


Figure 8.11: Span vs. Particle diameter

This re-hydration, along with agglomeration, was removed from further analysis of final particle diameter as described below.

8.1.5.2 Excluding agglomeration effects

After collecting data from the laser diffractometer and the SEM, it was evident that some data was misrepresented by the results of the laser diffractometer. The procedure used to determine the exact particle size is described here for Run #39 as an example. The parametric data from Run #39 is shown in Table 15.

Cold air		Hot air			Atomizing air		Atomizing liquid		
Room Temp	Room humidity	Inlet Temp.	Outlet Temp.	Flow rate	Flow rate	Pressure	Flow rate	Concentration	Temp.
C	%RH	C	C	m ³ /min	m ³ /min	bar	l/hr	g/100ml water	C
23	23	200	89	1	3.6	3	0.5	10	23

Table 8.1: Parameters from Run #39

Since the inlet temperature is 200°C, round particles with a narrow particle size distribution are expected. From the results of the laser diffractometer in Figure 35, it is evident that the particle size distribution is bimodal. About 37.7% of the volume of the particles have an average size of 229.5µm. This is a relatively large particle size. From the percentile data, the span is calculated for each sample from Run #39.

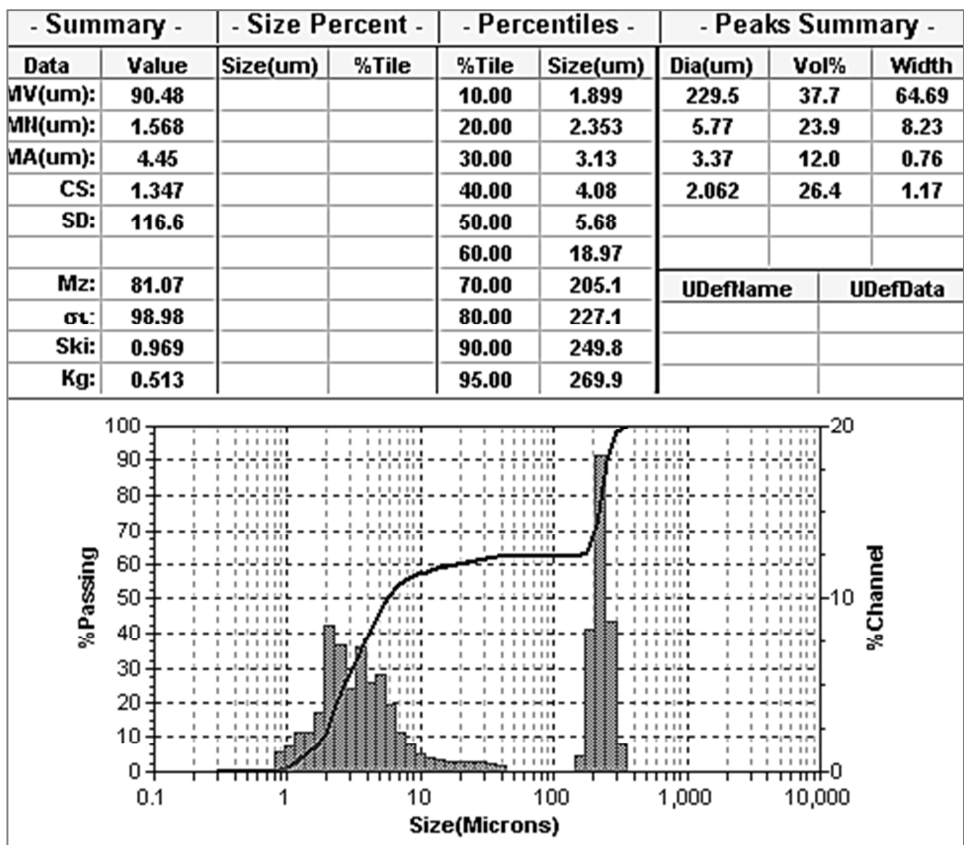


Figure 8.12: Results from laser diffractometer run no. #39-2

The results of the span indicate that there is considerable discrepancy for the first two samples, while the last sample shows a much narrower particle size distribution, as shown in Table 16.

Run	Percentiles			span
	10%	50%	90%	
1	1.875	6.44	354	54.68
2	1.899	5.68	249.8	43.64
3	1.482	3.19	6.95	1.71

Table 8.2: Spans calculated from three laser diffractometer runs from experiment #39

These results are verified with the SEM images taken of Run #39, shown in Figure 36. Due to the low pressures used in scanning electron microscopes, the particles viewed under the SEM are completely dry. Since the particles were not completely dry upon leaving the spray dryer under most runs, it should be expected that the particles observed under the laser diffractometer would be slightly larger than under the SEM.

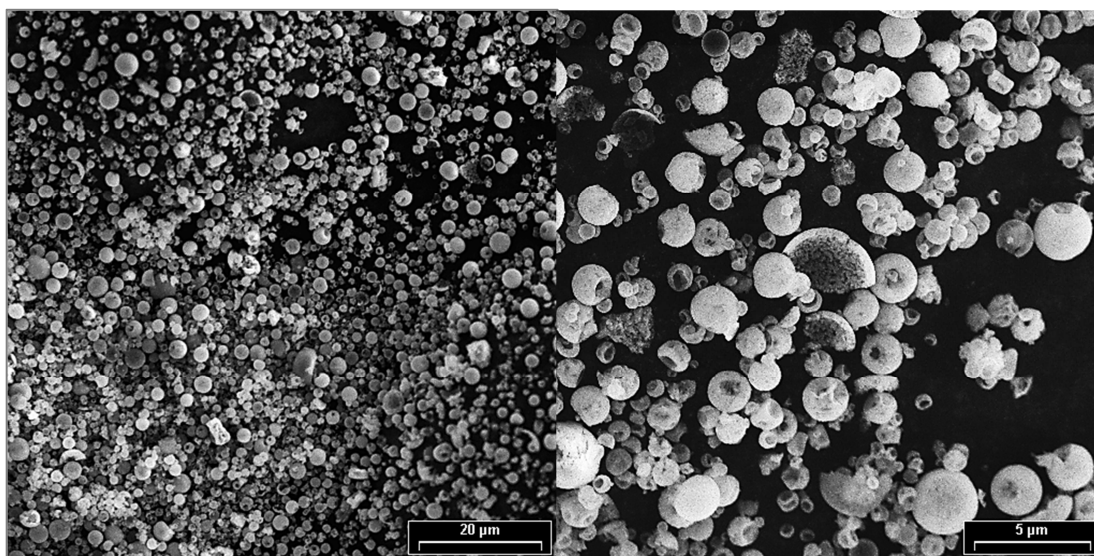


Figure 8.13: SEM images from Run #39

This volume change should be in proportion to the changes in crystal structure of cupric chloride as it changes from its dihydrate to anhydrous form, as with its density. The anhydrous form has a density of 3.386 g/cm^3 while for the dihydrate, it is 2.51 g/cm^3 . Therefore, the difference in volume taken up by the hydrate to the anhydrous form should be 34.5%, which, assuming round particles, corresponds to a difference in diameters of 10.5%, assuming that the final product is fully hydrated. This was most evident during the low temperature experiments.

For Run #39, the final moisture content was 0.928%, corresponding to a diameter-difference of 0.0974%, below the experimental uncertainty. The Sauter diameter from the SEM is much smaller than 229.5 μm , as recorded by the laser diffractometer. A method for excluding the agglomeration effects from laser diffraction was devised to determine the true particle diameter. Using the peak data from the laser diffraction data, the following Equation was determined, correlating the peak data to the Sauter diameter:

$$\sum_{i=1}^{N \text{ peaks}} \frac{\bar{m}_i \cdot (\text{Vol}\%)}{100} = D_{32, \text{calculated}} \cong D_{32, \text{measured}} \quad [8.3]$$

The R-squared value for the data set for this Equation was 0.991, obtained from Figure 37.

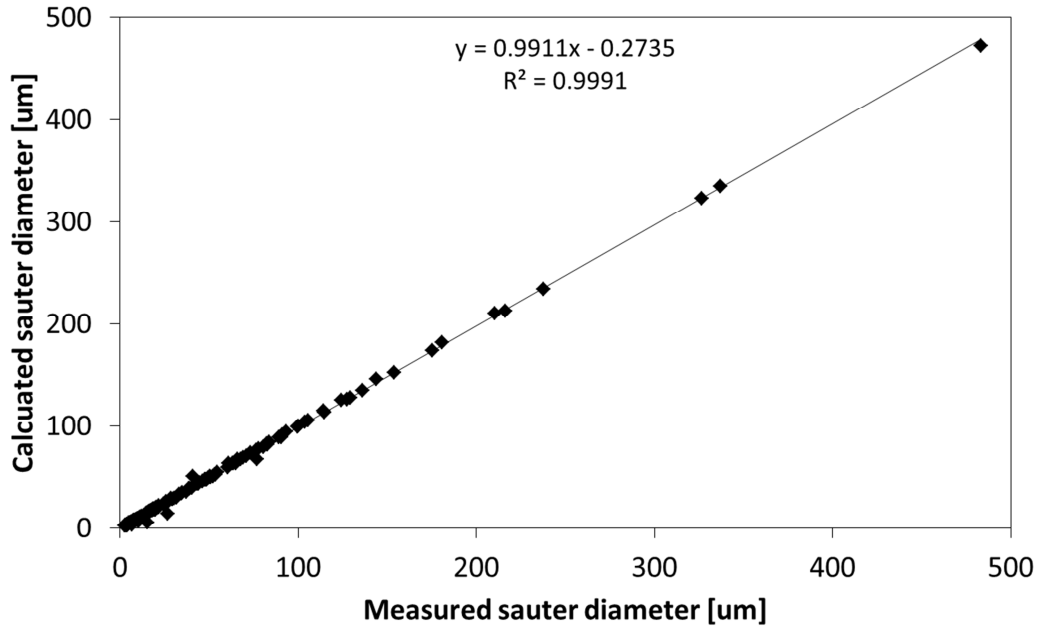


Figure 8.14: Diameter peak summation calculation

Using the peak summation Equation and the observed histogram for the laser diffractometer (Figure 34), the agglomeration was excluded:

$$D_{32, \text{no aglom.}} = \sum_{i=1}^{N - \text{largest}} \frac{\bar{m}_i \cdot (\text{Vol}\%)}{100 - (\text{Vol}\%)_{\text{largest}}} \quad [8.4]$$

In this way, all three samples were included in determining a representative Sauter diameter for each experiment, while the effects of agglomeration were excluded. This calculation is shown in Table 17 for experiment #39.

Run	Peaks summary								Meas. Sauter diam. (µm)	Calc. Sauter diam. (µm)	Standard deviation	No Aglom. Sauter diam.
	1st	Vol. %	2nd	Vol. %	3rd	Vol. %	4th	Vol. %				
1	327.3	46	5.26	17.5	3.36	10.6	2.031	25.9	153.9	153.9	169	3.338
2	229.5	37.7	5.77	23.9	3.37	12	2.062	26.4	90.48	90.48	116.6	3.736
3	5.45	36.3	3.38	20.4	2.063	43.3			3.99	3.99	1.919	3.990
Avg.									82.79	82.79	82.79	3.688

Table 8.3: Determining the Sauter diameter of Run #39

8.1.5.3 Equivalent droplet diameter

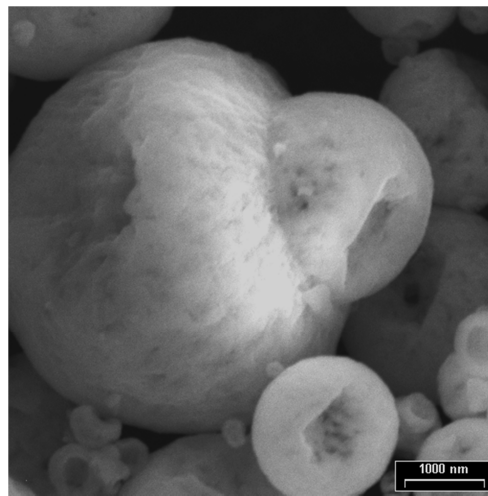


Figure 8.15: Run 21: droplet coalescence during mass transfer and drying

The droplet size correlations in Chapter 3 cannot be directly applied to spray drying. The correlations have been developed in the absence of heat transfer, and so they are not applicable directly to spray dried particles. To use these correlations, equivalent droplet diameters for each particle are determined using the process described below.

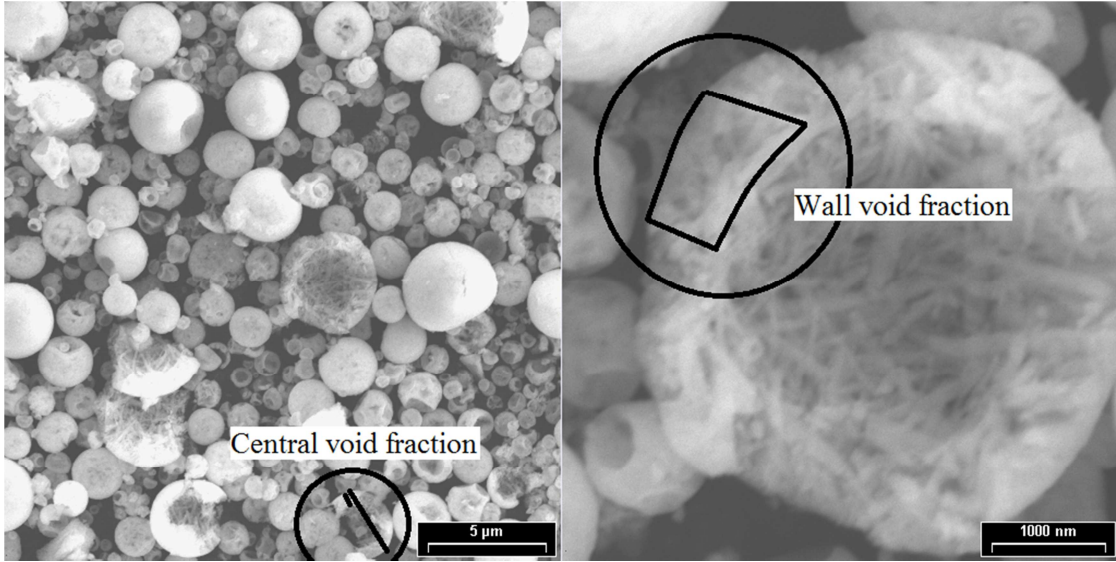


Figure 8.16: Central void fraction and wall void fraction

The central void fraction can be obtained by comparing the wall thickness to the particle diameter. These parameters are shown in Figure 39. However, the wall void fraction, which could be estimated by making a model for denticle packing, was too difficult to obtain through the SEM images. Further, some final particles were not hollow or spherical (as with the lower heat transfer cases). The void fractions are not applicable and not considered. By recording the final moisture content, and determining the air void packing, the equivalent droplet size was obtained from the spraying phenomenon.

Taking into consideration the initial concentration, a droplet mass balance is used as follows:

$$D_{32,final} = \frac{3}{4\pi} (V_0)^{1/3} \quad [8.5]$$

$$V_0 = \frac{m_{cucl2}}{10^{-6} \cdot c_{initial}} \quad [8.6]$$

$$m_{cucl2} = \rho_{cucl2} \cdot (V_{powder,final}) \cdot \left(1 - X \left(\frac{\rho_{cucl2}}{\rho_{water}} \right) \right) \quad [8.7]$$

$$V_{powder,final} = \frac{vf_w \cdot \pi}{12} \left[(D_{32,no\ aglom.})^3 - (D_{32,no\ aglom.} - 2 \cdot vf_c \cdot D_{32,no\ aglom.})^3 \right] \quad [8.8]$$

If the particle is solid, all the Equations were the same except Equation 8.6, where $vf_w = 1$ and $vf_c = 0.5$:

$$V_{powder,final} = \frac{\pi}{12} (D_{32,no\ aglom.})^3 \quad [8.9]$$

This was the case with lower temperature drying. To develop droplet size correlations, this final Sauter diameter was used.

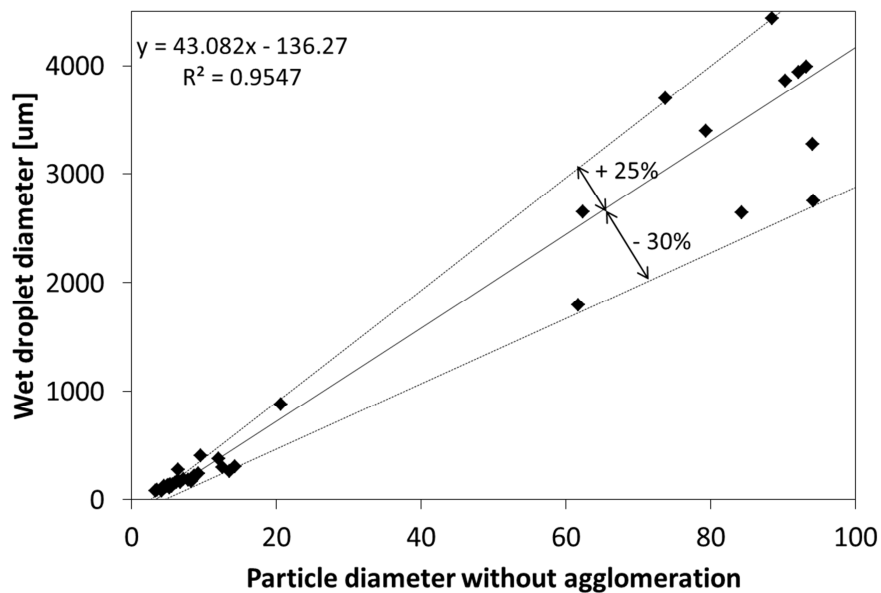


Figure 8.17: Discounting droplet drying, with non-spherical particles

The two bars on either side of the trend line represent 95% confidence intervals. If a correlation estimates the final diameter within +40%/-30% of the data, the correlation is made as accurate as the data. If non-spherical particles (equivalent diameters are much less accurate) are not included, the intervals fall to +10%/-20%, as shown in Figure 41.

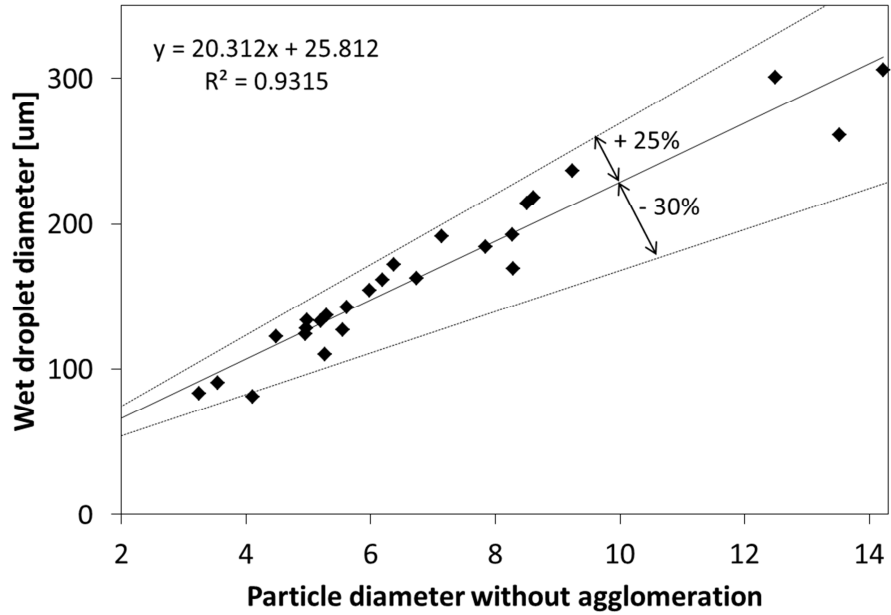


Figure 8.18: Discounting droplet drying, without non-spherical particles

This data analysis is performed to determine if the correlations for droplet diameter are accurate for the spray-dried particle set. The re-formatted data is shown in Figure 41 below, with an interpolated surface plot.

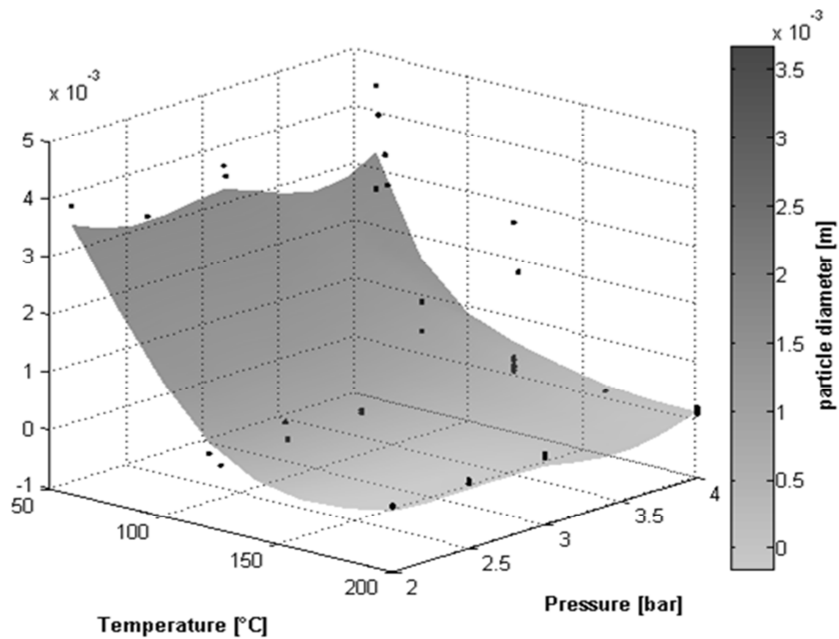


Figure 8.19: Droplet diameter vs. inlet temperature and atomization pressure

By having the final particle diameter and the mass of cupric chloride in the final particles, the equivalent concentration at the dried particle diameter can be determined. The equivalent final concentration at medium and high temperatures is *below* the saturation concentration for that droplet size. This shows that spray drying is a surface phenomenon: during drying, the bulk electrolyte concentration is below the surface electrolyte concentration. The surface reached saturation conditions and formed a crust while the centre of the droplet was far from saturation conditions.

8.1.5.4 Particle size correlation: previous models

The following three Figures (43, 44, 45) show how the previous droplet models correlated to the measured droplet diameters:

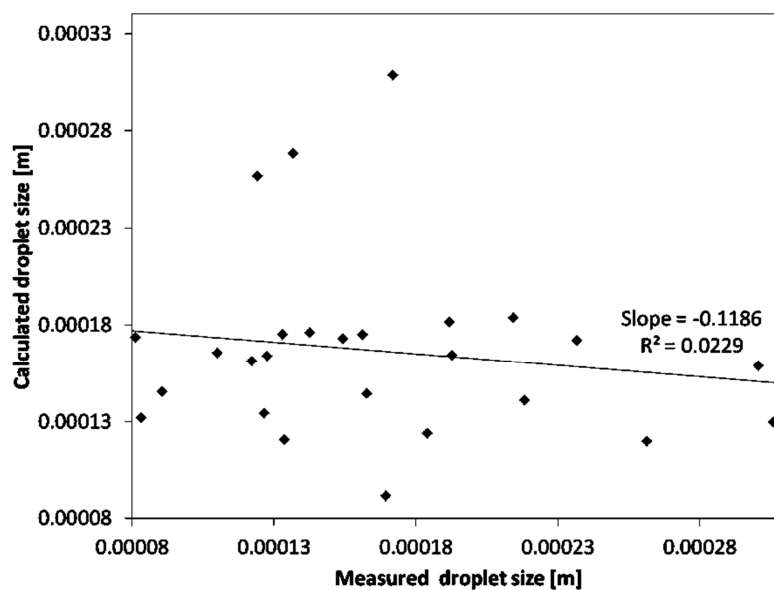


Figure 8.20: Calculated droplet size from Mulhem model vs. measured droplet size

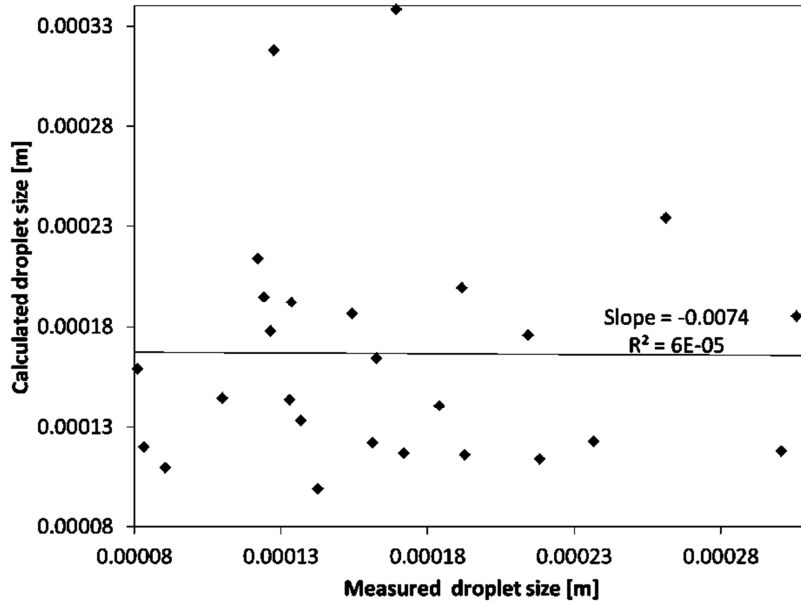


Figure 8.21: Calculated droplet size from Groom et al. model vs. measured droplet size

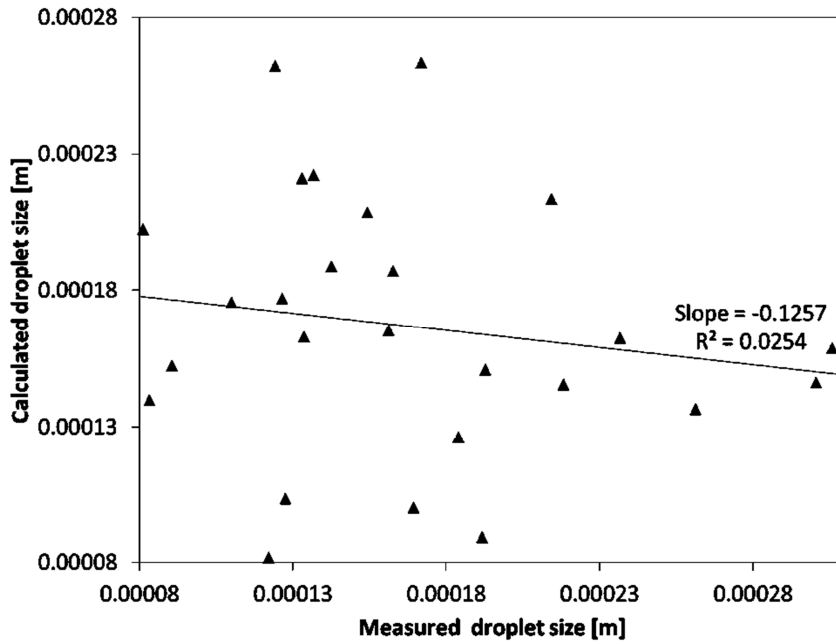


Figure 8.22: Calculated droplet size from Thybo model vs. measured droplet size

From the prior Figures it is evident that the droplet correlations without considering drying do not fit with the data set collected with drying.

8.1.5.5 Particle size correlation development

The general form of a correlation can be written as [78]:

$$y = C_0 \cdot t_1^{C_1} \cdot t_2^{C_2} \dots t_n^{C_n} \quad [8.10]$$

where t are the parameters that affect the final droplet size, and C represents the coefficients on the exponents.

Dimensional analysis was first conducted to determine the governing droplet size correlation coefficients. The essential parameters in the drying process to produce the final particles are shown in Table 18.

Variable	Description	SI units	Dimensions
D	Diameter of the droplet	m	L
ρ_{sol}	Liquid density	kg/m ³	M·L ⁻³
ρ_g	Gas density	kg/m ³	M·L ⁻³
μ_{sol}	Liquid dynamic viscosity	Pa·s	M·L ⁻¹ ·T ⁻¹
μ_g	Gas dynamic viscosity	Pa·s	M·L ⁻¹ ·T ⁻¹
k_{sol}	Liquid thermal conductivity	W/(m·K)	M·L·T·K ⁻¹
k_g	Gas thermal conductivity	W/(m·K)	M·L·T·K ⁻¹
Cp_{sol}	Heat capacity of liquid	J/(kg·K)	M·L·T·K ⁻¹
Cp_g	Heat capacity of gas	J/(kg·K)	M·L·T·K ⁻¹
σ	Surface tension	Pa·m	M·T ⁻²
S	concentration	kg/kg	-
V	Characteristic velocity	m/s	M·T ⁻¹

Table 8.4: Particle size parameters

To allow for simpler evaluation of the correlation, one more variable was introduced, a non-dimensional temperature:

$$\theta = \frac{T_{hot\ air} - T_{ambient}}{T_{mixture} - T_{ambient}} \quad [8.11]$$

This temperature is representative of the heat transferred to the liquid from the hot air.

For dimensional analysis, the Buckingham- Π theorem was used to determine the dimensionless Π groups. For the theorem to be applied, dimensionless Π groups are formed, based on dimensional homogeneity. The following expression is used to determine parameters affecting the particle diameter:

$$\frac{d_{32}}{d_0} = f(D, \rho_l, \rho_a, \mu_l, \mu_a, k_l, k_a, Cp_l, Cp_a, \sigma, S, V) \quad [8.12]$$

Each parameter was broken down into primary dimensions (M – mass, L – length, T – time, K – temperature). With consideration of these parameters, the following dimensionless groups in Table 19 were formed.

Π Term	Dimensionless group	Name
Π_1	$Nu^* = \frac{\ln(1 + B_T)}{B_T} (1 + (1 + RePr)^{1/3} Re^{0.077})$	Nusselt number
Π_2	$\mu/\sqrt{\rho\sigma L}$	Ohnesorge number
Π_3	$\sigma/(V^2 \rho D)$	Weber number
Π_4	μ_g/μ_{sol}	Viscosity ratio
Π_5	ρ_g/ρ_{sol}	Density ratio
Π_6	θ	Dimensionless Temperature
Π_7	$S_{T,\infty} = \frac{S(T)}{S_{max}(T)}$	Concentration ratio

Table 8.5: Dimensionless groups for the particle size correlation

The concentration ratio, $S_{T,\infty}$ is used instead of the actual concentration as it is more meaningful with regard to crystal formation. The concentration ratio is dependent on the

initial concentration of the solution, and the temperature to which the solution was brought during the initial heating process.

The resulting relationship is:

$$\frac{d_{32}}{d_0} = C \cdot Nu^{n_1} \cdot Oh^{n_2} \cdot We^{n_3} \left(\frac{\mu_g}{\mu_{sol}} \right)^{n_3} \left(\frac{\rho_g}{\rho_{sol}} \right)^{n_3} \theta^{n_3} S_{T,\infty}^{n_3} \quad [8.13]$$

In the Reynolds number from the first Π term, the final droplet diameters from the Mulhem, Thybo, and Groom correlations were used. In this way, fluid mechanics considerations were made in the initial jet breakup stage. Further, one key assumption was made. The time required for the initial jet breakup process approximately equaled the initial heating stage. Manual iterations were performed to determine the general correlation coefficients. It was determined that viscosity had the largest initial correlation to the final particle diameters.

8.1.5.6 First correlation iteration

All data was used for the initial correlations. Data was collected in excel, and a power function was fit to the data. The exponent on this power function was taken as the exponent on the correlation.

First step: Figure 46 shows the process of obtaining the power value for the viscosity term. It was determined that the viscosity term had the largest initial correlation. The power value was large since the spread in values for the viscosity was not as large as the spread for the particle diameters.

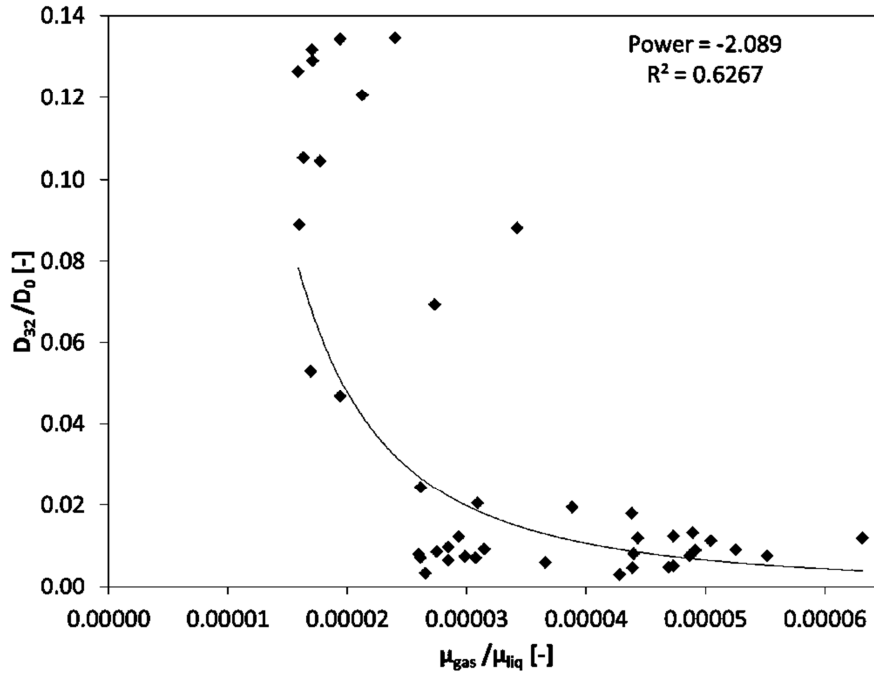


Figure 8.23: First step, obtaining power value

After obtaining the power, the values for the viscosity were raised to the power. The appropriate initial constant term was determined, and a new plot was made to show the correlation value, as shown in Figure 47. The statistical R-squared value was 0.6267, which is an acceptable indication that the data correlates at this point. The correlation at this point is shown below in Equation 8.14, where C is a constant determined from curve-fitting.

$$\frac{d_{32}}{d_0} = C \cdot \left(\frac{\mu_g}{\mu_{sol}} \right)^{-2.089} \quad [8.14]$$

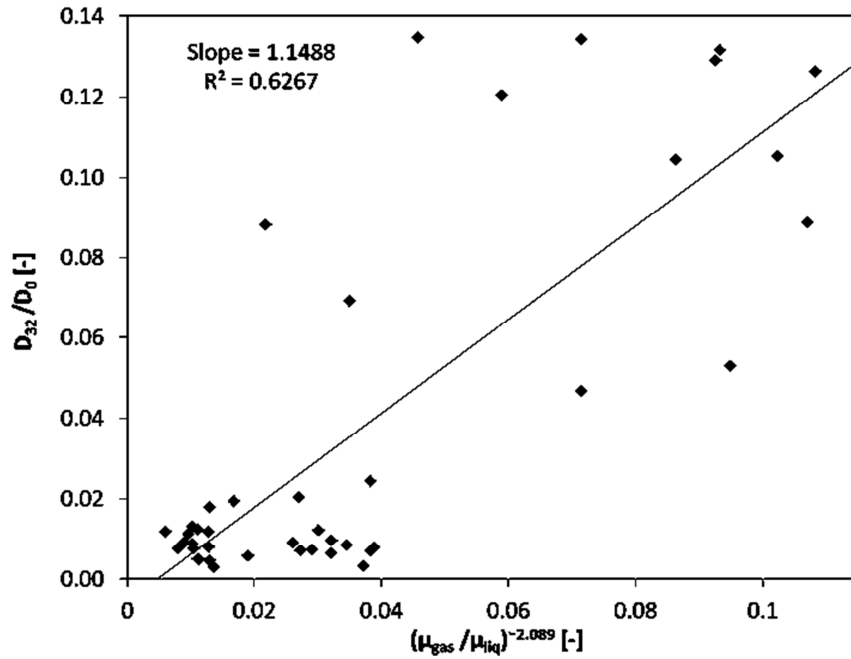


Figure 8.24: First step after obtaining the power value

Second step: The second step created another scatter plot, and line of best fit, to find the power value for the concentration ratio.

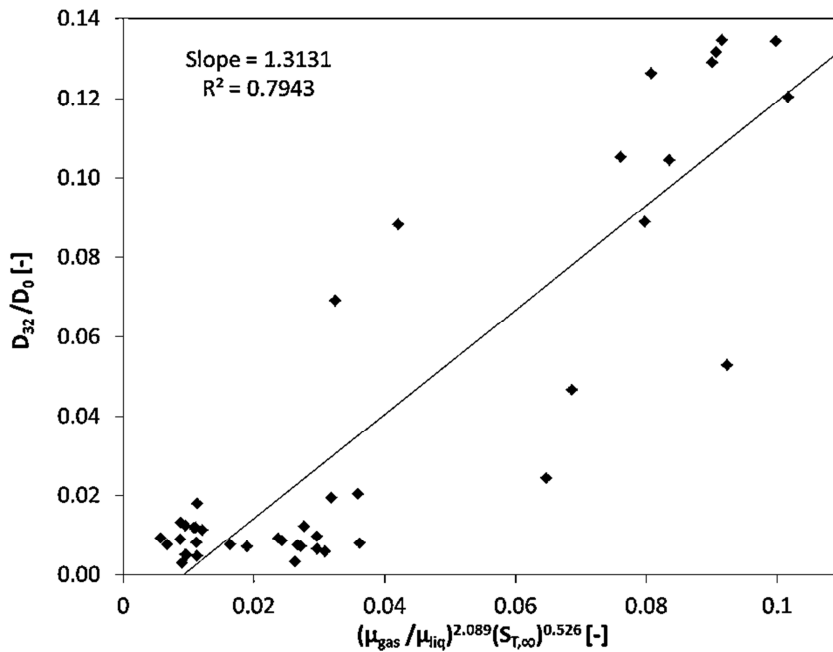


Figure 8.25: Second step after obtaining the power value

Figure 48 shows the process of obtaining the power value for the concentration ratio. The exponent on the concentration ratio, after using a power line of best fit, was found to be 0.526. This process gave an R-squared value of 0.7943, which suggests that the data correlates well at this point. The correlation becomes:

$$\frac{d_{32}}{d_0} = C \cdot \left(\frac{\mu_g}{\mu_{sol}}\right)^{-2.089} (S_{T,\infty})^{0.526} \quad [8.15]$$

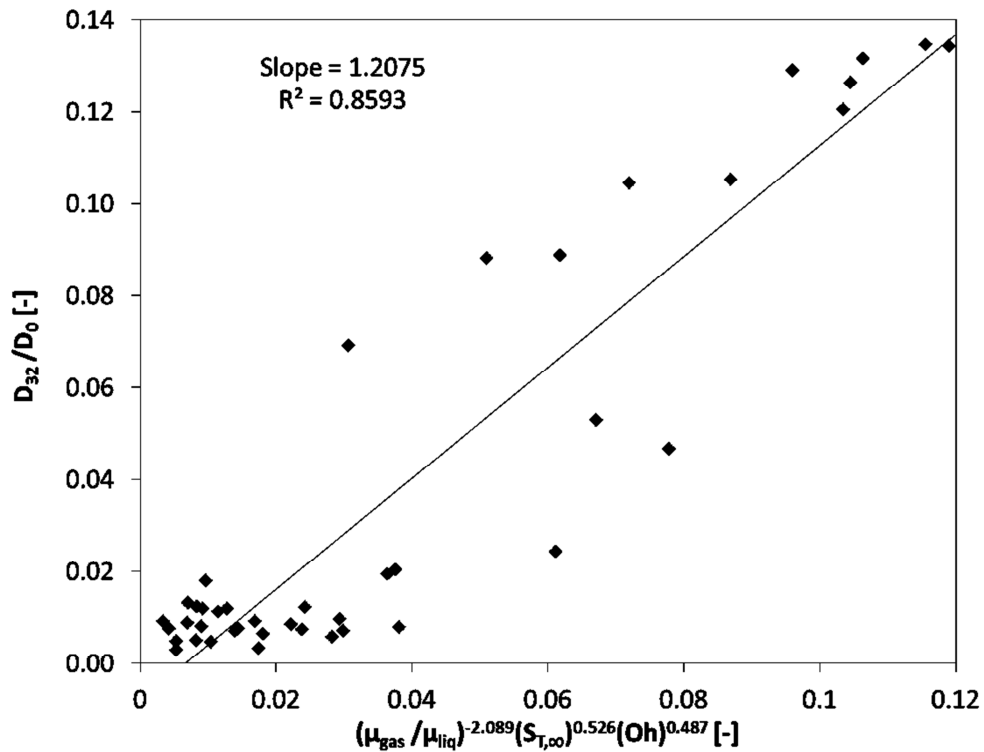


Figure 8.26: Third step after obtaining the power value

Third step: Figure 49 shows the process of obtaining the power value for the Ohnesorge number. The R-squared value is now 0.8593, which is a good range. Using the same process, the correlation becomes:

$$\frac{d_{32}}{d_0} = C \cdot \left(\frac{\mu_g}{\mu_{sol}}\right)^{-2.089} (S_{T,\infty})^{0.526} (Oh)^{0.487} \quad [8.16]$$

The same process was used for all other steps to find the final correlation. Using the initial values from the Mulhem correlation gave the best fit for the final values.

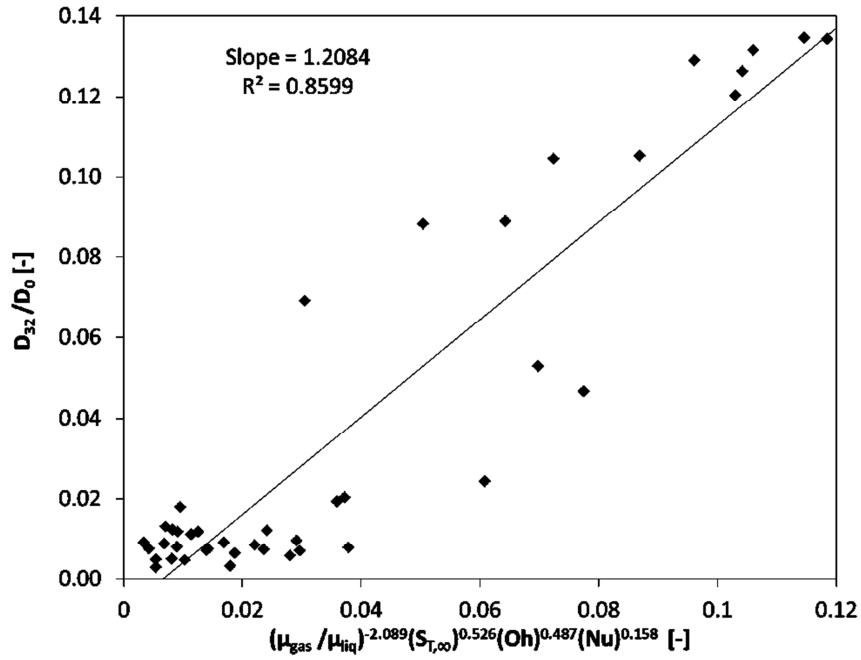


Figure 8.27: Fourth step after obtaining the power value

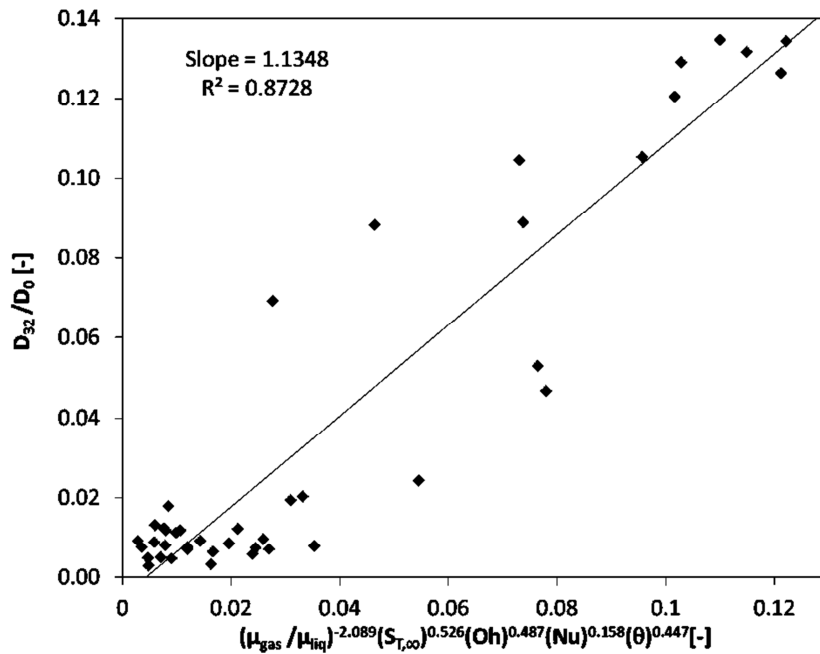


Figure 8.28: Fifth step after obtaining the power value

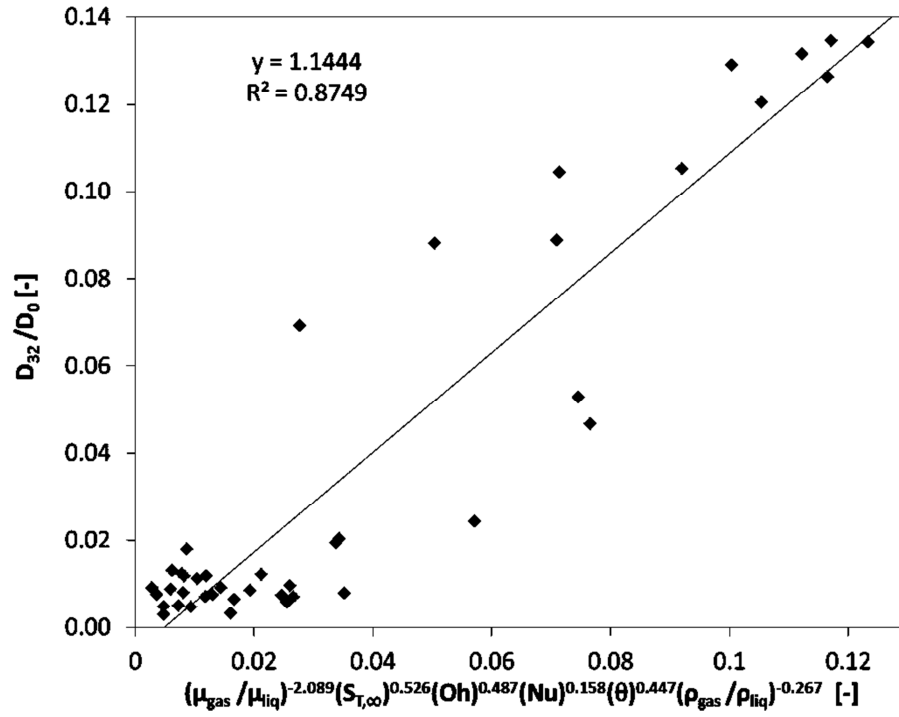


Figure 8.29: Fifth step after obtaining the power value

Sixth and final step: Figure 53 below shows the final correlation scatter plot.

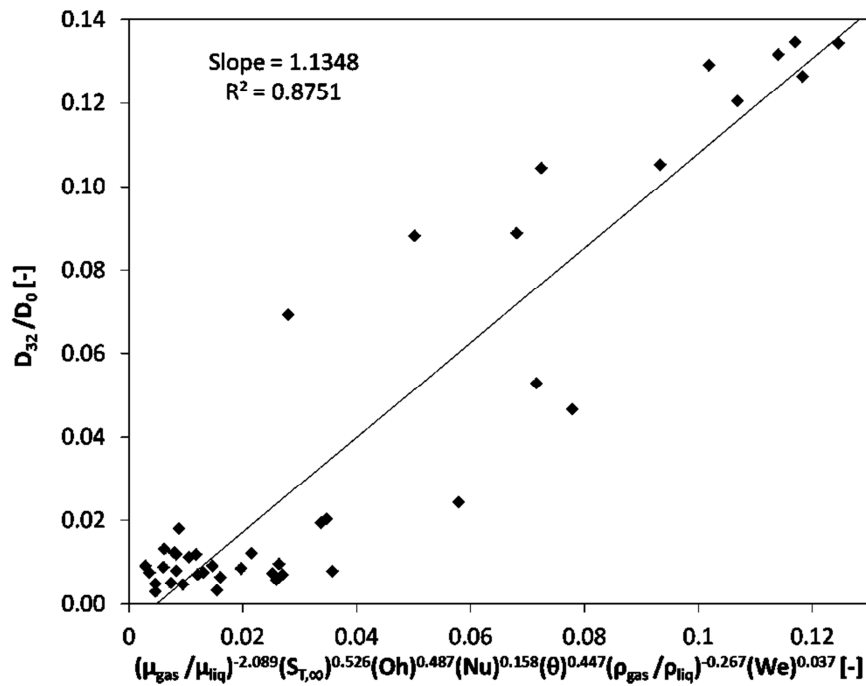


Figure 8.30: Sixth step after obtaining the power value

The R-squared value is 0.8751, which is an acceptable value for a correlation. The final correlation is:

$$\frac{d_{32}}{d_0} = C \cdot \left(\frac{\mu_g}{\mu_{sol}}\right)^{-2.089} (S_{T,\infty})^{0.526} (Oh)^{0.487} (Nu)^{0.158} (\theta)^{0.447} \left(\frac{\rho_g}{\rho_{sol}}\right)^{-0.267} (We)^{0.037} \quad [8.17]$$

From Figures 51, 52, and 53, the final three R-squared values do not differ considerably.

Therefore, the final correlation can be truncated to:

$$\frac{d_{32}}{d_0} = C \cdot \left(\frac{\mu_g}{\mu_{sol}}\right)^{-2.089} (S_{T,\infty})^{0.526} (Oh)^{0.487} (Nu)^{0.158} (\theta)^{0.447} \quad [8.18]$$

8.1.5.7 Thybo droplet based particle correlation

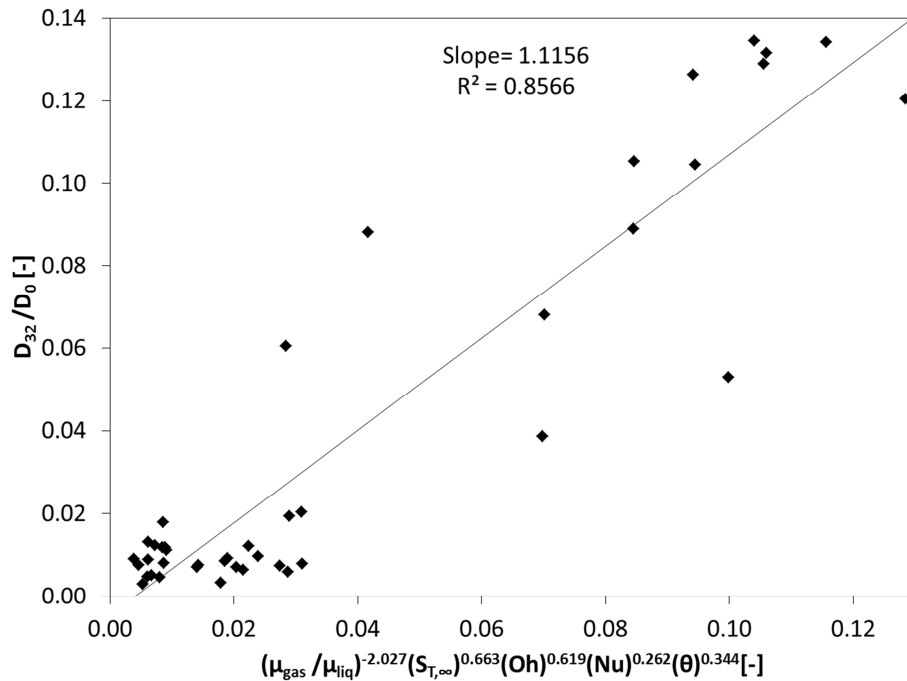


Figure 8.31: Thybo-based correlation after fifth step

After the fifth step in Figure 54, the best R-squared value for the correlation for the Thybo-based droplets is 0.8566, which is less than 0.8726 for the Mulhem based droplets. This suggests that the Mulhem correlation is better a fit for the data set. The final Thybo-based correlation is:

$$\frac{d_{32}}{d_0} = C \cdot \left(\frac{\mu_g}{\mu_{sol}}\right)^{-2.027} (S_{T,\infty})^{0.63} (Oh)^{0.619} (Nu)^{0.262} (\theta)^{0.344} \quad [8.19]$$

All exponents on both the Thybo and Mulhem based correlations are within the same range.

8.1.5.8 Groom droplet based particle correlation

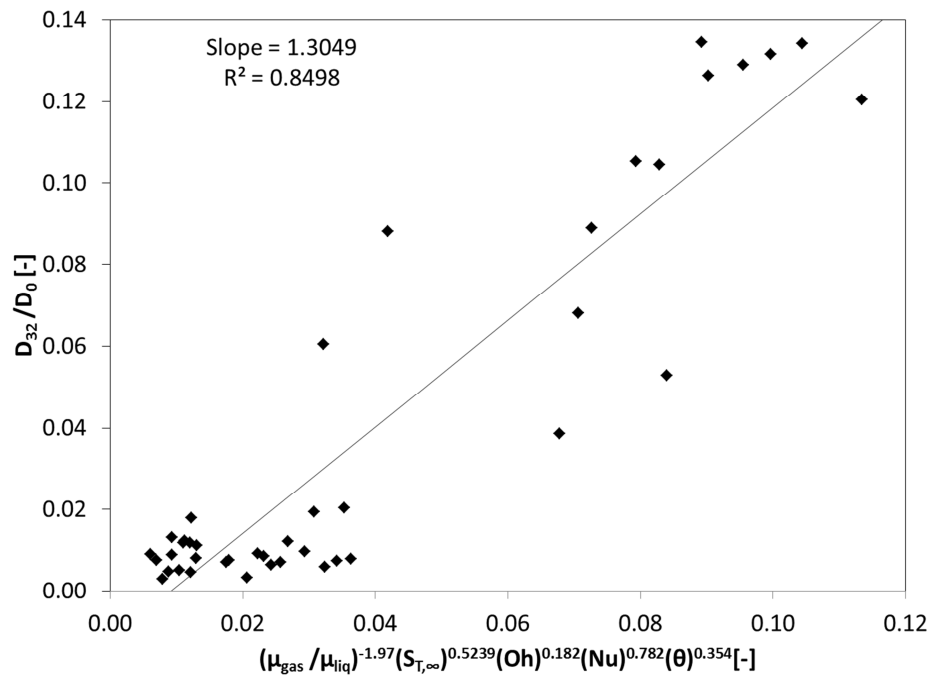


Figure 8.32: Groom-based correlation after fifth step

After the fifth step in Figure 55, the best R-squared value for the correlation for the Groom-based droplets is 0.8499, which is less than the value for both the Thybo-based and

Mulhem-based correlations. This suggests that the Groom correlation for the initial droplets is the poorest fit to the current data set. The final Groom-based correlation is:

$$\frac{d_{32}}{d_0} = C \cdot \left(\frac{\mu_g}{\mu_{sol}}\right)^{-1.97} (S_{T,\infty})^{0.524} (Oh)^{0.182} (Nu)^{0.782} (\theta)^{0.354} \quad [8.20]$$

The exponents on the Groom-based correlation have the same magnitude, but not the same order as the Groom and Thybo based correlations. However, the initial correlations are different as well. For practical purposes, the truncated version of the Mulhem-based correlation is used as the final correlation, with an r-squared value of 0.8723 is Equation 8.17.

8.1.6 Particle size distribution

Various distribution models were compared to determine the best fit to the spray dried particle distributions. Log-normal, upper-limit log, root-normal, and Rosin-Rammler distributions were all compared against the data sets. Various cases were chosen to conduct the analysis. Figure 55 shows the best-fit curves for the 2nd run, at 80°C. The Log-normal distribution provides the best fit for the data. For Run 2, the air inlet air temperature was 80°C, and air outlet temperature = 40°C. The drying air flow rate was 0.8 m³/min. The atomization liquid flow rate was 0.58 litres / hour, while the atomization pressure was 4bar, and the solids concentration was 9%.

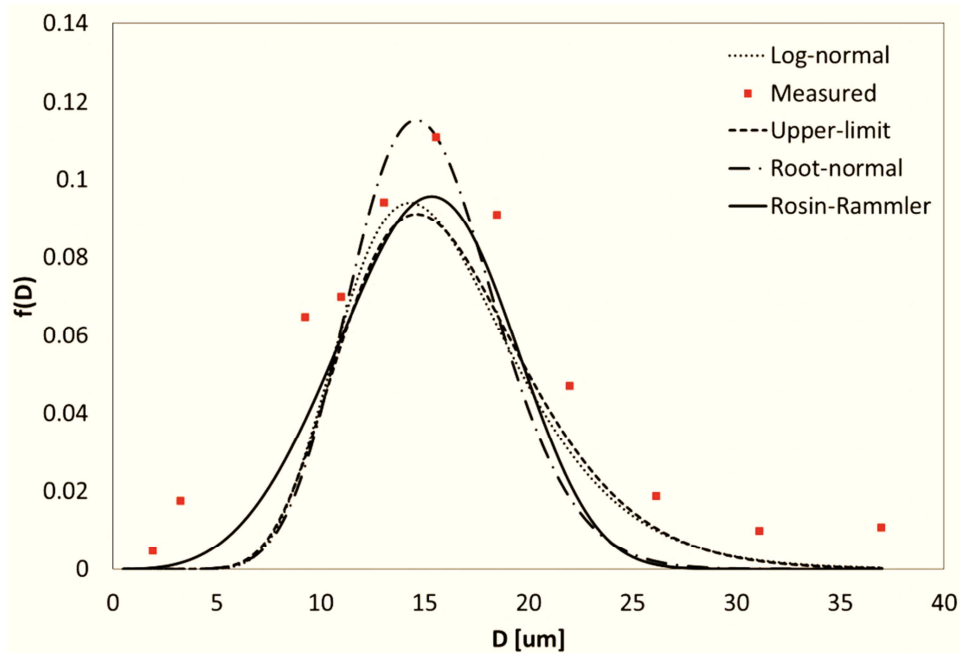


Figure 8.33: Run no. 2 (80°C, 0.7mm nozzle) particle results

Figure 57 shows the SEM graphs of these particles. The particle shape was found to be closely agglomerated, and mostly non-spherical. The final moisture content was 27%.

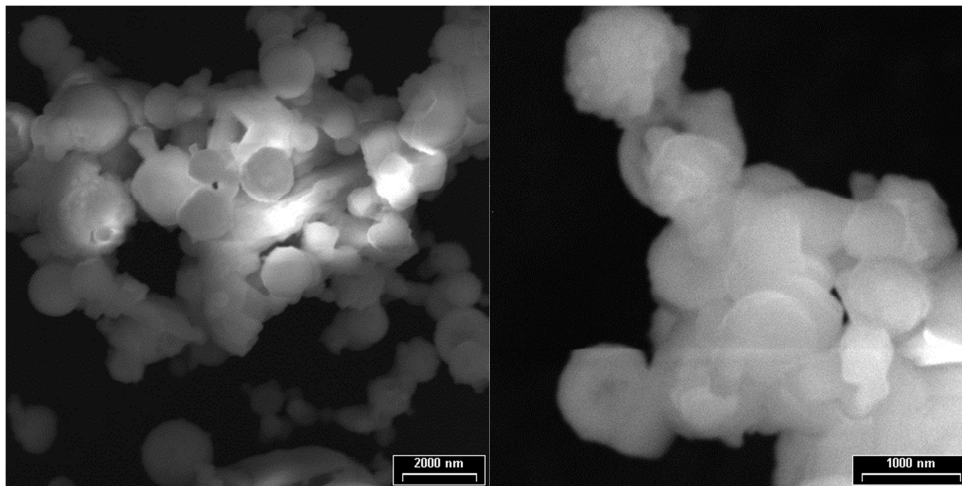


Figure 8.34: Run no. 2 (80°C, 0.7mm nozzle) SEM results

Figures 58-61 below show the best-fit data for Runs no. 3 and 36, at 120°C and 200°C, respectively. For both cases, the final particles were nearly spherical. Other best-fit results can be found in Appendix D.

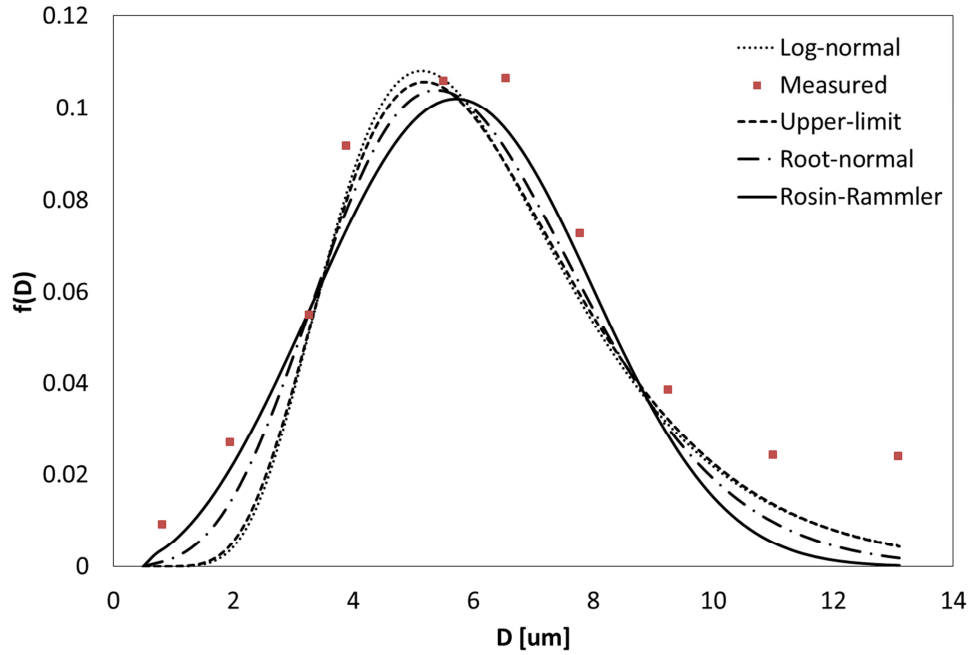


Figure 8.35: Run no. 3 (120°C, 0.7mm nozzle) particle results

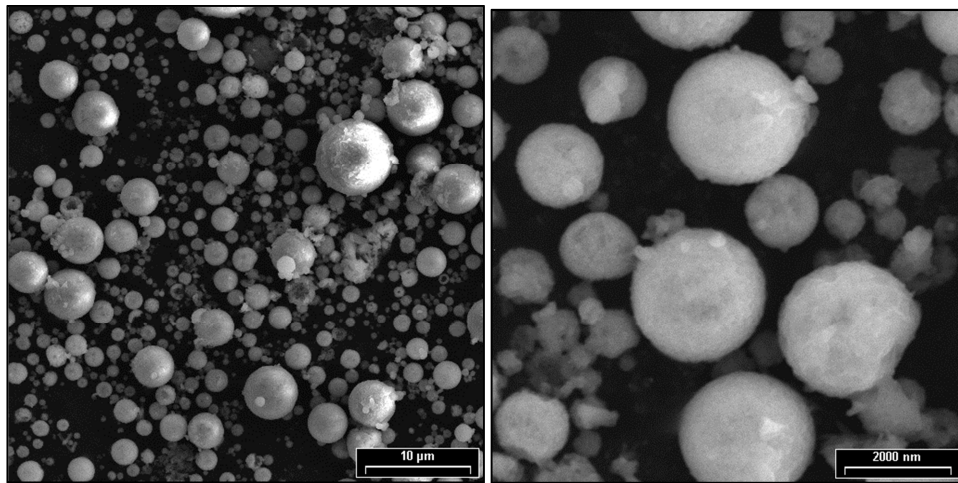


Figure 8.36: Run no. 3 (120°C, 0.7mm nozzle) SEM results

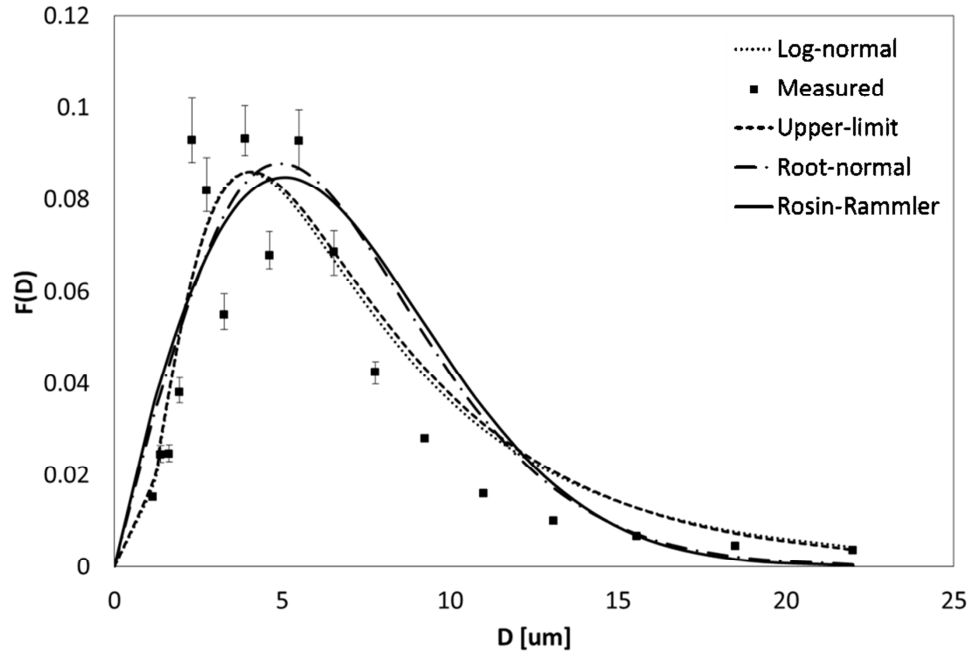


Figure 8.37: Run no. 36 (200°C, 0.7mm nozzle, 1/2 nominal pressure) particle results

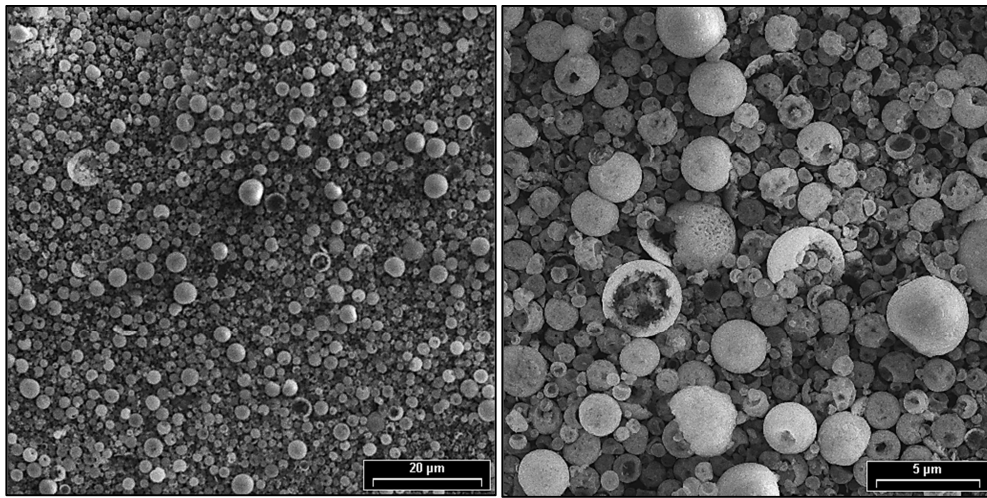


Figure 8.38: Run no. 36 (200°C, 0.7mm nozzle, 1/2 nominal pressure) SEM results

Table 20 below shows the best-fit results, with the respective Bayesian criterion values. The lowest Bayesian value is the most desirable.

Table 8.6: Particle size distribution best fit results

Run	Log-Normal	Upper-Limit	Root-Normal	Rosin-Rammler	Best Fit
60C	0.0001242	0.04300	0.03351	0.02884	Log-Normal
80C	0.0003429	0.08060	0.08445	0.07019	Log-Normal
120C	0.0002077	0.05687	0.05059	0.0001771	Rosin-Rammler
160C	7.192E-05	7.014E-05	6.588E-05	7.9810E-05	Root-Normal
1.5x Liq. flow	4.338E-05	4.588E-05	7.779E-05	8.670E-05	Log-Normal
0.5x pressure	0.0001725	0.0001806	0.0002596	0.0002830	Log-Normal

Table 21 below shows the final resulting parameters for all the distribution models analysed.

Table 8.7: Parameter values for curve fits

Run no.	Temp.	log normal		upper limit		Dmax	root normal		Rosin-Rammler	
		sigma	Dbar	sigma	Dbar		sigma	Dbar	q	D
1	60C	1.49	17	1.63	20.2	103.8	0.83	16.4	2.78	18.6
2	80C	1.33	15.5	1.39	18	123.7	0.45	15	4.13	16.4
3	120C	1.45	5.9	1.5	6.4	78.4	0.45	5.8	3.06	6.5
4	160C	1.52	6.4	1.56	6.8	97	0.51	6.2	2.73	7
27	120C	2.00	12.2	1.9	13.1	100	1.1	12.2	1.83	15.1
33	160C	2.08	21.2	2.35	26	100	1.35	20.1	1.83	24.7
36	200C	2.01	6.5	2.07	6.9	100	0.74	6.1	1.9	7.5

There is a clear trend for the average particle size, Dbar, to decrease with increasing temperature. The particle size distribution, as determined by the value of sigma, also decreases with increasing temperature. It was seen that agglomeration had a significant role

in determining the size of particles. Agglomeration causes the sizes of particles to seem larger than via laser diffraction. This phenomenon is visible in the SEM images.

8.1.7 Particle flowability

Two methods of determining the particle flowability were measured: Hausner ratio and compression ratio. The correlation between the Hausner ratio and compression ratio is shown in Figure 61.

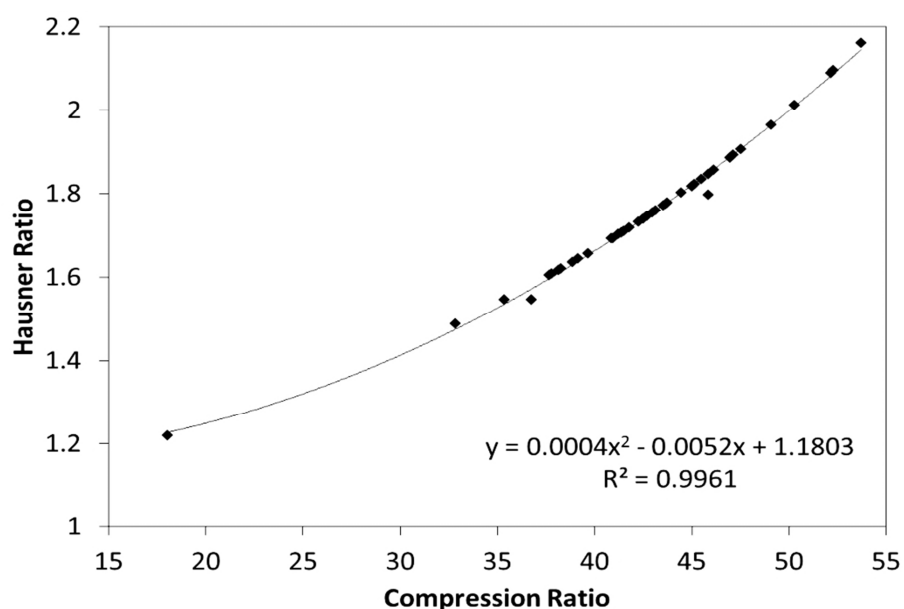


Figure 8.39: Correlation between Hausner ratio and compression ratio

From Figure 62, it is apparent that the Hausner ratio and the compression ratio are not independent of each other. Both will represent the dataset in the same way. To stay consistent with previous studies, the Hausner ratio was chosen. The Hausner ratio was compared to the droplet size for each experiment, as shown in Figure 63.

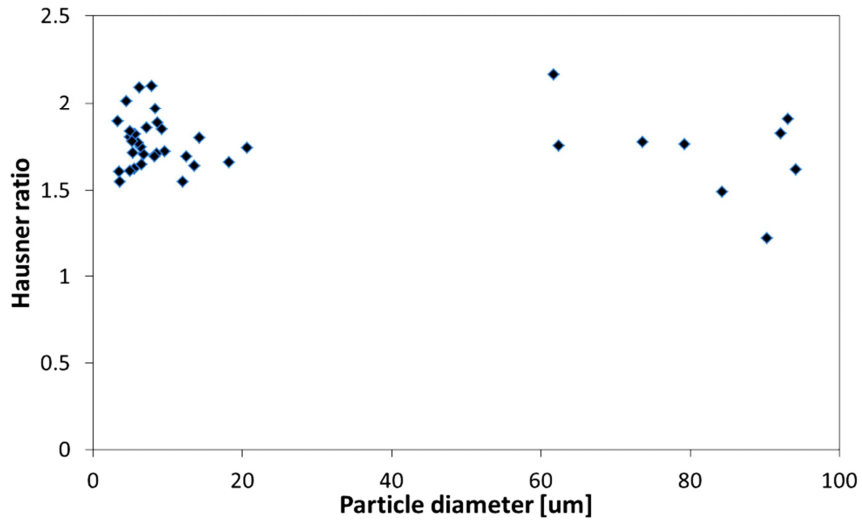


Figure 8.40: Hausner ratio vs. particle diameter [all data]

There is no self-evident trend with this data. The right side of the Table represents data from the lower heat addition rates, for which larger non-spherical particles were formed. If this data is omitted, the following data is obtained in Figure 65.

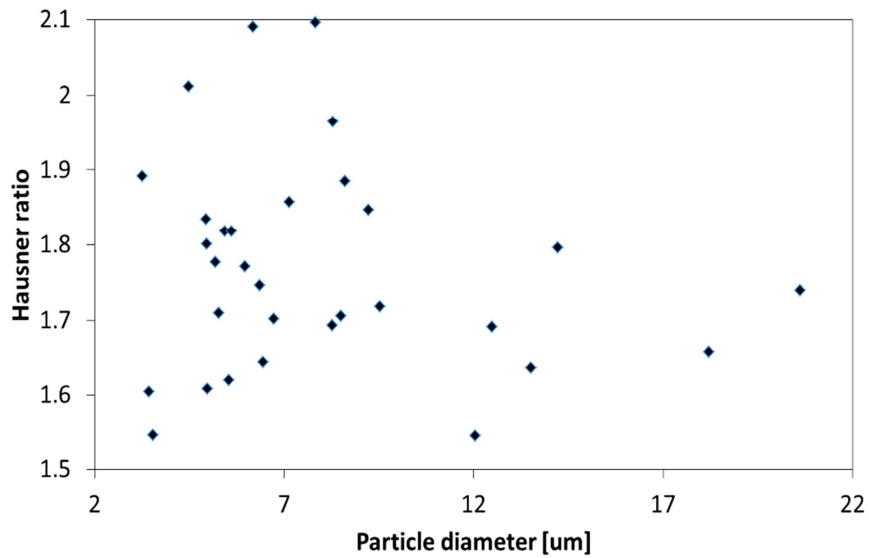


Figure 8.41: Hausner ratio vs. particle diameter [higher heat additions]

There is a slight trend from the top left to the bottom right. This trend is captured in the following correlation:

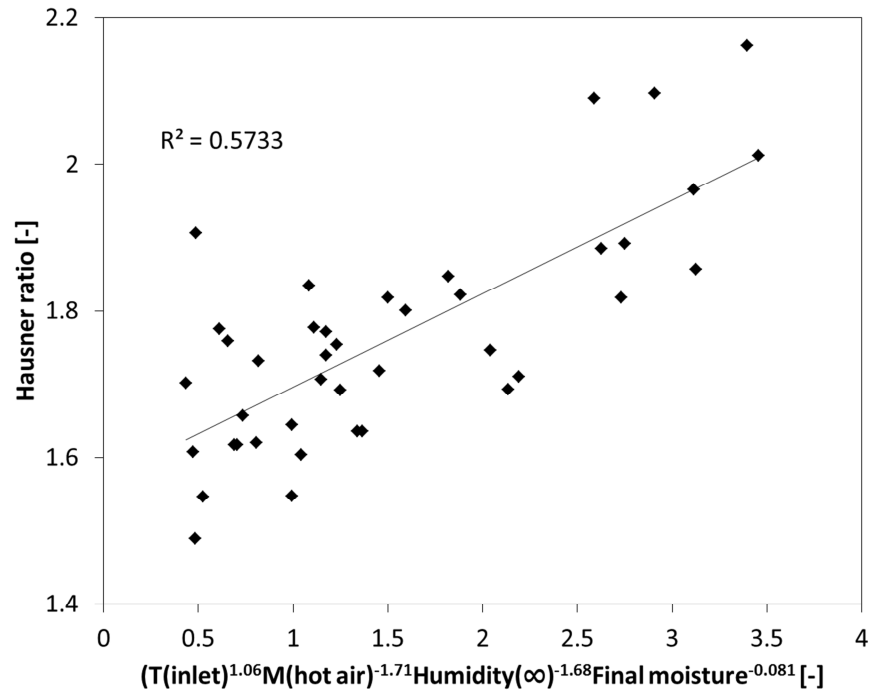


Figure 8.42: power law Equation for Hausner ratio

$$HR = C \cdot T_{inlet}^{1.06} \dot{m}_{hot\ air}^{-1.71} RH_{room\ air}^{-1.68} \dot{m}_{at.\ air}^{0.68} X_{final}^{-0.009}$$

[8.20]

From Equation 8.20, it can be inferred that the Hausner ratio increases with increasing inlet air temperature, atomization air flow rate, room humidity, and it decreases with the final moisture content. Most other variables do not have a significant impact on the Hausner ratio. This occurs that the final moisture content does not have a significant impact on the Hausner ratio. This could be because the final moisture content does not take into account the different hydrates that form with copper II chloride. Moisture can be bound in the crystal structure. This moisture would not cause the particles to become stickier. It is believed that only surface moisture, which is not directly measured by the moisture content, would have a significant impact on the Hausner ratio.

8.2 Convective drying

These experiments were used to calculate the drying rate under various temperatures, for application in the characteristic rate drying curve. The drying rate Equation can be directly applied to a CFD code, for spray drying experiment predictions.

8.2.1 Dihydrate

The results from the convective drying experiments are shown in Figure 65 below. A linear fit is shown for each drying rate.

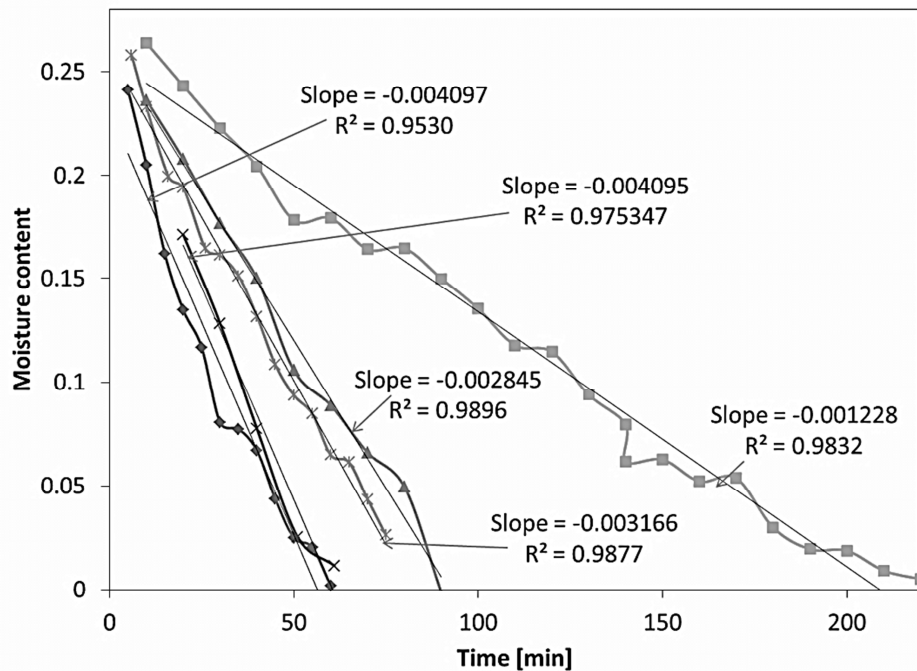


Figure 8.43: Convective drying rate experiments

8.2.2 Slurry drying

The initial moisture content of the slurry was determined by conventional means of completely drying the sample, determining the bone dry mass, and calculating the initial

moisture content through the initial mass. Due to the nature of the slurry, there was a large variation with the initial moisture content. Therefore, a method was devised to determine the drying constant of the dcc slurry at the given temperature. The initial three values were omitted in determining the drying constant. These values have a higher drying rate than the average value, as shown in Figure 66, due to the surface effects of drying.

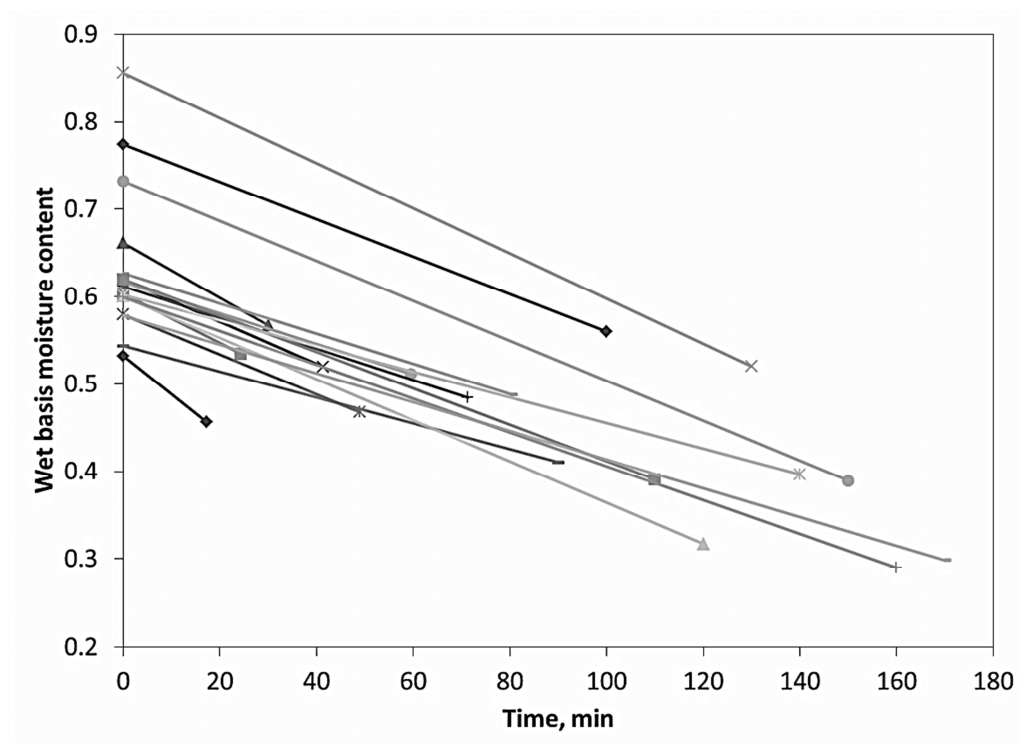


Figure 8.44: Initial data from slurry drying at 100C

The average slope of the remaining cases was determined afterwards. The data points were then fitted to the new line, to determine how well the data fit, through an r-squared value, as shown in Figure 67.

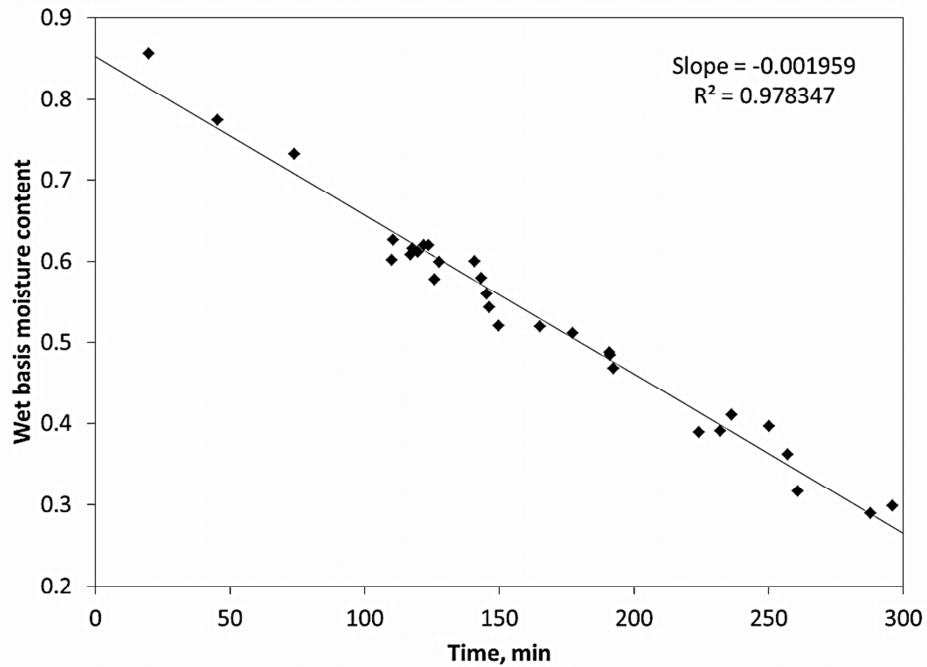


Figure 8.45: Drying rate determined from slurry data at 100C

The measured drying rate falls below the drying rate of the dihydrate (a slope of -0.001959 for the slurry, and a slope of -0.001228 for the dihydrate at 105°C). This was expected, since the water molecules are bonded to the crystal lattice in the dihydrate.

8.2.3 Drying rate calculations

These values were used to calculate the drying rate of the water over the copper II chloride, N_v , to be used to determine the value of B_3 , the constant in Equation 8.41, as shown in Table 22. The Equation is re-arranged to solve for B_3 for four of the experiments conducted. The variability in B_3 is $\pm 20\%$, which is acceptable for this range of values. It appears that there is a slight temperature dependence on B_3 , however further experiments are needed to determine this dependence. The drying rates have the same order of magnitude in other applications, such as those observed by Lin and Chen [79].

Table 8.8: CRDC rate calculations

Variable	Symbol	Unit	Exp. 1	Exp. 2	Exp. 3	Exp. 4
Removal frequency	-	min	5	5	10	10
Temperature	T_b	°C	150	130	130	105
Drying rate	N_v	kg/(m ² ·s)	0.000199	0.000149	0.000141	7.42E-05
Average dry mass	m_s	kg	0.00353	0.00353	0.00353	0.00353
Effective area	A_p	m ²	0.00126	0.00126	0.00126	0.00126
Average moisture content	X	-	0.105	0.105	0.105	0.105
Final moisture content	X_e	-	0.00	0.00	0.00	0.00
Partial pressure of water at T	-	Pa	468 000	272 000	272 000	121 000
Partial pressure of water over CuCl ₂ at T	-	Pa	194 000	86 800	86 800	26 600
Temperature depression due to CuCl ₂	T_{wb}	°C	130	116	116	96.7
beta3	B_3	-	0.000353	0.000381	0.000360	0.000318

Chapter 9

Conclusions and recommendations

9.1 Conclusions

A new correlation for particle size was obtained.

A new correlation based on input parameters was developed for determining particle size. The correlation uses the initial droplet size as calculated by the Mulhem correlation from Table 3. This value is used to calculate various parameters (Reynolds number, Nusselt number, etc.) in Equation 8.18. This correlation can assist in predicting fluidization for the downstream process of the fluidized bed, and increase the energy efficiency of the Cu-Cl cycle

Particle size distributions fit well to existing distribution functions.

The Log-normal distribution performed well for the whole temperature range. The best performing distribution for spherical particles was the Rosin-Rammler distribution. The distribution fitting process will assist in determining narrow distributions, which allow for better fluidization.

New correlations for atomization air flow and the Hausner ratio were determined

Equation 8.2 uses input parameters to determine the atomization air flow rate. This Equation will help in determining an adequate compressor size for the spray dryer.

Equation 8.20 uses various parameters to determine the Hausner ratio. This ratio is directly proportional to the powder's ability to be fluidized, for applications further in the Cu-Cl cycle.

The CRDC rate curve was found to fit adequately to the drying of Copper II Chloride.

This information will be useful in CFD modeling of dcc drying, and future scale up of the Cu-Cl cycle.

9.2 Recommendations

Determine surface moisture effects on the Hausner ratio.

It is believed that the high Hausner ratios were due to high surface moisture. It is recommended to take more of the samples, tap test them, dry it in the oven, tap test again, and study if there is a large difference in Hausner ratios. The Hausner ratio is not directly related to the moisture content, because this powder forms a hydrate. The hydrate feels just as dry as the anhydrous form, but there could be surface moisture stuck on the anhydrous material after drying, which would cause a higher Hausner ratio due to the sticky nature of the surface moisture. Since the crystal structure of the powder changes at different moisture contents, the surface moisture may have a greater role in fluidization than the bound moisture.

Develop a model for color vs. moisture content.

The color of dcc changes significantly at various moisture contents. By developing a model for moisture content vs. color, the final moisture content can be determined in situ, and in real-time. This information can later be used as a feedback mechanism for automating the Cu-Cl cycle. Since the color affects the crystal structure (ie. anhydrous vs. dihydrate), this model will also predict the final crystal structure after drying.

Determine the equilibrium moisture content vs. temperature for ambient temperatures to 100°C.

This data will be valuable in spray drying, and also in long-term storage of dcc, crystallization, and other types of drying pursued for the Cu-Cl cycle.

Bibliography

- [1] C. Cooper, and W. P. Nel, "Implications of Fossil Fuel Constraints on Economic Growth and Global Warming," *Energy Policy*, vol. 37, pp. 166-180, 2009.
- [2] International Energy Agency, "Key world energy statistics," Paris, 2010.
- [3] J. Zalasiewicz et al., "The New World of the Anthropocene," *J. of Envi. Sci. Tech.*, vol. 44, pp. 2228-2231, 2010.
- [4] S. W. Diegel, and S. C. Davis, "Transportation Energy Data Book," Oak Ridge National Laboratory, Tennessee, DE-AC05-00OR22725, 2010.
- [5] G. F. Naterer et al., "Canada's program on nuclear hydrogen production and the thermochemical Cu-Cl cycle," *Int. J. Hydrogen Energy*, vol. 35, pp. 10905-10926, 2010.
- [6] OECD/IEA, "Hydrogen production and storage," *Energy Tech. essentials*, vol. 5, pp. 1-4, April 2007.
- [7] M. Sakurai et al., "Experimental study on side-reaction occurrence condition in the iodine sulfur thermochemical hydrogen production process," *Int. J. Hydrogen Energy*, vol. 23, pp. 613-619, 2000.
- [8] K. Schultz, "Thermochemical production of hydrogen from solar and nuclear energy," Stanford global climate and energy project, General Atomics, San Diego, CA, 2003.

- [9] Z. L. Wang, "Comparison of sulfur–iodine and copper–chlorine thermochemical hydrogen production cycles," *Int. J. Hydrogen Energy*, vol. 35, no. 10, pp. 4820-4830, May 2010.
- [10] G. F. Naterer et al., "Thermochemical hydrogen production with a copper-chlorine cycle I: oxygen release from copper oxychloride decomposition," *Int. J. Hydrogen Prod.*, vol. 33, pp. 5439-5450, 2008.
- [11] I. Dincer, M. A. Rosen, and M. F. Orham, "Design of systems for hydrogen production based on the cu-cl thermochemical water decomposition cycle: configurations and performance," *Int. J. Hydrogen Prod.*, vol. 30, pp. 1-12, 2011.
- [12] M. A. Rosen, "Advances in hydrogen production by thermochemical water decomposition: A review," *Energy*, vol. 35, pp. 1068–1076, 2010.
- [13] S. Suppiah et al., "Recent CuCl/HCl Electrolyzer developments at AECL," in *ORF workshops on nuclear-based thermochemical hydrogen production*, Oshawa, 2011.
- [14] C. H. Gammons, A. E. Williams-Jones, and Z. F. Xiao, "Experimental study of copper(I) chloride complexing in hydrothermal solutions at 40 to 300 C and saturated water vapor pressure," *Geochimica et Cosmochimica Acta*, vol. 62, pp. 2949-2964, 1998.
- [15] G. F. Naterer, K. S. Gabriel, and V. N. Daggupati, "Diffusion of gaseous products through a particle surface layer in a fluidized bed reactor," *Int. J. Heat Mass Transfer*, vol. 53, pp. 2449-2458, 2008.

- [16] G. F. Naterer, I. Dincer, and V. N. Daggupati, "Convective heat transfer and solids conversion of reacting particles in a copper(II) chlorine fluidized bed," *Chem. Eng. Sci.*, vol. 66, pp. 460-468, 2011.
- [17] N. Busscher et al., "Evaporation influences on the crystallization of an aqueous dihydrate cupric chloride solution with additives," *J. Colloid Interface Sci.*, no. 344, pp. 556–562, 2010.
- [18] J. Tanskanen, T. Kuokkanen, and T. Keskitalo, "Analysis of key patents of the regeneration of acidic cupric chloride etchant waste and tin stripping waste," *Resources, Conservation and Recycling*, no. 49, pp. 217–243, 2007.
- [19] O. G. Polyachenok et al., "Formation of a super disperse phase and its influence on equilibrium and thermodynamics of thermal dehydration," *Thermochimica Acta*, vol. 467, pp. 44-53, 2008.
- [20] S. M. A. Basir, "Recovery of cupric chloride from spent copper etchant solutions: a mechanistic study," *Hydrometallurgy*, vol. 69, no. 1-3, pp. 135-143, April 2003.
- [21] I. Dincer, G. F. Naterer, and C. Zamfirescu, "Thermophysical properties of copper compounds in copper–chlorine thermochemical water splitting cycles," *Int. J. Hydrogen Energy*, vol. 35, no. 10, pp. 4839-4852, May 2010.
- [22] A. S. Mujumdar, *Handbook of industrial drying*, 3rd ed. New York, USA: CRC Press, 2006.

- [23] V.N. Daggupati et al., "Effects of atomization conditions and flow rates on spray drying for cupric chloride formation," *Int. J. Hydrogen Energy*, vol. 22, pp. 990-997, 2010.
- [24] K. R. Mahadik, A. Paradkar, and A. A. Ambike, "Spray-dried amorphous solid dispersions of simvastatin, a low Tg drug: in vitro and in vivo evaluations," *J. Pharmaceutical Research*, vol. 22, pp. 990-997, 2005.
- [25] K. Stahl et al., "The effect of process variables on the degradation and physical properties of spray dried insulin intended for inhalation," *Int. J. Pharmaceutics*, vol. 233, pp. 227-237, 2002.
- [26] P. Meenan et al., "The influence of spray drying conditions on the particle properties of recrystallized burkeite ($\text{Na}_2\text{CO}_3 \cdot (\text{Na}_2\text{SO}_4)_2$)," *Powder Tech.*, vol. 90, pp. 125-130, 1997.
- [27] V. S. Birchal et al., "Effect of spray-dryer operating variables on the whole milk powder quality," *Drying Tech.*, vol. 23, pp. 611-636, 2005.
- [28] N. T. Bhaskar, and V. J. Sachin, "Optimization of spray drying of ginger extract," *Drying Tech.*, no. 28, pp. 1426-1434, 2010.
- [29] G. F. Naterer et al., "Thermochemical hydrogen production with a copper-chlorine cycle II: Flashing and drying of aqueous cupric chloride," *Int. J. of Hydrogen Energy*, vol. 33, pp. 5451-5459, 2008.

- [30] P. Bach, A. D. Jensen, and P. D. Hede, "Two-fluid spray atomisation and pneumatic nozzles for fluid bed coating / agglomeration purposes: A review," *Chem. Eng. Sci.*, vol. 63, pp. 3821-3842, 2008.
- [31] P. Thybo et al., "Scaling up the spray drying process from pilot to production scale using an atomized droplet size criterion," *Pharmaceutical Research*, vol. 25, no. 7, pp. 1610-1620, 2008.
- [32] S. Gunther, U. Fritschinm, and B. Mulhem, "Solid-liquid separation in suspension atomization," *Chem. Eng. Sci.*, no. 61, pp. 2582-2589, 2006.
- [33] P.E. Sojka, and E. Babinsky, "Modeling drop size distributions," *Prog. in E. Comb. Sci.*, no. 28, pp. 303-329, 2002.
- [34] L. Hovgaard, and P. Thybo, "Droplet Size Measurements for Spray Dryer Scale-Up," *Pharmaceutical Develop. Tech.*, vol. 13, pp. 93-104, 2008.
- [35] X. Xu et al., "Measurement and influence factors of the fowability of microcapsules with high- content B-Carotene," *Chinese J. Chem. Eng.*, vol. 4, no. 15, pp. 579-585, 2007.
- [36] D. Geldart, and E. C. Abdullah, "The use of bulk density measurements as flowability indicators," *Powder Tech.*, no. 102, pp. 151-165, 1999.
- [37] C. J. Mumford, and D. E. Dalton, "Spray dried products - characterization of particle morphology," *Trans. Insitution Chem. Engineers*, vol. 77, pp. 21-38, 1999.

- [38] T.K. Kockel and T.A.G. Langrish, "The assessment of a characteristic drying curve for milk powder for use in computational fluid dynamics modelling," *Chem. Eng. J.*, no. 84, pp. 69-74, 2001.
- [39] M. A. Mohamed, and S. A. Halawy, "Non-Isothermal Kinetic and Thermodynamic Study for the Dehydration of Copper(II) Chloride Dihydrate and Nickel Chloride Hexahydrate," *J. Thermal Anal.*, vol. 41, pp. 147-159, 1994.
- [40] E. N. Dudkina, L. D. Polyachenok, and O. G. Polyachenok, "Thermal stability and thermodynamics of copper(II) chloride dihydrate," *J. Chem. Thermodynamics*, vol. 41, pp. 74-79, 2009.
- [41] W. S. Rayleigh, "On the instability of jets," *Proc. London Math Soc.*, no. 10, pp. 4-13, 1879.
- [42] F. Ommi, S. M. Hosseinalipour, and E. Movahednejad, "Prediction of droplet size and velocity distribution in droplet formation region of liquid spray," *Entropy*, no. 12, pp. 1484-1498, 2010.
- [43] Rasmussen K., "Calculation methods for the physical properties of air used in the calibration of microphones," Tech. Un. of Denmark, Proposal PL-11b, 1997.
- [44] E. Gilliland et al., "Diffusion on surfaces. 1. Effect of concentration on the diffusivity of absorbed gases," *Industrial Eng. Chemistry Fundamentals*, vol. 2, no. 13, pp. 95-100, 1974.

- [45] J. M. Prausnitz, B. E. Poling, and R. C. Reid, *The properties of gases and liquids*, 4th ed. New York: McGraw-Hill, 1987.
- [46] D. P. Dewitt, and F. P. Incropera, *Fundamentals of heat and mass transfer*, 5th ed. New York: Willey, 2002.
- [47] W. E. Cooper, and M. Laliberte, "Model for calculating the density of aqueous electrolyte solutions," *J. Chem. Eng. Data*, no. 49, pp. 1141-1151, 2004.
- [48] J. O. Maloney, *Perry's Chemical Engineer's Handbook*, 8th ed. United States: McGraw-Hill, 2008.
- [49] M. Laliberte, "Model for calculating the viscosity of aqueous solutions," *J. Chem. Eng. Data*, no. 52, pp. 321-335, 2007.
- [50] M. Laliberte, "A model for calculating the heat capacity of aqueous solutions, with updated density and viscosity data," *J. Chem. Eng. Data*, no. 54, pp. 1725-1760, 2009.
- [51] C. S. Dutcher et al., "Surface tension of inorganic multicomponent aqueous electrolyte solutions and melts," *J. Phys. Chem.*, no. 114, pp. 12216-12230, 2010.
- [52] G. H. Hua, Y. G. Li, and Y. X. Yu, "Surface tension for aqueous electrolyte solutions by the modified mean spherical approximation," *Fluid Phase Equilibria*, no. 173, pp. 23-38, 2000.
- [53] R. N. Goldberg, "Evaluated activity and osmotic coefficients for aqueous solutions: Bi-univalent compounds of lead, copper, manganese, and uranium," *J. Phys. Chem.*

Ref. Data, vol. 8, no. 4, pp. 1005-1050, 1979.

- [54] F. P. Incropera et al., *Fundamentals of Heat and Mass Transfer*. USA: John Wiley & Sons, 2011.
- [55] L. Riedel, "Die wärmeleitfähigkeit von wässrigen lösungen starker elektrolyte," *Chem. Ing. Tech.*, vol. 3, no. 23, pp. 59-64, 1951 (in German).
- [56] A. Anderko, and P. Wang, "Modeling thermal conductivity of concentrated and mixed-solvent electrolyte systems," *Ind. Eng. Chem. Res.*, no. 47, pp. 5698-5709, 2008.
- [57] D. N. Noel, *Physical and chemical equilibrium for chemical engineers*. New York: Wiley, 2002.
- [58] L. Meaux, "MaxRace Software & Meaux Racing Heads/Engines," Larry Meaux/MaxRace Software, Abbeville, LA, Software guide 1995.
- [59] G. Marin, "Evaporative drying of cupric-chloride droplets in a thermo-chemical cycle of hydrogen production," Univ. of Ontario Inst. of Tech., Oshawa, MASC Thesis 2008.
- [60] X. D. Chen, S. Kar, and K. C. Patel, "The temperature uniformity during air drying of a colloidal liquid droplet," *Drying Tech.*, no. 23, pp. 2337–2367, 2005.
- [61] H. C. Van Ness, M. M. Abbott, and J. M. Smith, *Introduction to chemical engineering thermodynamics*, 6th ed. New York: McGraw Hill, 2001.

- [62] C. Weber, "Zum zerfall eines flussigkeitsstrahles," *Zeitschrift fur Angewandte Mathematik Und Mechanik*, no. 2, pp. 136-154, 1931 (in German).
- [63] N. Ashgriz, Ed., *Handbook of Atomization and Sprays*. New York: Springer Sci., 2011.
- [64] A. Levy, I. Borde, and M. Mezhericher, "Theoretical drying model of single droplets containing insoluble or dissolved solids," *Drying Tech.*, no. 25, pp. 1035-1042, 2007.
- [65] D. X. Chen, and K. C. Patel, "Prediction of Spray Dried Product Quality using two Simple Kinetic Drying Models," *J. Food Process Eng.*, no. 28, pp. 567-594, 2005.
- [66] X. D. Chen, and K. C. Patel, "Surface-center temperature differences within milk droplets during convective drying and drying-based Biot number analysis," *Bioengineering, Food, and Natural Products*, vol. 54, no. 12, pp. 3273-3290, December 2008.
- [67] J. C. Yang, "Hetrogeneous combustion," in *Environmental implications of combustion processes*. Gaithersburg, MA: CRC Press, 1993, ch. 4, pp. 91-137.
- [68] P. Bahadorani, "Evaporative heat and mass transfer with solubility driven solidification of aqueous droplet flows," University of Ontario Insittute of Technology, Oshawa, MAsc Thesis 2009.
- [69] J. R. Marshall, and W. E. Ranz, "Evaporation from drops," *Chem. Eng. Progress*, vol. 48, pp. 141-146, 1952.

- [70] L. L. Ross, and T.W. Hoffman, "A Theoretical investigation of the effect of mass transfer on heat transfer to an evaporating droplet," *Int. J. Heat Mass Transfer*, vol. 15, pp. 559-617, 1971.
- [71] J. R. Grace, M. E. Weber, and R. Clift, *Bubbles, drops, and particles*. New York: Academic Press, 1978.
- [72] S. S. Sazhin, "Advanced models of fuel droplet heating and evaporation," *Progress in Energy and Combustion Sci.*, no. 32, pp. 162-214, 2006.
- [73] R.W. Tate and W.R. Marshall, "Atomization by centrifugal spray nozzles," *Chem. Eng. Prog.*, no. 49, pp. 169-174, 1953.
- [74] and Rammler E. Rosin P., "The laws governing the fitness of powdered coal," *J. Inst. Fuel*, no. 7, pp. 29-36, 1933.
- [75] Mujumdar A.S., *Handbook of Industrial Drying*, 3rd ed. New York, USA: CRC Press, 2006.
- [76] Spray Systems Co., 1/4JAU & 1/4JAUCO Automatic Air Atomizing Nozzles, 2008.
- [77] A. Engberg, "An X-ray refinement of the crystal structure of copper (II) chloride dihydrate," *Acta Chemica Scandinavica*, no. 24, pp. 3510-3526, 1970.
- [78] Mokry S., "Development of a Heat-Transfer Correlation for Supercritical Water in Supercritical Water-cooled Reactor Applications," UOIT, Oshawa, Canada, MASC. Thesis 2009.

- [79] X. Q. Lin, and X. D. Chen, "Air drying of milk droplet under constant and time-dependent conditions," *J. Bioengineering, Food, and Natural Products*, vol. 51, pp. 1790-1799, 2005.
- [80] A. C. F. Ribeiro et al., "Diffusion Coefficients of Copper Chloride in Aqueous Solutions at 298.15 K and 310.15 K," *J. Chem. Eng. Data*, no. 50, pp. 1986-1990, 2005.
- [81] Partnership for advancing the transition to hydrogen, "Annual report on world progress in hydrogen," Washington D. C., USA, 2011.
- [82] U.S. Energy Information Administration, "Electric Power Annual 2009," Washington D. C., DOE/IEA-0348(2009), 2011.
- [83] D. Venkatanarasaiah, Y. B. G. Varma, and K. Sreenivasaulu, "Drop size distributions in liquid pulsed columns," *Bioprocess Eng.*, no. 17, pp. 189-195, 1997.
- [84] L. Riedel, "Die wärmeleitfähigkeit von wäßrigen Lösungen starker elektrolyte," *Chemie-Ingenieur-Technik*, no. 23, p. 59, 1951 (in German).
- [85] J. Pisecky, *Handbook of milk powder manufacture*. Copenhagen, Denmark: Niro A/S, 1997.
- [86] K. C. Patel, and X. D. Chen, "Prediction of spray-dried product quality using two simple drying kinetics models," *J. Food Proc. Eng.*, no. 28, pp. 567-594, 2005.

Appendix A: Surface tension, viscosity, and density measurements

CuCl₂		DM water			2g/100ml		
T	C	24	40	50	24	40	50
μ	m²/s	9.11E-07	7.96E-07	7.58E-07	9.18E-07	9.11E-07	8.51E-07
σ	N/m	0.0629	0.0608	0.0594	0.0616	0.0606	0.0589
ρ	kg/m³	996.1	992.6	987.0	1015.0	1005.5	1001.6
		4g/100ml			8g/100ml		
T	C	24	40	50	24	40	50
μ	m²/s	9.55E-07	9.16E-07	9.13E-07	1.02E-06	9.91E-07	9.68E-07
σ	N/m	0.0614	0.0601	0.0602	0.0600	0.0629	0.0638
ρ	kg/m³	1033.3	1024.6	1018.8	1055.7	1054.7	1054.7

Appendix B: program for Bayesian information criterion test

This program was originally written for the Chi-squared test. However, after determining that the chi-squared test gave skewed lower-values, the code was adapted to the Bayesian criterion.

```
Sub logNormal()
%Variable initialization
  Dim i As Integer
  Dim j As Integer
  Dim k As Integer
  Dim TestRow As Integer
  Dim TestCol As Integer
  Dim ChiValue As Double
  Dim ChiTest As Double
  Dim Sigma As Double
  Dim Dbar As Double
  Dim SigmaLow As Double
  Dim DbarLow As Double
  ChiValue = 0
  ChiTest = 1
  Sigma = 1
  Dbar = 1
  TestRow = 18
  TestCol = 20
  For i = 1 To 80
    Sigma = 1.5 + i * 0.01
    Cells(3, TestRow).Value = Sigma
    For j = 1 To 80
      Dbar = 4.5 + j * 0.1
      Cells(4, TestRow).Value = Dbar
      %Summation for test
      For k = 1 To TestCol
        ChiValue = ChiValue + (Abs(Cells(7 + k, 4).Value -
Cells(7 + k, TestRow).Value)) ^ 2
      Next k
      ChiValue = ChiValue / (TestCol - 1)
      %test-check
      If ChiTest > ChiValue Then
        SigmaLow = Sigma
        DbarLow = Dbar
        ChiTest = ChiValue
      End If
      ChiValue = 0
    Next j
  Next i
  Cells(3, TestRow).Value = SigmaLow
  Cells(4, TestRow).Value = DbarLow
End Sub
```

Appendix C: Experimental results

Table 12.1: Experimental results: spray drying

	X	Hs. R.	Vfc	SMD	vrms	Trms	mwma	Oh	Re	We	Nu	Bt
	% Dry B.	-	-	um	m/s	C	-	-	-	-	-	-
1	27.39	1.489	0.500	84.26	1.27	30.34	0.0431	14.19	1.80	0.0264	3.37	0.015
2	26.95	-	0.500	12.04	1.23	41.11	0.0446	12.14	2.15	0.0250	3.36	0.015
3	25.33	1.604	0.126	4.102	1.32	65.82	0.0417	9.48	3.39	0.0302	3.45	0.019
4	4.97	1.818	0.126	5.267	1.32	97.49	0.0417	8.26	4.92	0.0332	3.49	0.025
9	1.32	1.892	0.091	3.252	1.76	111.90	0.0277	6.53	5.60	0.0374	3.43	0.029
20	35.40	1.657	0.500	133.3	2.44	27.00	0.0308	7.48	4.79	0.1541	4.47	0.014
19	26.58	1.801	0.068	4.968	2.47	59.02	0.0306	4.60	8.57	0.1527	4.55	0.018
18	1.44	2.012	0.067	4.476	2.49	113.63	0.0303	3.01	16.04	0.1478	4.64	0.030
30	2.00	1.857	0.105	7.135	2.22	118.70	0.0349	2.97	16.03	0.1265	4.58	0.032
31	26.80	1.718	0.500	9.539	2.18	60.82	0.0356	4.43	8.32	0.1250	4.48	0.019
32	27.24	1.759	0.500	79.29	2.22	27.86	0.0349	7.15	4.75	0.1325	4.44	0.014
33	27.28	1.739	0.500	20.62	1.72	34.66	0.0284	13.58	1.98	0.0369	3.32	0.015
11	20.41	1.62	0.074	5.553	1.76	58.02	0.0277	9.79	3.02	0.0380	3.38	0.012
5	3.98	1.818	0.091	5.612	1.39	112.61	0.0349	6.51	4.43	0.0230	3.23	0.028
16	26.84	1.608	0.500	88.45	1.96	26.77	0.0241	16.09	1.79	0.0464	3.36	0.014
12	21.71	1.547	0.075	4.979	1.94	57.90	0.0244	9.99	3.10	0.0442	3.40	0.018
6	1.53	1.822	0.092	3.539	1.63	119.61	0.0299	6.34	5.52	0.0316	3.37	0.032
34	27.10	1.702	0.500	92.11	1.70	28.21	0.0287	15.23	1.71	0.0361	3.30	0.015
35	26.58	1.732	0.092	6.732	1.65	61.06	0.0295	9.46	2.96	0.0336	3.32	0.018
13	26.00	1.834	0.064	4.949	1.28	69.80	0.0709	8.78	2.41	0.0190	3.07	0.020
7	1.47	1.746	0.067	6.369	1.10	135.55	0.0820	5.96	3.93	0.0131	3.01	0.037
38	27.14	1.906	0.500	93.14	1.23	29.77	0.0756	14.80	1.28	0.0190	3.04	0.015
37	25.62	1.644	0.500	6.453	1.19	67.59	0.0782	8.84	2.33	0.0174	3.06	0.020
36	1.37	1.71	0.094	5.288	1.21	136.31	0.0769	6.07	4.68	0.0175	3.14	0.038
17	27.35	1.775	0.500	73.67	1.75	27.91	0.0357	15.74	1.63	0.0368	3.26	0.015
14	25.61	1.771	0.069	5.979	1.57	61.14	0.0396	9.62	2.63	0.0289	3.22	0.019
8	3.04	1.847	0.092	9.239	1.56	124.33	0.0412	6.24	5.50	0.0285	3.33	0.031
41	26.95	1.22	0.500	90.28	1.57	28.34	0.0409	15.19	1.59	0.0309	3.23	0.014
40	21.11	1.706	0.100	8.512	1.48	62.83	0.0432	9.29	2.72	0.0271	3.23	0.019
39	0.93	2.09	0.096	6.185	1.53	123.61	0.0420	6.26	5.36	0.0278	3.32	0.033
15	27.20	1.754	0.500	62.37	1.70	58.11	0.0425	9.78	2.91	0.0354	3.34	0.018
10	23.88	1.692	0.092	12.49	1.74	113.70	0.0415	6.48	5.61	0.0353	3.42	0.025
42	21.70	1.693	0.082	8.273	1.67	112.72	0.0431	6.50	5.35	0.0336	3.39	0.030
28	22.00	1.777	0.105	5.196	1.43	63.16	0.0357	9.25	2.64	0.0251	3.20	0.019
29	1.70	1.885	0.089	8.613	1.70	117.48	0.0302	6.39	5.65	0.0344	3.40	0.031
21	1.06	1.965	0.143	8.285	1.84	121.18	0.0318	11.86	9.77	0.1183	4.09	0.033
22	27.24	2.162	0.500	61.69	1.84	56.34	0.0318	11.02	4.71	0.0708	4.01	0.018
23	24.34	1.636	0.144	13.52	1.71	64.22	0.0342	10.49	4.90	0.0631	3.94	0.020
24	27.22	1.617	0.500	94.19	1.75	32.44	0.0333	14.17	2.96	0.0592	3.92	0.015
25	1.67	2.096	0.128	7.838	1.76	115.82	0.0297	6.97	6.78	0.0474	3.60	0.031
26	23.48	-	0.115	14.23	1.76	59.96	0.0297	9.54	3.63	0.0445	3.55	0.019
27	28.98	34.7	0.500	94.01	1.76	29.92	0.0297	14.27	2.15	0.0439	3.50	0.015

Appendix D: Results from particle distribution analysis

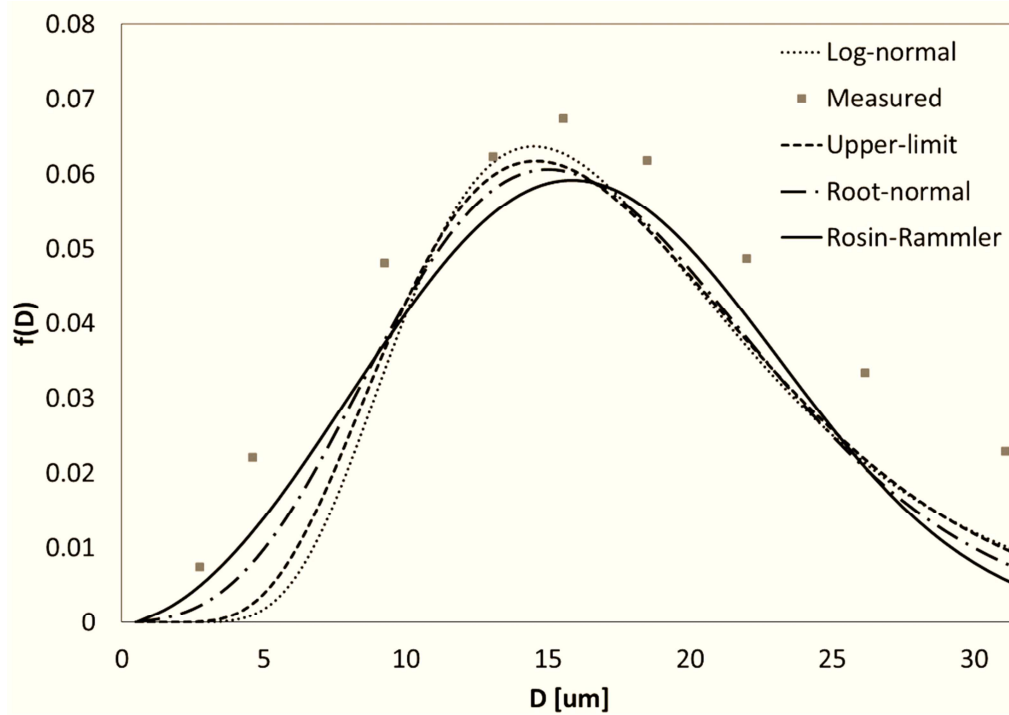


Figure 13.1: Run no. 1 (60C, 0.7mm nozzle) particle results

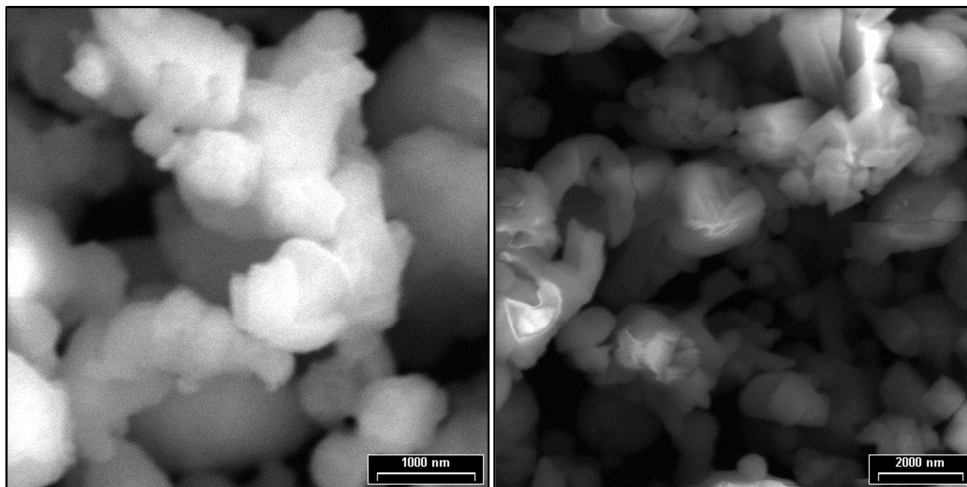


Figure 13.2: Run no. 1 (60C, 0.7mm nozzle) SEM results

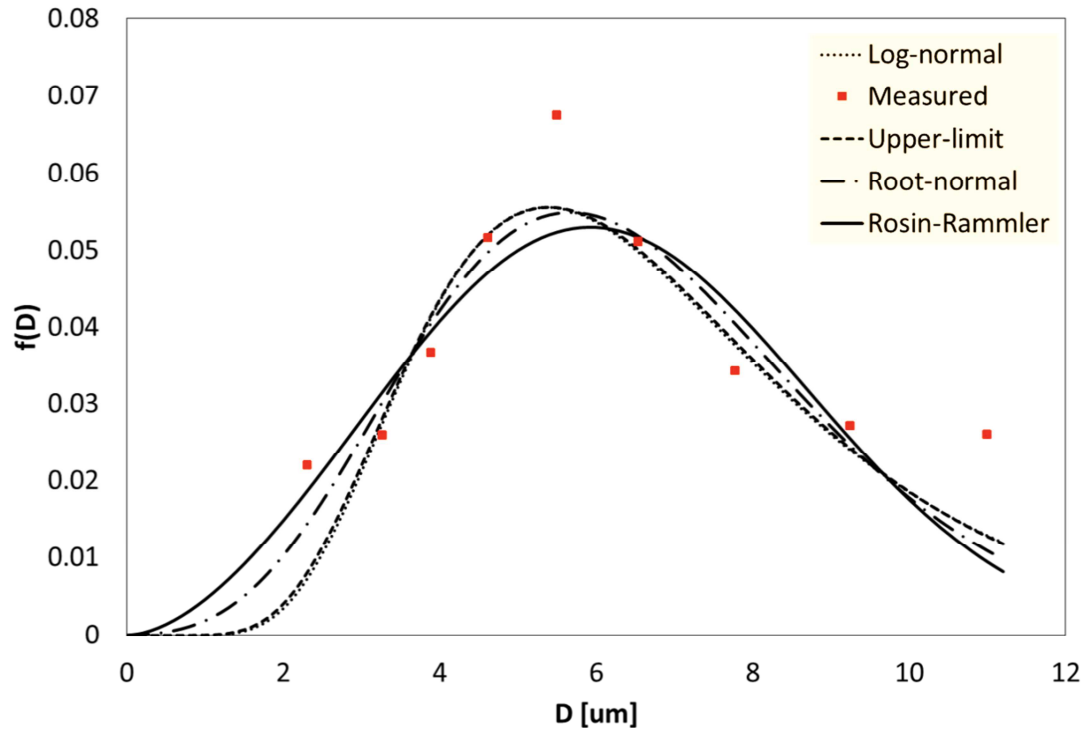


Figure 13.3: Run no. 4 (160C, 0.7mm nozzle) particle results

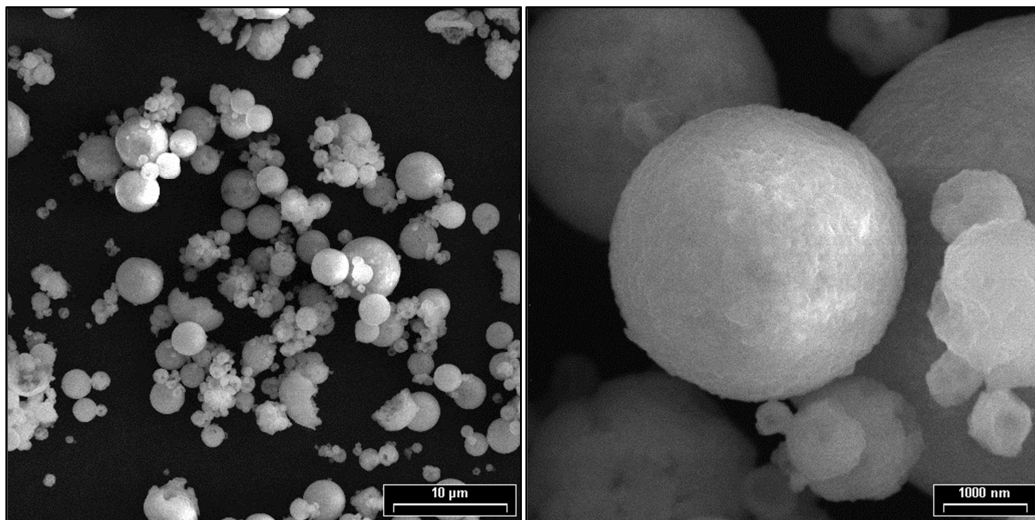


Figure 13.4: Run no. 4 (160C, 0.7mm nozzle) SEM results

Appendix E: Matlab code

Property models

```
function air_density = air_den(T_bulk_gas, gas_h)
air_density = (353.12832/T_bulk_gas)*( (1+gas_h)/(1+1.6*gas_h));
end
```

Property models

```
function air_density = air_den(T_bulk_gas, gas_h)
air_density = (353.12832/T_bulk_gas)*( (1+gas_h)/(1+1.6*gas_h));
end
```

```
function air_diffusion = air_dif(T_gas)
air_diffusion = 1.963*10^7*T_gas - 3.33307*10^5;
end
```

```
function air_viscosity = air_visc(T_air)
a = (((((-2.8054253*10^(-10)*T_water + 1.0556302*10^(-7))*T_water -
4.6170461*10^(-5))*T_water - 0.0079870401)*T_water + 16.945176)*T_water +
999.83952);
b = 1 + 0.01687985*T_water;
air_viscosity = a/b;
end
```

```
function wat_surface_tension = wat_surf_ten(T_water_c)
T_water = T_water_c+273.15;
wat_surface_tension = 235.8*((647.15-T_water)/647.15)^1.256)*(1-
0.625*((647.15-T_water)/647.15))/1000;
end
```

```
function surface_tension = surf_ten(T_water, c_cucl2)
beta = -0.06;
watden = water_den(T_water);
g_g_cucl2 = 10*c_cucl2/(watden/1000);
mmass_cucl2 = 63.5463 + 35.4532*2;
b_molal = g_g_cucl2/mmass_cucl2;
s_molal = b_molal*(1-beta/(1+(3*b_molal/55.51)));
b_osmotic = 0.52*log(b_molal+2.18)+1/(170*(b_molal+0.032))+0.362-
0.0139*b_molal-0.0058*b_molal^2+0.00009*b_molal^3+0.0000516*b_molal^4;
s_osmotic = 0.52*log(s_molal+2.18)+1/(170*(s_molal+0.032))+0.362-
0.0139*s_molal-0.0058*s_molal^2+0.00009*s_molal^3+0.0000516*s_molal^4;
wat_ten = wat_surf_ten(T_water);
surface_tension=wat_ten+(3*8.314462*(T_water+273.15)^0.95/(55.51*722.5))*
(b_molal*b_osmotic-s_molal*s_osmotic);
end
```

```

function water_density = water_den(T_water)
a = (((((-2.8054253*10^(-10)*T_water + 1.0556302*10^(-7))*T_water -
4.6170461*10^(-5))*T_water - 0.0079870401)*T_water + 16.945176)*T_water +
999.83952);
b = 1 + 0.01687985*T_water;
water_density = a/b;
end
function elect_density = elect_den(T_water, c_cucl2)
watden = water_den(T_water);
w_cucl2 = 1/(1 + 1/(10*c_cucl2/watden));
w_water = 1 - w_cucl2;
a = w_cucl2 + 0.07185 + 0.002565*T_water;
b = (1868.5*w_cucl2 + 1137.20)*exp(0.000001*((T_water+575.7)^2));
elect_density = 1/((w_water/watden)+w_cucl2*a/b);
end

function air_thermal_conductivity = k_air(T_air)
air_thermal_conductivity = 1.5207e-11*T_water^3 - 4.8574e-8*T_water^2 +
1.0184e-4*T_water - 0.00039333;
end

function water_thermal_conductivity = k_wat(T_water)
water_thermal_conductivity = 0.57109 + 0.0017625*T_water - 6.7036e-
6*T_water^2
end

```

Appendix E: Corrosion notes

A chrome coating was originally applied to the stainless steel parts on the spray dryer. However, the chrome did not withstand the corrosive properties of dcc. Viton and Teflon were found to be resist corrosion up to 200°C; Viton was chosen as a coating since it was readily obtainable. Corrosion was a problem at the atomizing nozzle, as shown in Figure 17: stainless steel is not favorable to withstand high concentrations of chlorine ions.

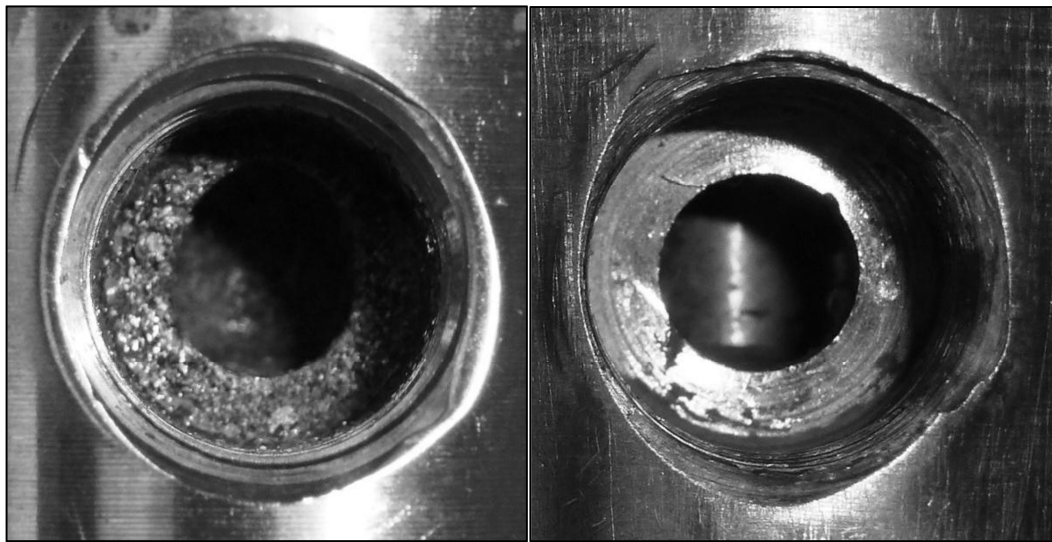


Figure 15.1: *Stainless Steel (left) and Titanium (right) nozzle corrosion*

	%	Plastics		Elastomers		Metals			
		CPVC	Teflon	Viton	Si	316 SS	Ti	Hastelloy C	Ta
CuCl	Sat	100	120	100	-	X	100	100	-
CuCl ₂	sat	80	120	100	25	-	118	100	-
HCl	25	80	120	120	25	X	25	60	200
HCl	35	80	120	120	25	X	X	60	150
HCl	38	80	120	120	X	X	X	40	150
HCl	50	80	120	120	X	X	X	30	-

Table 15.1: Compiled chemical resistance data

Copper II chloride is a very corrosive liquid, as is hydrochloric acid. The output from the electrolytic cell, an 8-10 molar solution of hydrochloric acid and dcc, puts limitations on the substances available for various components for further processing of the electrolyte. Table 24 shows the chemical resistance of various substances to dcc and hydrochloric acid; the corrosion resistance performance of various alloys to hydrochloric acid is shown in the accompanying Figure. For most metal parts, a plastic Teflon coating will suffice to resist the electrolytic solution. However, if spray drying is chosen as part of the process, difficulty arises in finding a satisfactory alloy to resist corrosion. For the purposes of this study, only dcc was used without mixing hydrochloric acid.

Small quantities of multi-valent metals in solution (Fe, Cu, Ni, Mo, or Ti) can suppress the corrosive properties of hydrochloric acid on titanium. This suggests that the hydrochloric acid alone is more corrosive against titanium as compared with hydrochloric acid in solution with dcc. Titanium forms a passive surface very quickly.